Localization, dualization, and magnetic fields in strongly coupled quantum field theories

Dissertation zur Erlangung
des Doktorgrades der Naturwissenschaften
(Dr. rer. nat.)
der Fakultät Physik

vorgelegt von

Jacob Wellnhofer
aus Großmehring

im Jahr
2018

Promotionsgesuch eingereicht am: 17.01.2018
Die Arbeit wurde angeleitet von: PD Dr. Falk Bruckmann

Termin des Promotionskolloquiums: 25.04.2018

Prüfungsauschuss:

Vorsitzender:	Prof. Dr. Dieter Weiss
1. Gutachter:	PD Dr. Falk Bruckmann
2. Gutachter:	Prof. Dr. Tilo Wettig
weiterer Prüfer:	Prof. Dr. John Schliemann

Abstract

This thesis is comprised of three parts. In part one Anderson localization is studied in the context of QCD, an Anderson-Ising model, and $CP(N-1)$. For the first two the effect of a background magnetic field on the localization properties is studied. In $CP(N-1)$ localization of fermion eigenmodes in the background of the (auxiliary) $U(1)$ gauge field is investigated. In all three cases a transition from localized modes near the origin and delocalized modes in the bulk of the spectrum can be observed. The second part is concerned with Landau levels in QCD. The Landau levels are identified and their contributions to several observables are calculated using lattice methods. The third part deals with the sign problem in QCD at nonzero density. It is shown that the sign problem is exclusively fermionic in nature by considering *scalar* QCD, i.e., QCD with scalar quarks. In this scalar theory the sign problem is found to be absent for up to three flavors, when using a formulation with dual variables.

Contents

1 Introduction

Since the advent of modern physics with the discovery of first *special relativity* and then *general relativity* on the one hand, and Quantum theory on the other, tremendous progress has been made in many areas of physics. The former has lead to the new field of *cosmology*, studying the evolution of the universe as a whole. The latter has branched into many different fields, ranging from *condensed matter physics* to *high energy particle physics*.

The most successful theoretical development for particle physics was the so called *Standard model*. It is comprised of three distinct parts: Quantum electro dynamics (QED), weak interactions, and quantum chromo dynamics (QCD). The first two have been combined into the so called *electro weak* theory, which is a unification at high energy scales[1–3]. It encompasses electromagnetic effects as well as radioactive decays. QCD on the other hand deals with strong interactions of sub nuclear particles, i.e., *quarks* and *gluons*. A unification of QCD with the electro weak theory has not been accomplished so far; this is still a topic of current research.

The *color interaction* of QCD is responsible for the *hadronic* bound states of matter; primarily *protons* and *neutrons*. In fact, the constituent particles of QCD, quarks and gluons, have never been observed in isolation, which is known as *confinement*. The other remarkable feature of QCD is *asymptotic freedom*. Namely, due to the *running of the coupling*, the coupling constant decreases with the energy scale. Thus at exceedingly high energies or temperatures quarks and gluons are expected to be no longer bound to each other. The transition from the confined phase to the deconfined phase takes place around[4] $T = 160\,\mathrm{MeV}$; this transition is found to be a crossover rather than a proper phase transition.

Direct experimental measurement of this transition is virtually impossible. (It has been possible to observe signatures of a quark gluon plasma at RHIC[5].) Thus one has to rely on theoretical predictions instead. Such predictions have been facilitated by the use of computers over the last 40 years. Also many computational techniques for simulating QCD with a computer have been developed over the years. Nevertheless, there are some caveats for the simulations. Among the more severe ones are on the one hand *real time* simulations, and on the other simulations at nonzero density, that is, simulations where the matter content does

not match that of antimatter. In both cases one faces a sign problem, making the simulations prohibitively expensive. Real time simulations are of interest because they could capture the dynamical behavior of QCD interactions, as they occur, for instance, in collider experiments. Nevertheless, the feasibility of real time simulations is still an open question.

In recent years there has been some progress in simulating theories with a sign problem at nonzero density by using dual variables; for example, the Schwinger model on the lattice[6], and $O(N)$ and $CP(N-1)$ models[7], to name but two. Using the same principles also a dual formulation of *scalar* QCD has been found[8], which is part of this thesis. This may have some applications in Gauge-Higgs models.

Simulations at nonzero density in QCD could yield important input for other fields of physics, mainly astrophysics and cosmology, but also nuclear physics. In astrophysics this concerns the internal structure of neutron stars and other very dense objects. In cosmology the development of the very early universe depends on the phase diagram of QCD. Namely, during its evolution the universe went from a very hot and dense state to a rather cool and dilute phase. The details of this transition depend on the route through the phase diagram that was taken.

Another current topic of interest is QCD under the influence of strong magnetic fields. Such magnetic fields can either be generated in heavy ion collisions or by energetic processes in the early universe. In recent years there have been a number of studies[9–11] of strong magnetic fields using first principles lattice simulations. Nevertheless, the subject of Landau levels had never been analyzed in this approach, even though for model calculations[12–14] Landau levels are widely used. This gap has now, at least in part, been filled in this thesis.

Also on the topic of magnetic fields in QCD, the effect on Anderson localization can be studied. The fact that an Anderson transition takes place in the quark spectra of high temperature QCD has been established in Refs. [15–18]. The effect of a background magnetic field in this context is studied in this thesis. Furthermore, it is an interesting question whether also other QCD-like theories, which share a number of properties with QCD, show an Anderson transition. Thus in this thesis the special case of nonlinear sigma models, in particular $CP(N-1)$, are analyzed for their localization properties. This also may give insights into nonperturbative physics of strongly coupled quantum systems.

The following sections and chapters are organized as follows: First a brief introduction to quantum field theory in the continuum and on the lattice is given in **Sec. 1.1**. Furthermore, some simulation strategies as well as the connection of Euclidean field theory to thermodynamics are briefly reviewed.

Next, **Chapter 2** deals with localization; first in QCD (**Sec. 2.2**), then in an Anderson-Ising model (**Sec. 2.3**) and nonlinear sigma models (**Sec. 2.4**). In QCD the effect of a background magnetic field on the localization properties are considered. The same is done for the Anderson-Ising model. In both cases the effect of the magnetic field on the spectrum appears to be similar. Namely, the effect of the magnetic field is to push the spectrum to lower eigenvalues. For nonlinear sigma models, $CP(N-1)$ in particular, localization depends on the dimensionality of the model. For $CP(N-1)$ two dimensions, which has the closest analogy to QCD, all modes appear to be localized. Nevertheless, in three dimensions an Anderson transition takes place in the spectrum, much like in QCD.

In **Chapter 3** Landau levels in QCD are considered. First the problem is studied in two dimensions. In the absence of QCD interactions this has a close connection to Hofstadter's butterfly[19]. Taking also QCD interactions into account the lowest Landau level is clearly separated from the rest. In four spacetime dimensions such a separation cannot be observed. Nevertheless, it is still possible to extract the contribution of the lowest Landau level alone. In this way the lowest Landau level contribution of several observables are studied.

Finally, **Chapter 4** addresses the sign problem in QCD with both fermionic and scalar quarks, using dual variables. First the situation in (strong coupling) QCD is reviewed. There even after going to a dual formulation, a sign problem is still present. Nevertheless, this sign problem appears to be purely fermionic in nature. Therefore a *scalar* version of QCD is considered, to test whether the sign problem is, indeed, absent in this case.

Chapter 5 gives a summary of the results, reviewing the main findings of the preceding chapters.

1.1 Elements of quantum field theory

The following sections only give a very brief introduction to quantum field theory and methods encountered therein. For more elaborate

discussions of these topics, the reader is referred to standard textbooks on the subject, e.g., [20–23].

Quantum field theories can quite generally be defined via their path integral. Given an action $S[\Phi]$ depending on various fields, denoted here simply as Φ, the partition function can be calculated:

$$\mathcal{Z} = \int \mathcal{D}\Phi \, e^{iS[\Phi]}. \tag{1.1}$$

The $\mathcal{D}$ is understood to mean that an integration over the fields Φ is performed at every spacetime point. In this respect, the path integral is not a well defined object, but rather a convenient way of writing. Hence there are only very few cases where the partition function can be computed analytically. All this makes it necessary to introduce some form of regularization, in order to render the results finite. The lattice regularization will be discussed in the next section.

The expectation value of an operator $X[\Phi]$ can be evaluated,

$$\langle X \rangle = \frac{1}{\mathcal{Z}} \int \mathcal{D}\Phi \, X[\Phi] e^{iS[\Phi]}, \tag{1.2}$$

using the partition function to normalize the result.

As an example we will be considering the special case of quantum chromo dynamics (QCD) in the following because this will be the most complicated theory encountered in this thesis. In QCD there are two kinds of fields; namely, the bosonic gauge field A_ν and the fermionic quark fields ψ. The fermionic field is Grassmann-valued and the gauge field lives in the Lie-algebra $su(3)$. The gauge fields convey the color interaction between the different color components of the quarks.

The QCD action can be written as a sum of the fermionic action and the gauge action:

$$S[A, \psi] = S_g[A] + S_f[\psi, A], \tag{1.3}$$

$$S_g[A] = -\frac{1}{4g^2} \int d^4x \, F^a_{\nu\rho}(x) F^{a\nu\rho}(x), \tag{1.4}$$

$$S_f[\psi, A] = \sum_{f=1}^{N_f} \int d^4x \, \bar{\psi}^f(x) (\not{D}(x) - m) \psi^f(x). \tag{1.5}$$

Here $\not{D} = \gamma_\nu (\partial - iA(x))^\nu$ denotes the covariant derivative. The γ-matrices satisfy $\{\gamma_\nu, \gamma_\rho\} = 2g_{\nu\rho}$, with the Minkowski metric $g_{\nu\rho}$. The

field strength tensor can be defined via the covariant derivative, $F_{\nu\rho} = [D_\nu, D_\rho]$. Since A lives in the $su(3)$-algebra, so does F. Therefore F^a denotes the color component a of F.

The QCD action is gauge invariant under the gauge group $SU(3)$ by construction. Namely, given a gauge transformation $\Omega(x) \in SU(3)$, the quark fields are transformed as $\psi(x) \to \Omega(x)\psi(x)$, while the covariant derivative transforms as $D_\nu(x) \to \Omega(x)D_\nu(x)\Omega^\dagger(x)$. In this way, the fermionic action clearly is gauge invariant. The field strength tensor transforms just like the covariant derivative, $F_{\nu\rho}(x) \to \Omega(x)F_{\nu\rho}\Omega^\dagger(x)$. As the integrand in the gauge action essentially contains a trace in color space via $\mathrm{Tr}(F_{\nu\rho}F^{\nu\rho}) = \frac{1}{2}F^a_{\nu\rho}F^{a\nu\rho}$, the cyclic property of the trace ensures that also this action is invariant under gauge transformations.

Among the many fascinating properties of QCD are confinement and asymptotic freedom. Confinement means that quarks cannot be observed individually, but only within bound states, i.e., hadrons. Asymptotic freedom is closely linked to the *running* of the coupling $\alpha_S = g^2/4\pi$. Namely, the value of the coupling depends on the energy scale. In particular, for QCD it was found that the coupling decreases to zero when the energy scale goes to infinity[24,25]; hence the term asymptotic freedom. The way in which the coupling changes with the energy scale is dictated by the so called *beta* function. It can be calculated order by order by perturbative means. To lowest nontrivial order the beta function of a Yang-Mills theory including fermions is[24–26]

$$\beta(\mu) = \mu^2 \frac{d\alpha_S(\mu)}{d\mu^2} = \frac{\alpha_S(\mu)}{4\pi}\left(-\frac{11N}{3} + \frac{2N_f}{3}\right) + \mathcal{O}(\alpha_S^3). \qquad (1.6)$$

Here μ is the energy scale, N the order of the gauge group $SU(N)$, and N_f the number of fermion flavors. As long as $N_f < 11N/2$, the coefficient of α_S remains negative and thus the theory is asymptotically free.

From this it can be seen that perturbation theory in QCD works best at high energies. For the same reason perturbative results become unreliable at low energies. In that case the coupling α_S becomes large, $\mathcal{O}(1)$, and is thus no longer a suitable expansion parameter. Also it has been known at least since the conception of instantons in the 1970s that quantum field theories can have nonperturbative aspects, which by their very nature are excluded in a perturbative treatment. The next section is devoted to lattice regularization, which is a nonperturbative treatment of quantum field theories.

1.1.1 Lattice regularization

As was already mentioned, the path integral is not a well defined object. Hence the need for some form of regularization arises. Also for a numerical treatment the oscillating phase in the integrand, e^{iS}, is untractable. Therefore what is commonly done is to work in Euclidean or imaginary time, that is, $t \to it$. As a result, the phase factor turns into an exponential factor, $e^{-S_{\text{Eucl}}}$, with the Euclidean action S_{Eucl}. In the Euclidean formulation the path integral can be viewed as a sum/integral over different configurations, each of which has a probability assigned according to the exponential factor. In the following S will refer to the Euclidean action, as we are no longer concerned with the real time action. Further it has to be noted that working in Euclidean time only gives access to equilibrium physics, i.e., dynamic processes are not covered by this approach.

There are two types of divergencies occurring in the path integral. On the one hand there are ultra-violet (UV) divergencies, and on the other there are infrared (IR) divergencies. The former come from the fact that arbitrary large momenta can occur in a continuous space. The latter are due to the circumstance that in an infinite space arbitrary large wavelengths can appear.

The IR divergencies can be eliminated by putting the system into a finite box with volume V, which naturally gives a lower bound for the maximum wavelengths allowed. The UV divergencies can be cured by discretizing the space with a lattice constant a, as this leads to a momentum cutoff of $p_{\max} \sim 1/a$. In order to recover the continuum theory, the continuum limit, $a \to 0$, as well as, the thermodynamic limit $V \to \infty$ have to be performed. (It has to be noted that in general these limits do not commute.) In the following we again consider QCD as an example of a lattice regularization.

To define the theory on a space time lattice, also the action has to be discretized. In QCD the action consists of two separate parts, the gauge action S_g and the fermion action S_f; these can be treated separately. We follow the presentation in [23].

1.1.1.1 Plaquette action

First we consider the gauge action S_g. In the continuum the gauge field $A_\nu(x)$ lives in the $su(3)$-algebra, which is defined locally around the point x. On the lattice it is natural to use gauge transporters,

$$U_\nu(x) = P\exp\left(i \int_x^{x+a\hat{\nu}} dx'_\nu A_\nu(x') \right) \in SU(3), \tag{1.7}$$

instead, as they 'accumulate' the gauge field from one site to the next. (Pexp denotes the path ordered exponential.) Practically one can also use $U_\nu(x) = \exp(iaA_\nu(x))$ because the difference is only of $\mathcal{O}(a)$ and is therefore not important in the continuum limit. In the literature U_ν is called a *gauge link* for obvious reasons. Under a gauge transformation $\Omega(x) \in SU(3)$ they transform as $U_\nu(x) \to \Omega(x)U_\nu(x)\Omega^\dagger(x + a\hat{\nu})$.
With the help of the gauge links we can define a plaquette

$$P_{\nu\rho}(x) = U_\nu(x)U_\rho(x + a\hat{\nu})U^\dagger_\nu(x + a\hat{\rho})U^\dagger_\rho(x), \tag{1.8}$$

which describes a closed loop of link variables. The plaquette or Wilson action is then defined as the sum over all traced plaquettes on the lattice,

$$S_g[U] = \frac{\beta}{3} \sum_x \sum_{\nu<\rho} \Re \operatorname{Tr}(1 - P_{\nu\rho}(x)). \tag{1.9}$$

The cyclic property of the trace renders the action gauge invariant, since the plaquette transforms like $P_{\nu\rho}(x) \to \Omega(x)P_{\nu\rho}(x)\Omega^\dagger(x)$ under a gauge transformation $\Omega \in SU(3)$. It can be shown that in the limit $a \to 0$ the plaquette reduces to

$$\begin{aligned} P_{\nu\rho} &= \exp(ia^2(\partial_\nu A_\rho - \partial_\rho A_\nu + i[A_\nu, A_\rho]) + \mathcal{O}(a^3)) \\ &= \exp(ia^2 F_{\nu\rho} + \mathcal{O}(a^3)). \end{aligned} \tag{1.10}$$

Thus we can write that for $a \to 0$ the plaquette action becomes

$$\begin{aligned} S_g[U] &= \frac{\beta}{3} \sum_x \sum_{\nu<\rho} \Re \operatorname{Tr}(-ia^2 F_{\nu\rho}(x) + i\mathcal{O}(a^3) + \frac{a^4}{2} F^2_{\nu\rho} + \mathcal{O}(a^6)) \\ &= \frac{\beta}{3} \frac{a^4}{4} \sum_x \sum_{\nu,\rho} \left(\operatorname{Tr}(F^2_{\nu\rho}) + \mathcal{O}(a^2) \right), \end{aligned} \tag{1.11}$$

where the a^2 and a^3 terms have been eliminated by only taking the real part. For $a \to 0$ the sum turns into an integral, $a^4 \sum_x \to \int d^4x$, such that the continuum action is recovered, provided we set the lattice coupling to $\beta = 6/g^2$.
The Wilson action is the most simple lattice action that converges to the right continuum action for QCD. There are also various *improved*

forms for this action. Namely, one can add other terms to the lattice action that vanish in the continuum limit. This can be used to achieve a faster convergence to the continuum, e.g., by canceling the $\mathcal{O}(a^2)$ term in eq. (1.11), such that the action approaches the continuum as $\mathcal{O}(a^3)$. An example for this is the *Lüscher-Weisz* action[27].

1.1.1.2 Fermion action

Next we consider the discretization of the fermion action. The simplest discretization of the Dirac operator reads

$$\not{D} \xrightarrow{\text{discr}} D_{x,y} = \sum_{\nu} \gamma_\nu \left(\frac{U_\nu(x)\delta_{x+a\hat{\nu},y} - U_\nu^\dagger(y)\delta_{x-a\hat{\nu},y}}{2a} \right). \quad (1.12)$$

Here the γ-matrices satisfy $\{\gamma_\nu, \gamma_\rho\} = 2\delta_{\nu\rho}$, since we work in Euclidean spacetime. The gauge links serve to make the expression, $\sum_{x,y} \bar{\psi}(x) D_{x,y} \psi(y)$, invariant under gauge transformations $\Omega(x) \in SU(3)$. Nevertheless, there is the problem of so called *fermion doubling*, that is, the naive discretization actually corresponds to more than one flavor of fermions.

This can be seen most easily in the free case, where all $U_\nu(x) \equiv 1$. Performing a Fourier transform yields the massless Dirac operator in momentum space

$$\tilde{D}_{p,q} = \delta(p-q) \frac{i}{a} \sum_{\nu} \gamma_\nu \sin(p_\nu a). \quad (1.13)$$

Its inverse is the *fermion propagator* in the massless case:

$$\tilde{D}^{-1}_{p,q} = \delta(p-q) \frac{-\frac{i}{a} \sum_\nu \gamma_\nu \sin(p_\nu a)}{\frac{1}{a^2} \sum_\nu \sin^2(p_\nu a)}. \quad (1.14)$$

The pole of the propagator is associated with the mass of the fermion, i.e., zero in this case. Nevertheless, eq. (1.14) shows that in addition to the continuum pole, $p = 0$, there are also other (unphysical) poles for all the different combination of $p_\nu = \pi/a$ and $p_\nu = 0$. Thus the discretized version represents 2^d different fermions, where d is the spacetime dimension. This is a consequence of the Nielsen-Ninomiya theorem[28].

There have been a number of proposals for eliminating these doublers over the years. Among the first of these was Wilson's construction, which works by adding a second derivative term. In order to match the

dimensionality of the first derivative term, the second derivative term has to be multiplied by the lattice spacing a, thus ensuring that this term does not affect the continuum limit. The net effect of this additional term is to make the unphysical poles with one or more $p_\nu = \pi/a$ infinitely heavy ($m_{pol} \sim 1/a$) in the continuum limit.

Another way of reducing the number of doublers is due to Kogut and Susskind. Namely, the number of doublers can be reduced by choosing a spin-diagonal basis for the fermions ψ. Let $n = x/a \in \mathbb{N}^4$ be a lattice vector. The fermions can be transformed to a new basis ψ' via

$$\begin{aligned} \psi(x) &= \gamma_0^{n_0}\gamma_1^{n_1}\gamma_2^{n_2}\gamma_3^{n_3}\psi'(x), \\ \bar{\psi}(x) &= \bar{\psi}'(x)\gamma_3^{n_3}\gamma_2^{n_2}\gamma_1^{n_1}\gamma_0^{n_0}. \end{aligned} \tag{1.15}$$

For the γ-matrices the relation $\gamma_\nu^2 = 1$ holds. When the Dirac operator in eq. (1.12) is sandwiched between the fermion fields, $\sum_{x,y} \bar{\psi}(x) D_{x,y} \psi(y)$, the two fields are shifted by one unit in the ν-direction. Thus there is a mismatch in the powers of γ-matrices, but this mismatch is cured by the prefactor γ_ν. Commuting this one past the others to the correct place introduces a minus sign,

$$\eta_\nu(x) = (-1)^{\sum_{\rho<\nu} n_\rho}, \tag{1.16}$$

the so called *staggered phase*. Now all the γs square to 1 and the fermion action reads

$$\begin{aligned} \sum_{x,y} \bar{\psi}(x) D_{x,y} \psi(y) &= \sum_{x,y} \bar{\psi}'(x) D'_{x,y} \psi'(y) \\ D'_{x,y} &= \sum_\nu \eta_\nu(x) \frac{U_\nu(x)\delta_{x+a\hat{\nu},y} - U_\nu^\dagger(y)\delta_{x-a\hat{\nu},y}}{2a} \mathbb{1}, \end{aligned} \tag{1.17}$$

where the $\mathbb{1}$ indicates that D' is diagonal in Dirac space. It is therefore sufficient to only use one of the spinor-components. This means that the doubling problem is reduced by the dimension of the representation for the γ-matrices. For QCD in $d = 4$ dimensions the γs are 4×4 matrices; thus the doubling problem is reduced to 4 doublers.

Denoting with χ just one spinor component, the *staggered* fermion action can be written

$$S_f^{st} = a^4 \sum_{x,y} \bar{\chi}(x)(D_{x,y}^{st} + m\delta_{x,y})\chi(y), \tag{1.18}$$

$$D_{x,y}^{st} = \sum_\nu \eta_\nu(x) \frac{U_\nu(x)\delta_{x+a\hat{\nu},y} - U_\nu^\dagger(y)\delta_{x-a\hat{\nu},y}}{2a}. \tag{1.19}$$

1.1.1.3 QCD partition function

Combining the gauge part and the fermion part of the action, we can write the partition function using staggered fermions[1]. The fermions are Grassmann numbers, that is, they anticommute. This makes them hard to treat numerically. Nevertheless, they can be integrated analytically, with the familiar integration prescription

$$\int d\xi = 0, \qquad \int d\xi\, \xi = 1, \tag{1.20}$$

for a Grassmann number ξ. Now the fermion fields in the partition function can be integrated out giving a determinant[29]:

$$\begin{aligned} \mathcal{Z} &= \int \mathcal{D}U \mathcal{D}\chi \mathcal{D}\bar{\chi}\; e^{-S_g[U] - S_f^{st}[U,\chi]} \\ &= \int \mathcal{D}U\; \det(D^{st}[U] + m) e^{-S_g[U]}. \end{aligned} \tag{1.21}$$

In the discretized setting, the integration measure has a well defined meaning; namely, an integration is performed at every point of the finite spacetime lattice, e.g., $\mathcal{D}U \equiv \prod_{x,\nu} dU_\nu(x)$, where dU_ν denotes the Haar measure of $SU(3)$. The determinant still corresponds to more than one fermion. To circumvent this, the so called rooting trick can be applied[30]; namely, instead of using the determinant, the fourth root of the determinant can be used, which is supposed to correspond to only one flavor in QCD in four dimensions.

1.1.1.4 Connection to thermodynamics

Field theory in Euclidean spacetime has a strong resemblance to statistical mechanics and hence also thermodynamics. The partition function of a thermodynamical system with temperature T can be written as

$$\mathcal{Z}(T) = \mathrm{Tr}\left(e^{-\hat{H}/T}\right), \tag{1.22}$$

where the trace goes over all eigenstates of the Hamiltonian of the system. However, the trace can also be computed by going to the basis

[1] At least in studying nonzero temperature QCD on the lattice, staggered fermions have proven to be sufficient.

of the field variables, Φ, instead. This transformation naturally leads to the path integral representation of the partition function[23,31]

$$\mathcal{Z}(T) = \int \mathcal{D}\Phi \; e^{-S(T)}, \tag{1.23}$$

where S is the Euclidean action corresponding to the Hamiltonian, which can be expressed as an integral over a Lagrange density $\mathcal{L}(\Phi)$:

$$S(T) = \int_0^{1/T} dt \int d^3x \, \mathcal{L}(\Phi). \tag{1.24}$$

In this way the inverse temperature $1/T$ is associated with the temporal extent of spacetime. On the lattice the temporal extent is aN_t, while the spatial extent is aN_s, so the temperature is given by $T = 1/(aN_t)$. Thus, on the lattice, the temperature can be changed either by varying the lattice spacing a or by varying the spatial extent N_t. It is also possible to obtain a continuum limit at a given temperature, by varying a and N_t in such a way that T remains fixed.

1.1.1.5 Simulation strategies

Simulating a field theory on the lattice means performing the path integral numerically. In case of QCD we have to perform an $SU(3)$ integration for every link on the lattice. Thus the dimensionality of the integral grows with the volume, which quickly exceeds the capabilities of conventional numerical integration routines; this is known as the *curse of dimensionality*. One of the few exceptions is *Monte Carlo* integration, where the integral is approximated by evaluating the integrand at a set of random points. More concretely, in lattice simulations we are interested in expectation values of observables. An expectation value of an observable X can be approximated as

$$\langle X \rangle = \frac{1}{\mathcal{Z}} \int \mathcal{D}\Phi \, X[\Phi] e^{-S[\Phi]} \approx \frac{1}{N} \sum_{i=1}^{N} X[\Phi_i], \tag{1.25}$$

where the Φ_i are random points in field space distributed according to the measure

$$\frac{e^{-S[\Phi]} \mathcal{D}\Phi}{\mathcal{Z}}. \tag{1.26}$$

Due to the stochastic nature of this approach, the error on $\langle X \rangle$ scales like[2] $1/\sqrt{N}$. In this way the problem of integration has been shifted to the problem of how to generate field configurations distributed according to the measure in eq. (1.26).

This can be achieved by generating the field configurations as a *Markov chain*. A Markov chain is a sequence of configurations $\Phi_1 \to \Phi_2 \to ...$, i.e., each successive configuration is generated from the previous one by an updating procedure. This sequence has to obey the balance equation

$$\sum_{\Phi} T(\Phi \to \Phi') P(\Phi) = \sum_{\Phi} T(\Phi' \to \Phi) P(\Phi'), \tag{1.27}$$

where $P(\Phi)$ is the probability of being in the configuration Φ and $T(\Phi \to \Phi')$ denotes the transition probability of going from the configuration Φ to the configuration Φ'. The transition probabilities have to fulfill the reality conditions

$$0 \leq T(\Phi \to \Phi') \leq 1 \quad \text{and} \quad \sum_{\Phi} T(\Phi' \to \Phi) = 1. \tag{1.28}$$

Put into words, eq. (1.27) simply states that the rate of starting anywhere in configuration space and ending up at some particular state Φ' must match the rate going anywhere in configuration space, starting from Φ'. This ensures that the system remains in equilibrium.

One of the most widely used forms of the balance equation is *detailed balance*,

$$T(\Phi \to \Phi') P(\Phi) = T(\Phi' \to \Phi) P(\Phi'), \tag{1.29}$$

where the balance equation is fulfilled term wise. Among the most simple algorithms for updating configurations is the *Metropolis-algorithm*[32]. In its simplest form, a new field configuration Φ', generated with some symmetric probability distribution $T_0(\Phi \to \Phi') = T_0(\Phi' \to \Phi)$, is proposed. The acceptance probability is given by

$$T_A(\Phi \to \Phi') = \min\left(1, \frac{e^{-S[\Phi']}}{e^{-S[\Phi]}}\right). \tag{1.30}$$

If the new configuration Φ' is accepted, it is added to the Markov chain. If it is rejected, the old configuration Φ is added to the chain once more.

[2] Strictly speaking, the autocorrelations, inherent in this approach, have to be taken into account for this to be true.

In this way a Markov chain with the equilibrium distribution in eq. (1.26) can be constructed. In practice, starting from a given configuration, one has to perform a certain number of update steps before the equilibrium distribution is reached. Only after that the configurations can be used in the measurement of observables in eq. (1.25).

There are also a number of other algorithms commonly used in lattice simulations. Among these are the Hybrid Monte Carlo algorithm[33] and the worm algorithm[34], to name just two. For more details on the theoretical basis of Markov chain Monte Carlo as well as the updating algorithms involved the reader is referred to standard textbooks and review articles, e.g., [23,35–37].

1.1.2 $CP(N-1)$ models

One class of nonlinear sigma models is that of the $CP(N-1)$ models. In two dimensions they display a number of features, such as asymptotic freedom and dynamic mass generation, which we usually associate with non-Abelian gauge theories, in particular QCD. In higher dimensions[3] $CP(N-1)$ can be treated as an effective field theory defined with a suitable cutoff scale Λ.

1.1.2.1 Continuum formulation

The continuum action for $CP(N-1)$ reads

$$S_{\text{cont,A}} = \frac{1}{g^2} \int d^d x \, (D_\nu n)^\dagger (D_\nu n), \tag{1.31}$$

where n is a complex N-component field, constrained to $n^\dagger n = 1$. This constraint is responsible for all the interesting dynamics of $CP(N-1)$ models. Without it, it would be a trivial theory of free complex scalar fields. The constraint, however, establishes the nonlinear nature of the model. The covariant derivative $D_\nu = \partial_\nu + \mathrm{i}A_\nu$ makes eq. (1.31) $U(1)$ gauge invariant. Note that only in two dimensions the coupling g is dimensionless and thus the theory is renormalizable perturbatively in two dimensions.

There is no field strength for the gauge field A present, therefore A can be substituted by its equation of motion

[3] It is still a current topic of research whether $CP(N-1)$ in higher dimensions may be renormalizable nonperturbatively, as suggested in [38].

$$A_\nu = \mathrm{i}\, n^\dagger \partial_\nu n. \tag{1.32}$$

Thus there is an equivalent action, containing only the n-field:

$$S_{\mathrm{cont}} = \frac{1}{g^2} \int d^d x \, \left[(n^\dagger \partial_\nu n)^2 + (\partial_\nu n^\dagger)(\partial_\nu n) \right]. \tag{1.33}$$

Fermions ψ can be coupled to the system via minimal coupling, i.e., by adding a term,

$$\bar{\psi}(\gamma_\nu(\partial_\nu + \mathrm{i}A_\nu) + m)\psi, \tag{1.34}$$

to the action.

1.1.2.2 Lattice formulation

There are two main courses of action for a non-perturbative treatment of $CP(N-1)$: One is the large N expansion[39] and the other is the lattice formulation. For the purpose of studying Anderson localization in $CP(N-1)$ numerically, the lattice formulation is preferable.

We can replace the covariant derivative with a finite difference, $D_\nu n \to U_{x,\nu} n_{x+\hat{\nu}} - n_x$; the resulting lattice action reads

$$S_{\mathrm{latt,U}} = -N\beta \sum_{x,\nu} (n_x^\dagger U_{x,\nu} n_{x+\hat{\nu}} + n_{x+\hat{\nu}}^\dagger U_{x,\nu}^\dagger n_x). \tag{1.35}$$

Provided we identify $N\beta \equiv 1/g^2$ and $U_{x,\nu} \equiv \mathrm{e}^{\mathrm{i}aA_\nu(x)}$, where a denotes the lattice spacing, this action reduces to the continuum action in eq. (1.31), when $a \to 0$. (Apart from an additive constant.)

There is also the so called *quartic* action, corresponding to the continuum action containing only the n-field in eq. (1.33):

$$S_{\mathrm{latt,quartic}} = -N\beta \sum_{x,\nu} |n_{x+\hat{\nu}}^\dagger n_x|^2. \tag{1.36}$$

Expanding this action to order a^2 gives (1.33), again with an additive constant.

1.2 Random matrix theory

Random matrix theory (RMT) customarily studies the statistic properties of random Hermitian matrices $H = H^\dagger$, whose matrix elements are Gaussian distributed according to the weight

$$w(H) = e^{-\operatorname{Tr} H^2}. \tag{1.37}$$

This gives rise to the joint eigenvalue distribution

$$\rho(\lambda_1, ..., \lambda_n) \sim \prod_{i<j} |\lambda_i - \lambda_j|^\beta \, e^{-\frac{\beta}{2} \sum_i \lambda_i^2}, \tag{1.38}$$

where $\beta = 1, 2, 4$. The value of β depends on the symmetry of the random matrix ensemble. More details on random matrix theory can be found in [40,41]. Under time reversal symmetry $\mathcal{T}$ there are three distinct symmetry classes possible:

- H can be symmetric under $\mathcal{T}$, in which case it is said to be in the Gaussian orthogonal ensemble (GOE, $\beta = 1$). H can be represented by *real, symmetric* matrices.
- H can have no symmetry properties under $\mathcal{T}$, in which case it is said to be in the Gaussian unitary ensemble (GUE, $\beta = 2$). H can be represented by *complex, Hermitian* matrices.
- H can be antisymmetric under $\mathcal{T}$, in which case it is said to be in the Gaussian symplectic ensemble (GSE, $\beta = 4$). H can be represented by *quaternion, symplectic* matrices.

Here we will mainly focus on the GUE, since both QCD and $CP(N-1)$ belong to this class.

A common observable is the level spacing statistics $P(s)$. It measures the probability that two adjacent eigenvalues are a distance s apart. Strictly speaking, $P(s)$ is only defined for a spectrum with a constant spectral density. In order to calculate $P(s)$ also for other spectra, these have to be unfolded first. This means that the original eigenvalues λ have to be rescaled by dividing out the local spectral density $\rho(\lambda)$, resulting in eigenvalues $\bar{\lambda}$ for which $\rho(\bar{\lambda}) = const$, getting rid of scales specific for the models in question. One way to do this is to put all the eigenvalues into a single list and sort that list in ascending order, keeping track of the eigenvalues while doing so[42]. The unfolded spectrum is then obtained by replacing the eigenvalues with their indices in the list. It has to be noted that this method only works if there are many sets of eigenvalues from different random matrices available, for a single set of eigenvalues this procedure does not work.

For 2×2-matrices in the GUE the level spacing can be obtained by multiplying eq. (1.38) with the delta function $\delta(\lambda_1 - \lambda_2 - s)$ and integrating over the eigenvalues λ_1, λ_2. The result is

$$P(s) = \frac{32}{\pi^2} s^2 e^{-\frac{4}{\pi}s^2}. \tag{1.39}$$

This formula is called the Wigner surmise for the GUE. In fact the constant in front, $32/\pi^2$, as well as the constant in the exponent, $4/\pi$, are uniquely determined by the conditions

$$\int_0^\infty ds\, P(s) = 1 \quad \text{and} \quad \int_0^\infty ds\, sP(s) = 1. \tag{1.40}$$

This is the level spacing distribution for 2×2-matrices; for larger matrices a closed form expression becomes increasingly difficult to obtain. Nevertheless, it is known that for larger matrices the Wigner surmise is a good approximation[43,44]. The most notable feature of the level spacing distribution is the so called level repulsion. Namely, the probability of finding two adjacent eigenvalues a distance $s = 0$ apart vanishes. This finding is highly nontrivial: for example using the eigenvalues themselves instead of the matrix elements as random variables leads to a Poissonian level spacing distribution, $P(s) = e^{-s}$, which has its maximum at $s = 0$. For comparison Figure **1.1** shows the level spacing distribution for Poissonian distributed eigenvalues as well as the Wigner surmise for the three Gaussian ensembles.

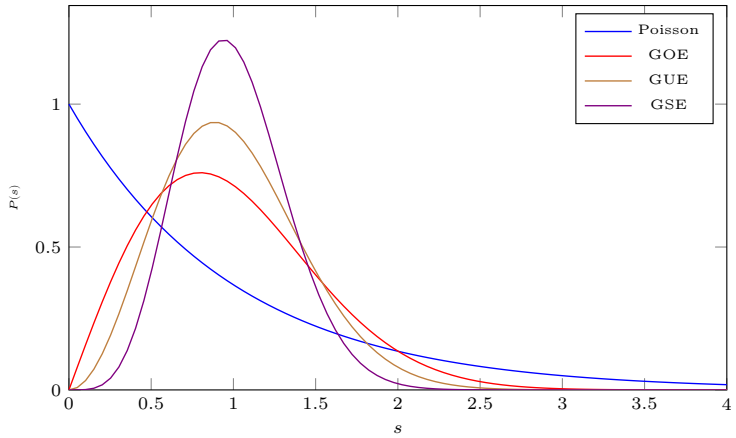

Figure 1.1 The level spacing distribution for the three Gaussian ensembles as well as for the Poissonian case. For the GUE see eq. (1.39).

Another, more recent, observable is the distribution of the ratio of consecutive level spacings[45]. Namely, the distributions $P(r)$ and $P(\tilde{r})$ are considered, where

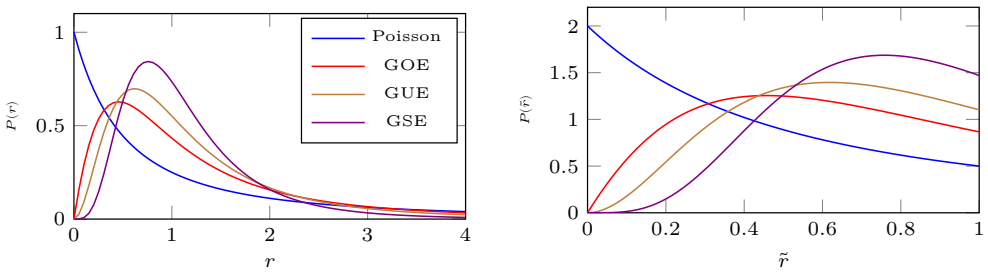

(a) (b)

Figure 1.2 The distribution of the r and $\tilde{r}$ of consecutive level spacings. For the GUE see eq. (1.41).

$$r = \frac{s_n}{s_{n-1}}, \quad \tilde{r} = \frac{\min(s_n, s_{n-1})}{\max(s_n, s_{n-1})}, \quad s_n = \lambda_{n+1} - \lambda_n.$$

Since consecutive spacings share the same local spectral density, no unfolding is needed when taking the ratio. The distributions $P(r)$ and $P(\tilde{r})$ are not independent, as for $P(\tilde{r})$ all values with $r > 1$ are added to the distribution at $1/r$, giving the relation $P(\tilde{r}) = 2P(r)\Theta(1-r)$. For the equivalent of the Wigner surmise, 3×3—matrices have to be used. The result for the GUE is given by[45]

$$P(r) = \frac{81\sqrt{3}}{4\pi} \frac{(r+r^2)^2}{(1+r+r^2)^4}. \tag{1.41}$$

For comparison Figure **1.2** shows $P(r)$ and $P(\tilde{r})$ for the three Gaussian ensembles as well as for the Poissonian case, which has $P(r) = 1/(1+r)^2$. Most notable is the fact that for small arguments the behavior is the same as in the Wigner surmise, i.e., there is level repulsion at small distances. However, even though the graphs for $P(r)$ and $P(s)$ look quite similar, the latter has an exponential decay, while the former decays only algebraically. On the basis of this last fact, it can be said that for numerical studies $P(\tilde{r})$ may be more advantageous than $P(r)$. Namely, increased statistics might not result in smaller errors with $P(r)$ because the increased statistics might largely be spent on sampling the tail of the distribution.

1.3 Notation and conventions

- $[A, B] = AB - BA$: the commutator of two operators A and B.
- $\{A, B\} = AB + BA$: the anticommutator of two operators A and B.

- $A^\nu B_\nu = \sum_\nu A^\nu B_\nu$: the Einstein sum convention is used, if not otherwise indicated.
- γ_ν: the Dirac γ-matrices. Depending on the context, they obey $\{\gamma_\nu, \gamma_\rho\} = 2g_{\nu\rho}$ in Minkowski spacetime or $\{\gamma_\nu, \gamma_\rho\} = 2\delta_{\nu\rho}$ in Euclidean spacetime.
- $\not{A} = A^\nu \gamma_\nu$: the so called Feynman-slash notation.
- d: will mostly refer to the dimensionality of *spacetime*.
- μ: will, if not otherwise indicated, refer to the chemical potential in lattice units.

2 Anderson localization

Anderson localization is among the most widely studied effects in condensed matter theory. Its inception was in 1958 when Anderson proposed a simple model in order to describe the metal insulator transition[46]. Since then a wide range of similar models have been analyzed. Let us first review a number of basic properties of Anderson localization, including a motivation for the Anderson model as well as some of the techniques used to differentiate between localized and delocalized modes.

2.1 Introduction

A regular lattice with a periodic potential gives rise to Bloch-waves as eigenstates, which are by their very nature delocalized objects. These are then naturally involved in transport phenomena. Intuitively, it is obvious that impurities and lattice defects may hamper transport properties. From the perspective of a tight binding model impurities can be modeled by adding a random onsite potential. A basic tight binding model involves just nearest neighbor interactions, suggesting a Hamiltonian of the form

$$H = \sum_{<x,y>} t_{xy}|x\rangle\langle y| + \sum_x V_x|x\rangle\langle x|, \tag{2.1}$$

where the first sum is over nearest neighbors only. Here $V_x \in [-w, w]$ is the random onsite potential where w determines the strength of the disorder. The states $|x\rangle$ are position eigenstates, with $\langle x|y\rangle = \delta_{xy}$. The value of the matrix elements t_{xy} depends on the details of the model, e.g., $t_{xy} = 1$ would be a viable choice for an isotropic lattice.

2.1.1 Properties of Eigenmodes

Let ψ_λ be an eigenmode of H with eigenvalue λ. A common observable which distinguishes between localized and delocalized modes is the so called *participation ratio*:

$$PR(\lambda) = \frac{1}{V\sum_x |\psi_\lambda(x)|^4}. \tag{2.2}$$

It is straight forward to see how PR behaves for localized and delocalized modes:

$$PR(\lambda) = \begin{cases} \frac{1}{V} & \text{localized, e.g., } \psi_\lambda(x) = \delta_{x,x_0} \\ \mathcal{O}(1) & \text{delocalized, e.g., } \psi_\lambda(x) = \frac{1}{\sqrt{V}} \end{cases} \tag{2.3}$$

Namely, localized modes scale like $1/V$, while delocalized modes do not scale with the volume. There is also the possibility that an eigenmode behaves like neither of these two, in which case the mode is said to be critical[47]. Namely, a fractal dimension d_f can be defined,

$$p_\lambda(L) = \sum_x |\psi_\lambda(x)|^4 \sim L^{-d_f},$$

where L is the linear extent of the system. For a localized mode we get the intuitive result $d_f = 0$, i.e., the mode is pointlike. Delocalized modes fill the whole space, hence we have $d_f = d$, where d is the dimension of the space. Critical modes on the other hand have a fractal dimension between the two, $0 < d_f < d$.

Extended eigenmodes are strongly correlated because they are necessarily sensitive to the potential at all lattice sites. As a consequence also the eigenvalues are strongly correlated, giving rise to random matrix statistics.

2.1.2 Connection to random matrix theory

The basics of random matrix theory were already introduced in **Sec. 1.2**. Delocalized modes are found to be in either one of the three Gaussian ensembles. Localized modes, being confined to a small region of space, are largely uncorrelated. This has the consequence that also their eigenvalues are uncorrelated, giving rise to a Poissonian level spacing distribution.

There is also the possibility of mixed ensembles, which lie in two or more different symmetry classes. Physically these arise naturally when for instance a perturbation is added, which does not have the same symmetries as the original system. There is a plethora of different transition ensembles between the various symmetry classes. For Anderson localization, the most important transitions are from the Poissonian case to the orthogonal and unitary ensembles. For finite sized systems many different interpolating forms for $P(s)$ are possible, depending on the details of the system under consideration. However, the Anderson

transition is of second order, which means that the spectrum can be divided into three distinct categories: A localized part with Poissonian statistics and a delocalized part with random matrix statistics, the third part is the boundary between the other two, which are said to be critical. In the simplest case, the spectrum can simply be divided in one localized part and one delocalized part. The point in the spectrum between these is referred to as the *mobility edge* λ_c.

The mobility edge can be determined in various ways. One of these is by noting that for the level spacing, the most drastic difference between, say, the Poissonian and the unitary distribution is the small distance behavior. In this sense

$$I_{0.5}(\lambda) = \int_0^{0.5} ds\, P_\lambda(s) \approx \begin{cases} 0.39 & \text{Poisson} \\ 0.11 & \text{GUE} \end{cases} \tag{2.4}$$

is an observable which has distinctly different values for localized and delocalized modes. For QCD at critical statistics, a value $I_{0.5}(\lambda_c) \approx 0.186$ was found[48]. In practice, $I_{0.5}(\lambda)$ will change smoothly between these two values while λ is swept by the mobility edge λ_c. Nevertheless, for larger system volumes, this transition will become steeper and steeper, and we can determine λ_c by the inflection point of these curves.

2.2 Anderson localization in QCD with a magnetic field

The following section is based on unpublished work in collaboration with Falk Bruckmann, Gergely Endrődi, Matteo Giordano, Sandor Katz, Tamás Kovács, and Ferenc Pittler.

In recent years the effect of a background magnetic field on QCD has been studied extensively[9,10,13,49,50]. The thermodynamic properties were of particular interest. Namely, what is the influence of a magnetic field on the transition from the confining low temperature phase to the deconfined high temperature phase. The most striking finding was inverse magnetic catalysis around the transition temperature, that is, there the chiral condensate is decreased. At all other temperatures magnetic catalysis is observed. The net effect is that the transition temperature is decreased under the influence of a magnetic field, as has been shown in various works[9,11,51] concerning the QCD phase diagram

in the $B-T$ plane; see also **Chapter 3** for other references concerning QCD in a magnetic field.

It has been speculated for a long time that the localization properties of quark eigenmodes may play a role in spontaneous chiral symmetry breaking[52–54]. Subsequent studies[15–18,48,55–57] have shown that there is, indeed, an Anderson transition taking place in the spectrum of the high temperature QCD Dirac operator. Above the deconfinement temperature a non-zero mobility edge could be defined, which was found to increase with the temperature (almost) linearly. The temperature where the mobility edge becomes zero agrees with the deconfinement temperature of $T \approx 160\,\mathrm{MeV}$[4].

2.2.1 The effect of a magnetic field on the spectrum

A remaining question is the influence of a magnetic field on the localization properties of Dirac eigenmodes. The numerical results presented here are from 6×24^3 lattices with physical quark masses. More details on the lattice setup can be found in [9,58].

The effect of the magnetic field in QCD is twofold: On the one hand, the observable may depend on the magnetic field explicitly, which is called the *valence effect*. On the other hand, the magnetic field changes the distribution of the gauge configurations through the fermion determinant; this is called the *sea effect*. Here we will only be concerned with the valence effect on the spectrum.

The flux Φ of a constant magnetic field $\vec{B} = B\vec{e}_z$ in a periodic space of physical size $L_x L_y$ is quantized[59,60] according to

$$\Phi = qBL_xL_y = 2\pi N_b, \tag{2.5}$$

where q is the electric charge and N_b is called the *magnetic flux quantum*. Thus on a given lattice it is only possible to simulate discrete values of the magnetic field. For intermediate values of the magnetic field one has to interpolate between the discrete values. Also the lattice spacing naturally places an upper bound on the maximum value of the magnetic field: $qB_{\max} = 2\pi/a^2$.

The chiral condensate is defined as the expectation value

$$\langle\bar{\psi}\psi\rangle = \frac{1}{V}\frac{d\log(\mathcal{Z})}{dm} = \frac{1}{V\mathcal{Z}}\int \mathcal{D}U\mathcal{D}\bar{\psi}\mathcal{D}\psi\ \bar{\psi}\psi\, e^{-S_g-\bar{\psi}(\not{p}+m)\psi}. \tag{2.6}$$

For our purposes, the spectral representation is more useful, which can be obtained as follows:

$$\begin{aligned}
\langle\bar{\psi}\psi\rangle &= \frac{1}{V}\frac{d\log(\mathcal{Z})}{dm} \\
&= \frac{1}{V\mathcal{Z}}\int \mathcal{D}U\mathcal{D}\bar{\psi}\mathcal{D}\psi\ \ \mathrm{Tr}\frac{1}{\not{D}+m}\, e^{-S_g-\bar{\psi}(\not{D}+m)\psi} \\
&= \frac{1}{V\mathcal{Z}}\int \mathcal{D}U\mathcal{D}\bar{\psi}\mathcal{D}\psi\ \ \mathrm{Tr}\frac{\not{D}-m}{\not{D}^2-m^2}\, e^{-S_g-\bar{\psi}(\not{D}+m)\psi} \\
&= \frac{1}{V\mathcal{Z}}\int \mathcal{D}U\mathcal{D}\bar{\psi}\mathcal{D}\psi\ \ \int d\lambda\frac{m\rho(\lambda)}{\lambda^2+m^2}\, e^{-S_g-\bar{\psi}(\not{D}+m)\psi} \\
&= \frac{1}{V}\left\langle\int d\lambda\frac{m\rho(\lambda)}{\lambda^2+m^2}\right\rangle. \qquad (2.7)
\end{aligned}$$

Here the fact that $\not{D}$ is traceless and γ_5-hermiticity have been used, where $i\lambda$ is the eigenvalue corresponding to $\not{D}$ and $\rho(\lambda)$ is the spectral density. In the chiral limit ($m \to 0$) this immediately gives the Banks-Casher relation

$$\langle\bar{\psi}\psi\rangle \sim \rho(0), \qquad (2.8)$$

which relates the condensate directly to the spectral density at zero eigenvalue. At non-zero mass it can still be argued that the eigenvalues $\lambda < m$ give the dominant contribution to the condensate.

Figure **2.1(a)** shows the spectral density at the low end of the spectrum[4]. As can be seen, the spectral density round the origin changes drastically with the temperature, in accordance with the change in the condensate. At low temperature the condensate is non-zero, as is the spectral density around the origin. As the temperature is increased gradually, a gap in the spectrum emerges, which is reflected in a (almost) vanishing condensate.

The effect of the magnetic field on the spectral density is depicted in figures **2.1(b,c,d)**. At all temperatures the spectral density is increased by the magnetic field. At low temperature this clearly induces magnetic catalysis. Around the transition temperature the spectral density just vanishes at $B = 0$. As the magnetic field increases the spectral gap closes, resulting in magnetic catalysis. This is only the valence effect,

[4] Only a small portion of the spectrum around the origin was computed, hence $\rho(\lambda)$ is cut off at some point in the spectrum.

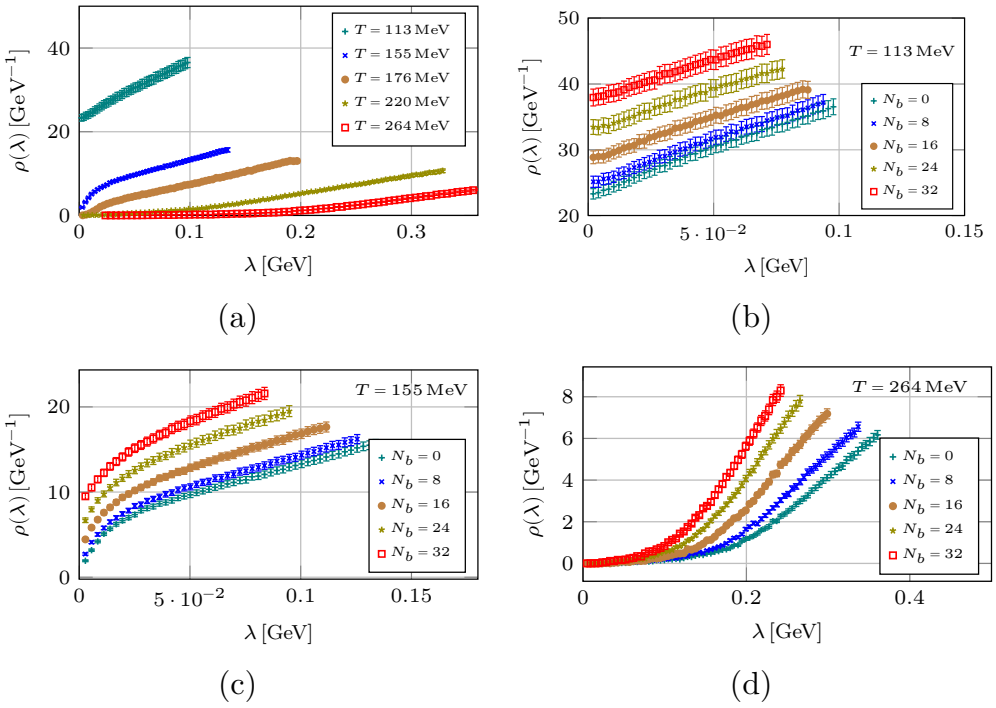

Figure 2.1 The spectral density at the low end of the Dirac spectrum. (a) The spectral density at different temperatures. (b) The spectral density at $T = 113\,\text{MeV}$ for different magnetic fluxes N_b. (c) The spectral density at $T = 155\,\text{MeV}$ for different magnetic fluxes N_b. (d) The spectral density at $T = 264\,\text{MeV}$ for different magnetic fluxes N_b.

which is usually the dominating one. Near T_c, however, the situation is different: namely, the closing of the gap with the magnetic field changes the fermion determinant drastically, which in turn results in a strong suppression of these particular gauge configurations. In this way the sea effect can win over the valence effect in the vicinity of the transition temperature. At high temperature the magnetic field still induces magnetic catalysis, but the magnetic field does not change the spectral density right at the origin, so the sea effect is small.

Finally, the effect of the magnetic field on the localization properties, in particular the mobility edge, can be studied. For this the integral $I_{0.5}(\lambda)$, eq. (2.4), of the level spacing distribution had to be computed at a given temperature for different values of the magnetic flux quantum N_b. From the inflection point of $I_{0.5}(\lambda)$ in the spectrum, the mobility edge λ_c was obtained at different N_b. By interpolating between the different N_bs the mobility edge at arbitrary intermediate magnetic fields could be obtained. The result is shown in Figure **2.2**. The mobility

edge rises almost linearly with temperature[61]. The magnetic field shifts the mobility edge to lower values; also this relation seems to be linear. Notice that this is in accord with the earlier findings that, when only considering the valence effect, T_c is raised by a magnetic field. (It is the sea effect that decreases the transition temperature[10].)

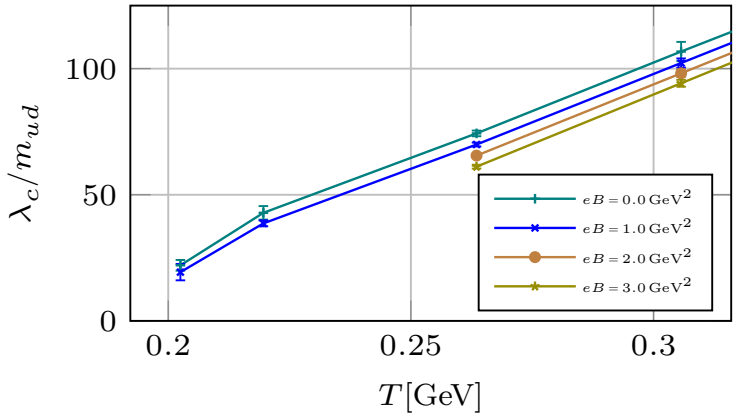

Figure 2.2 The mobility edge as a function of the temperature for different values of the magnetic field. At a given temperature the mobility edge decreases with rising magnetic field. (In order for the mobility edge to have a meaningful continuum limit, it has to be rescaled with the light quark mass m_{ud}, as both renormalize in the same way, see [62].)

2.3 An Ising-Anderson model

The toy model presented here was first proposed in [63], in order to better understand the localization mechanism in QCD. In the confined phase of QCD the eigenmodes are delocalized and the eigenvalues obey random matrix statistics, as has been known for a long time[64].

The model is based on the observation that in the high temperature phase of QCD the system is dimensionally reduced, i.e., four dimensional high temperature QCD can be described by an effective three dimensional theory. This circumstance has given rise to a wide field of effective Polyakov loop models[65].

For high temperatures the temporal extent of the lattice becomes small. Consequently, different time-slices are strongly correlated with one another. In this sense there is no additional information in having more than one time-slice. Going to the temporal gauge, all gauge links except

one can be chosen to be unity, $U_4(\vec{x}, t = 1, ..., N_t - 1) = 1$, while the remaining gauge link becomes the Polyakov loop, $U_4(\vec{x}, N_t) = P(\vec{x})$. One can go even further and also set $U_4(\vec{x}, N_t) = 1$ at the expense of changing the temporal boundary condition for the fermions to a local boundary condition:

$$\psi(\vec{x}, 1) = -P(\vec{x})\psi(\vec{x}, N_t).$$

When reducing the temporal extent to a single time-slice, this effectively introduces onsite disorder in the form of the Polyakov loop $P(\vec{x})$.

At high temperatures the Polyakov loop becomes ordered around $P(\vec{x}) = \mathbb{1}$ with small islands[51] in space where the Polyakov loop differs from $\mathbb{1}$. The idea is that the Dirac eigenmodes may get trapped/localized around these islands[66].

2.3.1 Presenting the model

The most important features inducing localization in QCD are thought to be the onsite disorder, involving continuous variables, in the form of the Polyakov loop, the fact that the disorder is strongly correlated in space, and that, as the system becomes more ordered, a gap in the spectrum develops.

Hence a model Hamiltonian is constructed as follows

$$H_{\vec{x}\vec{y}} = \gamma_4 \mathcal{N}_{\vec{x}} \delta_{\vec{x}\vec{y}} + i\vec{\gamma} \cdot \vec{\partial}_{\vec{x}\vec{y}}, \quad (\partial_j)_{\vec{x}\vec{y}} = \frac{1}{2}(\delta_{\vec{x}+\hat{\jmath},\vec{y}} - \delta_{\vec{x}-\hat{\jmath},\vec{y}}), \quad (2.9)$$

where the onsite noise $\mathcal{N}_{\vec{x}}$ has the required features from above. A spin model with continuous spins obviously has these features. The simplest one of these is the Ising model with nearest neighbor interactions. Namely, the spin configurations are generated, using an auxiliary system, according to

$$\mathcal{Z}_I = \sum_{\{s_{\vec{x}}\}} e^{-\beta H_I}, \quad H_I = \sum_{<\vec{x},\vec{y}>} s_{\vec{x}} s_{\vec{y}}, \quad s_{\vec{x}} \in [-1, 1]. \quad (2.10)$$

The onsite noise is chosen to be

$$\mathcal{N}_{\vec{x}} = \Lambda \frac{1 + s_{\vec{x}}}{2}. \quad (2.11)$$

When the spins are ordered, i.e., $s_{\vec{x}} = 1$, we have $\mathcal{N}_{\vec{x}} = \Lambda$. This gives rise to a gap in the spectrum of H, as it essentially acts like a mass

term. (It is understood that the spin configurations $\{s_{\vec{x}}\}$ are generated with an infinitesimal magnetic field, thus excluding an alignment of the spins in the opposite direction, $s_{\vec{x}} = -1$.) By varying the temperature ($k_B T = 1/\beta$) of the Ising model, the ordering of the spins can be tuned, that is, at low temperatures the spins become more ordered. In this case there is a sea of spins $s_{\vec{x}} = 1$ with small islands of misaligned spins $s_{\vec{x}} \neq 1$. This is similar to the high temperature phase of QCD, where the Polyakov loop becomes ordered with small islands of differing Polyakov loops. In QCD there is only one parameter, namely the temperature, governing both the ordering of the Polyakov loops and the gap in the Dirac spectrum. In this model there are two parameters: The temperature governs the ordering of the spins, while the other coupling parameter, Λ, determines the size of the gap in the spectrum.

As it is the model has various degeneracies. Since these play no role for the purposes of localization, we can simplify the model further. From $\{\gamma_5, H\} = 0$ it follows that ψ and $\gamma_5\psi$ are both eigenmodes with opposite eigenvalue, i.e., the spectrum is symmetric (per configuration) with respect to the origin. Performing a spin diagonalization yields a staggered version of the Hamiltonian,

$$\mathcal{H}_{\vec{x}\vec{y}} = \eta_4(\vec{x})\mathcal{N}_{\vec{x}}\delta_{\vec{x}\vec{y}}\gamma_4 + i\vec{\eta}(\vec{x}) \cdot \vec{\partial}_{\vec{x}\vec{y}}\mathbb{1}. \tag{2.12}$$

Since $\mathcal{H}$ and γ_4 commute, we can let $\psi_\pm$ be a common eigenmode of the two:

$$\mathcal{H}\psi_\pm = \lambda_\pm\psi_\pm, \quad \gamma_4\psi_\pm = \pm\psi_\pm.$$

Decomposing the four-spinor $\psi_\pm$ into two-spinors

$$\psi_\pm = \begin{pmatrix} \xi_\pm \\ \pm\xi_\pm \end{pmatrix}, \quad \xi_\pm = \begin{pmatrix} \xi_\pm^{(1)} \\ \xi_\pm^{(2)} \end{pmatrix},$$

gives the four eigenvalue equations

$$\mathcal{H}^\pm\xi_\pm^{(s)} = \lambda_\pm\xi_\pm^{(s)}, \qquad s = 1, 2, \tag{2.13}$$

$$\mathcal{H}^\pm_{\vec{x}\vec{y}} = \pm\eta_4(\vec{x})\mathcal{N}_{\vec{x}}\delta_{\vec{x}\vec{y}} + i\vec{\eta}(\vec{x}) \cdot \vec{\partial}_{\vec{x}\vec{y}}. \tag{2.14}$$

Consequently, there is a twofold degeneracy of the eigenvalues in addition to the symmetry of the spectrum around the origin. For the purpose of Anderson localization it is sufficient to study only one of these four equations, e.g., the one with the reduced Hamiltonian $\mathcal{H}^+$, as the other

three equations carry no addition information. Even though in this case the spectrum is no longer exactly symmetric around the origin on a per configuration basis, this symmetry still holds in the ensemble average. This is the state of the model so far. In order to study the effects of a background magnetic field on the spectrum, the derivative in eq. (2.14) has to be modified. For a magnetic field in a periodic space, its total flux Φ must be quantized. For a constant magnetic field pointing in the z-direction, $\vec{B} = B\vec{e}_z$, this condition reads

$$\Phi = BN_xN_y = 2\pi N_b, \tag{2.15}$$

as in eq. (2.5), where the charge has been set to $q = 1$ and the magnetic field is measured in dimensionless units. On the lattice such a background magnetic field can be implemented by introducing nontrivial $U(1)$ gauge links $u_j(\vec{x})$ in the xy plane[9]. Then the derivative operator, which replaces $\vec{\partial}$ in eq. (2.14), can be written as

$$D^j_{\vec{x}\vec{y}} = \frac{1}{2}\left(u_j(\vec{x})U_j(\vec{x})\delta_{\vec{x}+\hat{\jmath},\vec{y}} - u_j^\dagger(\vec{y})U_j^\dagger(\vec{y})\delta_{\vec{x}-\hat{\jmath},\vec{y}}\right), \tag{2.16}$$

$$u_1(\vec{x}) = \exp\left(2\pi i N_b \frac{n_x}{N_xN_y}\right), \tag{2.17}$$

$$u_2(\vec{x}) = \exp\left(-2\pi i N_b \frac{n_y}{N_y}\delta_{n_x,N_x-1}\right). \tag{2.18}$$

Here the u_1 and u_2 implement the effect of the magnetic field, while the third component $u_3 = 1$. The other phases U_j can be used to tune the overall symmetry class. With $U_j = 1$, the symmetry class of the model changes when going from $B = 0$ to $B > 0$. At vanishing magnetic field the model is in the orthogonal symmetry class, see appendix in [63]. At nonvanishing magnetic field the symmetry class becomes the unitary one. In order to make the model unitary already at $B = 0$, the phases $U_j(\vec{x}) = e^{i\theta(\vec{x})}$ can be used. However, care must be taken for the distribution of $\theta(\vec{x})$: for instance, choosing θ uniformly distributed in $[-\pi, \pi]$ removes the effect of the magnetic field completely because this amounts to an integration over $U(1)$ and the u_j are just constant offsets in this respect. Hence it is important to choose a nonuniform distribution for θ, in order for the magnetic field not to be 'washed out'. One possible way is to choose a Gaussian distribution $e^{-\theta^2/(2\sigma^2)}$ with a width σ. For σ too small, the phases U_j are very close to 1; thus the model essentially remains orthogonal at $B = 0$. For σ too large,

the U_j cover $U(1)$ more or less uniformly, thus essentially removing the magnetic field. Nevertheless, there is a window $\sigma \in [0.1, 0.7]$ between these two extremes, where the model is unitary and the effect of the magnetic field still plays a role.

2.3.2 Numerical results

For the numerical simulations presented in this section, isotropic three dimensional lattices with $N_s = 12, 14, 16$ were used. The full spectrum was obtained by exact diagonalization using LAPACK. The width for the distribution of the (random) unitary phases U_j was set to $\sigma = 0.4$. The coupling constant of the Ising model was set to $\beta = 0.7$. The coupling of the fermions to the background spin configuration was $\Lambda = 2.0$.

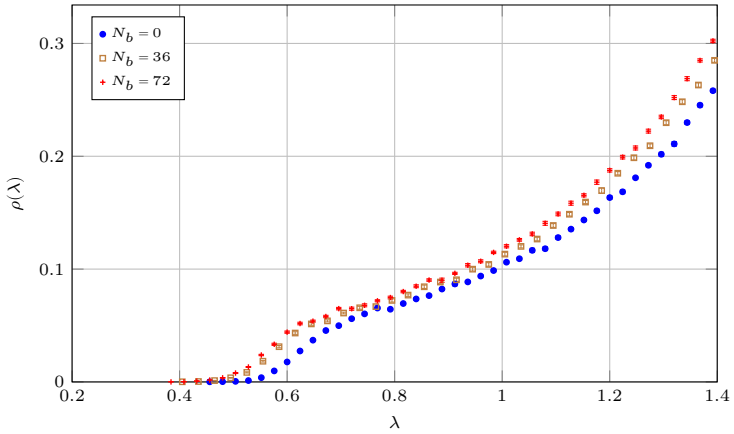

Figure 2.3 The spectral density of the Anderson-Ising model as a function of the eigenvalue for various values of the magnetic field, $N_b = 0, 36, 72$, for a lattice size of $N_s = 12$. The magnetic field shifts the spectral density to lower eigenvalues. The overall shape remains unchanged. Only at the high end of the spectrum (not shown) the spectral density is deformed, but in this region lattice artifacts dominate anyway.

First, Figure **2.3** shows the spectral density for various values of the magnetic field. (Only the positive branch of the spectrum is shown.) The overall effect of the magnetic field is to shift the spectral density to lower eigenvalues. The overall shift of the spectral density entails an enhancement of chiral symmetry breaking, i.e., magnetic catalysis. In this respect the effect of the magnetic field in the model here is very similar to the valence effect in QCD, which also shows magnetic catalysis.

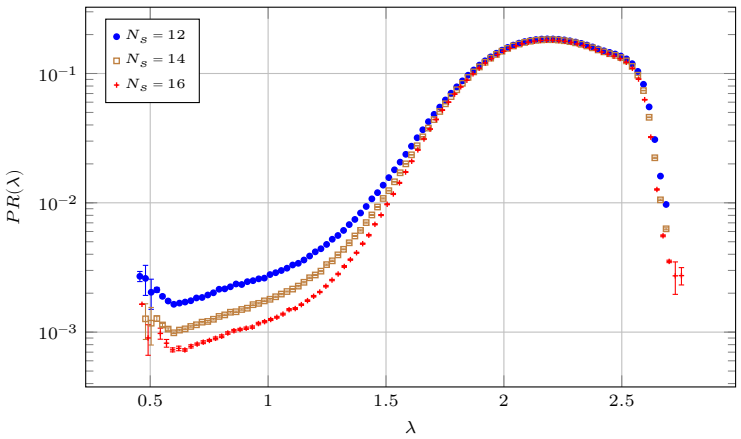

Figure 2.4 The participation ratio $PR(\lambda)$ as a function of the eigenvalue for several different volumes, $N_s = 12, 14, 16$. In the low part of the spectrum, the scaling is $PR \sim 1/V$, i.e., that part of the spectrum appears to be localized. The high part of the spectrum remains virtually unchanged, signaling delocalized modes.

In Figure **2.4** the participation ratio $PR(\lambda)$ is depicted for the three lattice sizes $N_s = 12, 14, 16$ at $B = 0$. For the low modes $PR(\lambda)$ clearly shows scaling like $1/V$, while the high end of the spectrum remains virtually unchanged. Thus the low modes show clear signs of localization, as opposed to the high modes which appear to be delocalized. Figures **2.5(a,b)** show the $PR(\lambda)$ for different values of the magnetic field at a fixed lattice size, respectively. Also here the effect of the magnetic field is to shift the curves to lower eigenvalues; with exception of the high end of the spectrum. For comparison, Figures **2.5(c,d)** show that if the $B \neq 0$ curves are shifted suitably in the horizontal direction, significant portions of the $B = 0$ and $B \neq 0$ curves overlap. Only the lowest modes show a slight increase in the PR at nonvanishing magnetic field. This suggests that the magnetic field mainly shifts the spectrum, but that the overall structure with respect to localization remains unchanged. As a consequence, the mobility edge will be shifted to lower eigenvalues by that same amount.

Figure **2.6** shows the level spacing distribution in four different spectral windows. The distribution progresses smoothly from a Poissonian one at the low end of the spectrum to the one for the GUE at the high end of the spectrum. In order to make more apparent where the transition in the spectrum takes place, Figure **2.7** shows the integral $I_{0.5}(\lambda)$ for various lattice sizes. One can see that the transition becomes steeper

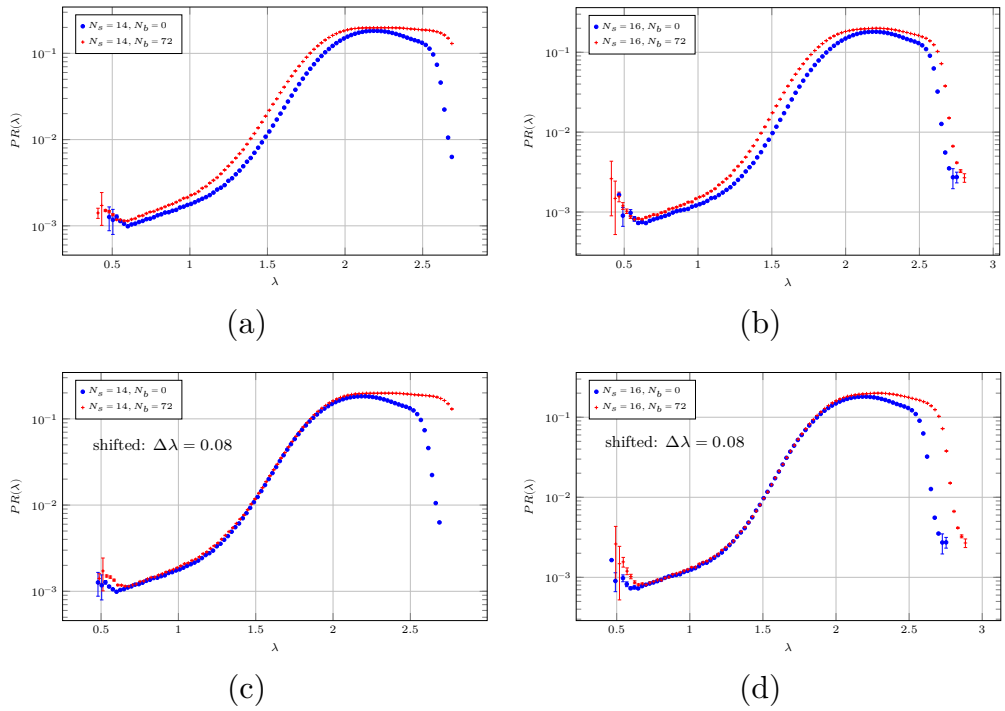

Figure 2.5 The effect of the magnetic field on the participation ratio. Also here the main effect of the magnetic field is to shift the PR to lower eigenvalues. For comparison, the $B \neq 0$ curves have been shifted by $\Delta\lambda = 0.08$ in the lower two panels; in this case significant portions of the $B = 0$ and $B \neq 0$ curves overlap.

as the volume is increased, signaling a phase transition. At around $\lambda_c \approx 1.5$ the curves for the different volumes cross each other, namely, there lies the mobility edge in the spectrum. Now also here it is the case, that the magnetic field lowers the eigenvalues in the spectrum, as can be seen from Figure **2.8**. The $B \neq 0$ curve is consistently shifted down to lower eigenvalues. The shift is also by a similar amount as was the case for the participation ratio in Figure **2.5**.

2.3.3 Remarks

The preceding sections have shown that even a very simple toy model can have similar spectral properties with respect to Anderson localization as QCD. When the underlying spin configurations are in the ordered phase, a gap develops in the spectrum. At the same time the eigenmodes at the low end of the spectrum become localized. The main effect of the magnetic field is to lower the eigenvalues. Thus also the mobility

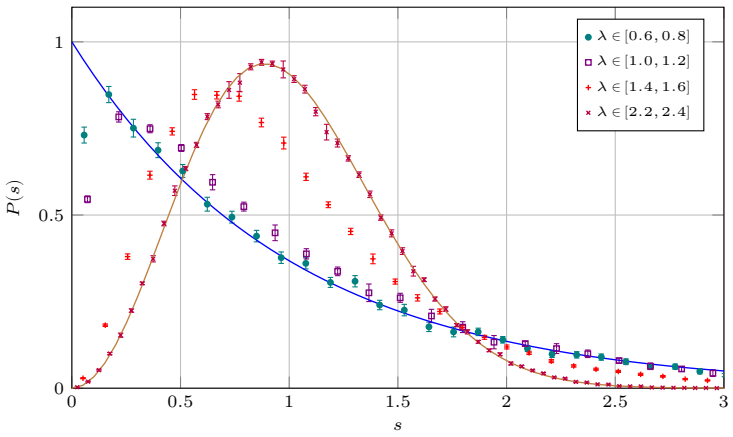

Figure 2.6 The level spacing distribution $P(s)$ of the Anderson-Ising model in different spectral windows. In the low end of the spectrum $P(s)$ is Poissonian; in the high end of the spectrum the distribution is the one for the GUE. For comparison, the curves for the Poissonian and the GUE distribution (in Wigner's approximation) are shown as solid lines.

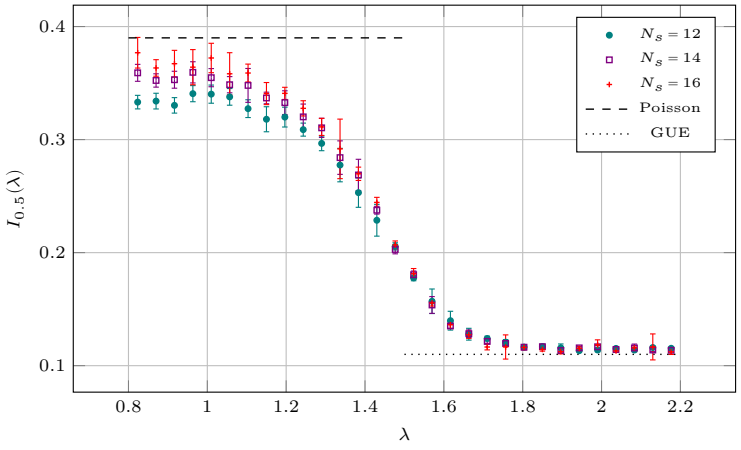

Figure 2.7 The integral $I_{0.5}(\lambda)$ for different lattice sizes. For larger volumes the transition becomes slightly steeper. The mobility edge can be inferred to be close to $\lambda_c \approx 1.5$.

edge, the point in the spectrum where the transition from localized to delocalized eigenmodes takes place, is lowered by the magnetic field. All in all this is the same as the valence effect of the magnetic field in QCD, which is responsible for magnetic catalysis by enhancing dynamical symmetry breaking.

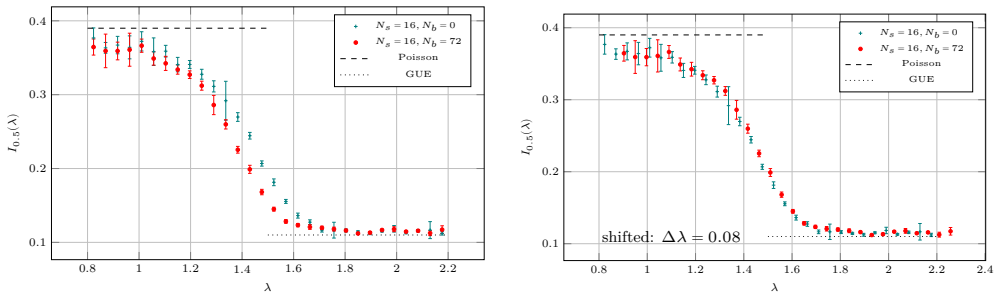

(a) (b)

Figure 2.8 The integral $I_{0.5}(\lambda)$ with and without a magnetic field. The magnetic field lowers the mobility edge. The right panel (b) shows that if the $B \neq 0$ curve is shifted to higher eigenvalues, the two curves overlap.

2.4 $CP(N-1)$ models

The following section is based on the publication [67] together with Falk Bruckmann.

In this section we will be considering Anderson localization in $CP(N-1)$ models. $CP(N-1)$ were already introduced in **Sec. 1.1.2**. Here we will only use the lattice action in eq. (1.35), with the gauge field written explicitly, since we are interested in the spectrum of the Dirac operator in the background of the gauge field. For convenience, we will denote the action in eq. (1.35) simply with S. The spectra in the following sections were either computed with LAPACK for smaller system sizes, or with SLEPc for larger system sizes.

2.4.1 Cross check

In order to verify that the setup for lattice simulations is correct, one can consider the weak and strong coupling limits of bulk observables and check whether these agree with the corresponding analytical results. One such observable is the energy density

$$E(\beta) = \frac{1}{V}\frac{\partial}{\partial\beta}\log Z(\beta) = \frac{1}{V}\frac{\partial}{\partial\beta}F(\beta) = \frac{1}{V\beta}\langle S(\beta)\rangle, \tag{2.19}$$

which can be obtained from the partition function

$$Z(\beta) = \int \mathcal{D}U \int_{n^\dagger n=1} \mathcal{D}n\mathcal{D}n^\dagger\, e^{-S(\beta)}. \tag{2.20}$$

In the strong coupling ($\beta \to 0$) limit, the energy density in two dimensions is found[68] to be

$$E_{sc}(\beta) = 4N\beta - \frac{4N^2}{N+1}\beta^3 + \frac{8N^3}{(N+1)(N+2)}\beta^5 + ..., \qquad (2.21)$$

for the lattice action in eq. (1.35). In the weak coupling expansion the energy density reads[68,69]

$$E_{wc}(\beta) = 4N - \frac{N}{\beta} - \frac{2N-1}{8N\beta^2} + ... \qquad (2.22)$$

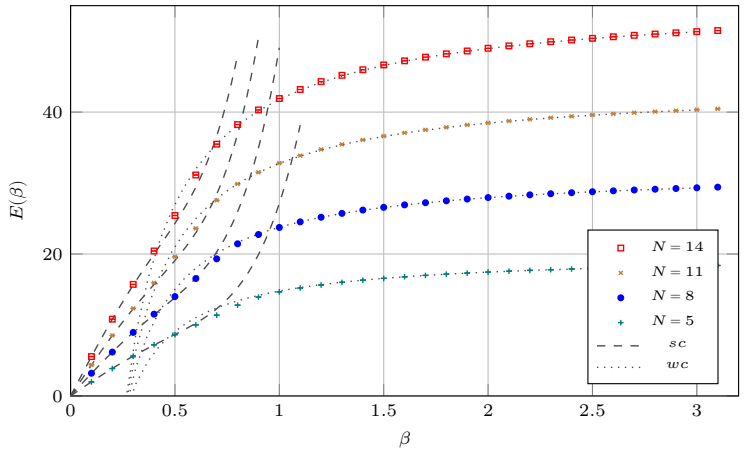

Figure 2.9 The energy density for various values of N. The corresponding strong and weak coupling expansions are also shown as dashed and dotted lines, respectively. Above $\beta \approx 0.5$ discretization effects seem to become negligible. (The numerical data is from a simulation with $N_{MC} = 10^3$ configurations and $N_{sweep} = 10^3$ sweeps between configurations on a 10×10 lattice.)

Figure **2.9** shows the energy density for different values of N. Below $\beta \approx 0.5$ the strong coupling expansion is in good agreement with the numerical data. Above $\beta \approx 0.8$ the weak coupling expansion agrees with the numerical data. In between these two values of β the numerical data interpolates smoothly between the strong and the weak coupling expansions.

2.4.2 Scale setting

In lattice simulations dimensionful quantities can only measured in units of the lattice spacing a. Therefore it is vital to know how the lattice spacing changes with lattice coupling β. This can be done by measuring the (connected) correlation function

$$G(x,y) = \left\langle \mathrm{Tr}P(x)P(y) - \frac{1}{N} \right\rangle, \tag{2.23}$$

where $P(x) = n(x)n^\dagger(x)$ is a projector along n. The exponential decay (in time direction) of the correlation function is dictated by the masses of bound states of the n-field. One thing to keep in mind is that for a given temporal extent N_t, at some point nonzero temperature effects appear via $T = 1/(aN_t)$ as the lattice spacing is decreased. Namely, for higher temperatures more and more excited states will contribute to the decay. Consequently, for a given lattice spacing, the temporal extent has to be adjusted such that the temperature remains well below the lowest mass, i.e., $T \ll m$. Secondly, the correlator above is a superposition of different momentum correlators; namely, a Fourier transform in position space gives

$$G(t_x - t_y, \vec{p}) = \sum_{\vec{x},\vec{y}} e^{i\vec{p}(\vec{x}-\vec{y})} G((t_x,\vec{x}),(t_y,\vec{y})). \tag{2.24}$$

In order to extract the rest mass of the lightest particle, we have to consider the zero momentum projected correlation function

$$G(t_x - t_y) = G(t_x - t_y, \vec{0}) = \sum_{\vec{x},\vec{y}} G((t_x,\vec{x}),(t_y,\vec{y})). \tag{2.25}$$

This has an exponential decay e^{-mL_t}, where $L_t = aN_t$ is the temporal extent in time direction. On a lattice with periodic boundary conditions, also this decay has to be periodic, which can be achieved by using the cosh. Thus in order to determine the mass m, we can fit the function

$$f(t) = A\cosh(am_{fit}(t - N_t/2)) \tag{2.26}$$

to the *zero-momentum* projected correlation function in eq. (2.25).
Another way to determine the mass is by considering the fully Fourier transformed correlation function (still at zero spatial momentum):

$$\tilde{G}(p) = \sum_t e^{ipt} G(t). \tag{2.27}$$

For small momenta it is expected that $\tilde{G}$ becomes close to the free (lattice) propagator, that is,

$$\tilde{G}(p) \sim \frac{1}{4\sin^2(ap) + (am)^2}. \tag{2.28}$$

Hence the mass can also be calculated using $\tilde{G}$ with the two lowest momenta, $p = 0$ and $p = \pi/(aN_t)$:

$$(am_{FT})^2 = 4\sin^2(\pi/N_t)\left(\frac{\tilde{G}(\frac{\pi}{aN_t})}{\tilde{G}(0) - \tilde{G}(\frac{\pi}{aN_t})}\right). \tag{2.29}$$

This one has the advantage that no fitting is needed. For small N the ratio of the masses m_{fit}/m_{FT} was found to be[70] close to 1. From the large N expansion it is expected[71] that $m_{fit}/m_{FT} \to \sqrt{2/3}$ for $N \to \infty$.

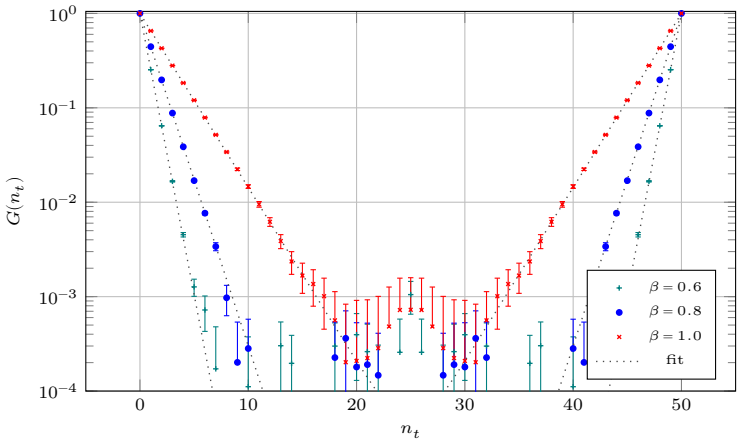

Figure 2.10 The correlation function $G(t)$ for several different couplings β at $N = 2$. The fitted curves (according to eq. (2.26)) are indicated as dotted lines. As β is increased, the decay becomes weaker, indicating that the lattice spacing becomes smaller.

Figure **2.10** shows the correlation function $G(t)$ from eq. (2.25) for several different $\beta = 0.6, 0.8, 1.0$ at $N = 2$. As β is increased, the decay becomes weaker. Figure **2.11** shows the lattice spacing as a function of the coupling β. The ratio of temperature over mass was chosen to be $T/m < 10\%$. (Up until $\beta = 1.1$ a temporal extent of $N_t = 50$ is sufficient for this.)

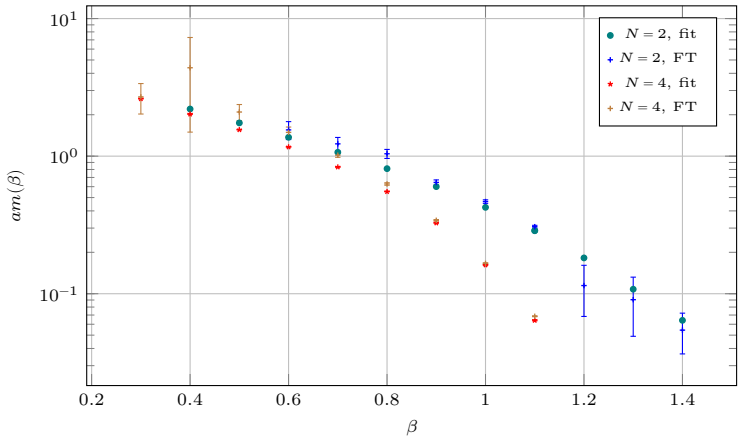

Figure 2.11 The lattice spacing a in units of a reference mass m as a function of the coupling β at $N = 2, 4$, obtained from both the fits as well as from the Fourier transform.

2.4.3 Localization in 2D

In the following we will study the spectra of the staggered Dirac operator, similar to eq. (1.19),

$$D_{xy} = \frac{1}{2}\sum_{\nu}(\eta_\nu(x)U_\nu(x)\delta_{x+\hat{\nu},y} - \eta_\nu(y)U_\nu^\dagger(y)\delta_{x,y+\hat{\nu}}), \qquad (2.30)$$

in the background of the $U(1)$ gauge configurations of the $CP(N-1)$ model. First we consider the spectral density. Figure **2.12(a)** shows that as the coupling β is increased, also here a gap appears in the spectrum. At the same time the Polyakov loop becomes polarized near 1, as the coupling is increased. (Even though there is no *center symmetry* here, the Polyakov loop still shows a transition toward an ordered phase.) Thus there is a chance that the statistics of the spectrum may be different near the gap.

In Figure **2.13** the participation ratio $PR(\lambda)$ is shown as a function of λ. All across the spectrum $PR(\lambda) \sim 1/V$, which indicates that the eigenmodes are localized. Similarly, Figure **2.14** shows the level spacing distribution $P(s)$ and the distribution of the ratio of consecutive level spacings $P(\tilde{r})$ in different spectral windows. Also here the distributions are nearly Poissonian, in accord with the finding from the participation ratio that the eigenmodes are localized throughout the spectrum.

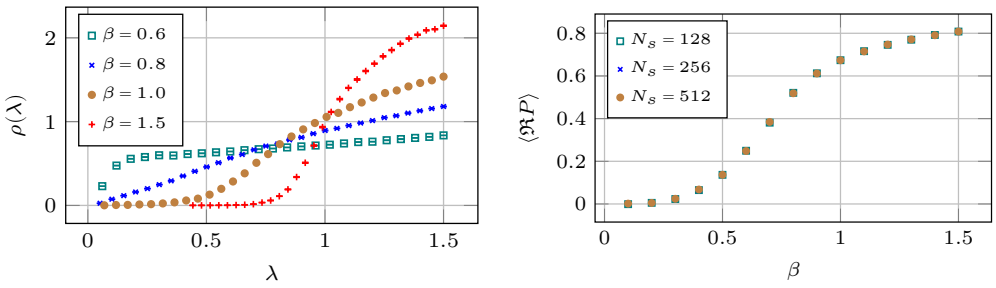

(a) (b)

Figure 2.12 (a): The spectral density of the $2D$ $CP(3)$ model for different β. As β is increased, a gap develops at the low end of the spectrum. (b): The Polyakov loop of the $2D$ $CP(3)$ model as a function of β. As the coupling is increased, the Polyakov loop becomes polarized towards 1.

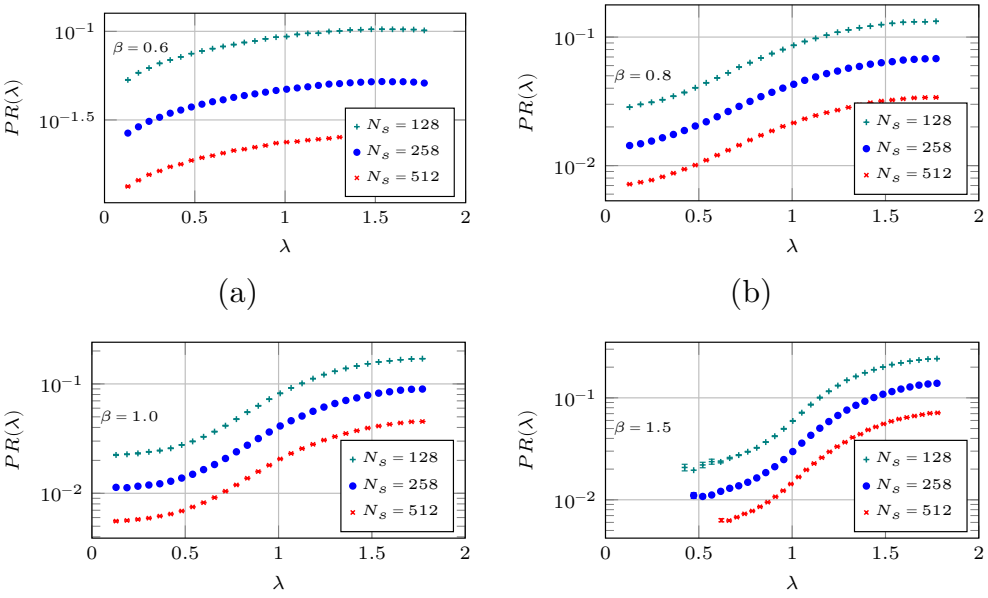

(a) (b)

(c) (d)

Figure 2.13 The participation ratio of the $2D$ $CP(3)$ model for different volumes and β. The PR scales as $1/V$ across the spectrum and in a wide range of β, indicating localization throughout the spectrum.

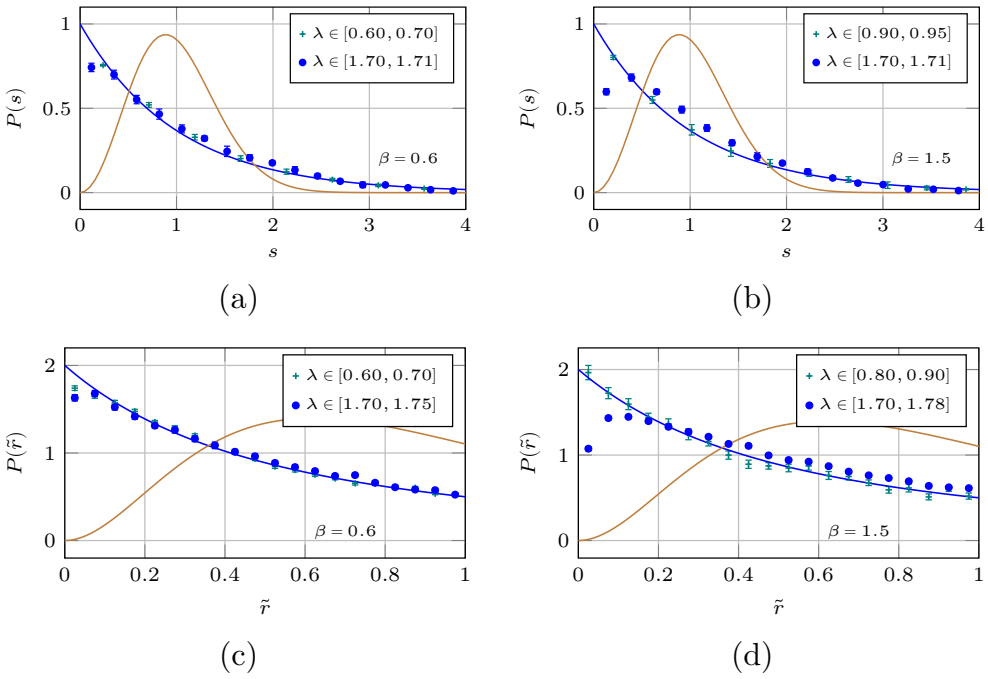

Figure 2.14 (a,b): The level spacing distribution $P(s)$ of the $2D$ $CP(3)$ model in different spectral windows and for different β. Also the curves for the GUE and the Poissonian distribution are shown. (c,d): The distribution of the ratio of level spacings $P(\tilde{r}) = 2P(r)\Theta(1-r)$ of the $2D$ $CP(3)$ model in different spectral windows and for different β. Also the curves for the GUE and the Poissonian distribution are shown. All the distributions are nearly Poissonian, again indicating localized modes.

2.4.4 Localization in 3D

In this section we consider $CP(N-1)$ in three dimensions, in order to see whether the dimensionality of the model plays a role in this case.

The participation ratio is shown in Figure **2.15**. At the low end of the spectrum the participation ratio scales with the volume, $PR(\lambda) \sim 1/V$, while higher up in the spectrum, no scaling takes place. This shows that only the low eigenmodes are localized, while the higher modes are delocalized. Also the level spacing distributions in Figures **2.16(a,b)** and the distributions of consecutive level spacings in Figures **2.16(c,d)** show a similar picture: At the low end of the spectrum the distributions are close to Poissonian, while for higher eigenvalues the distributions behave like the Gaussian unitary ensemble.

In order to characterize the transition from Poissonian to Gaussian level spacing distributions one can study in principle an arbitrary number of moments. Here we focus on the integral $I_{0.5}$ and the variance $\langle s^2 \rangle$ of the level spacing distribution. Figure **2.17(a)** shows $I_{0.5}(\lambda)$ for different β. The mobility edge can be determined from the inflection point of the curves. As the coupling β is increased the mobility edge moves to higher eigenvalues. Figure **2.17(b)** shows how $I_{0.5}$ and $\langle s^2 \rangle$ change in different eigenvalue windows. The data points for different β seem to follow a universal curve from a Poissonian to a Gaussian distribution. This transition can be modeled using deformed unitary random matrices[48]. From the current data it looks as if the transition follows the same curve as the QCD data, cf. Figure 7 in [48]. (The statistical errors are of the order of 10%. However, the spread of the mean values suggests a smaller error.) Toward the Poissonian point in this figure there are hardly any data points. This is mainly due to the fact that the spectrum is sparse at the gap; hence more statistics and/or a larger volume is needed in order to sample the Poissonian region better.

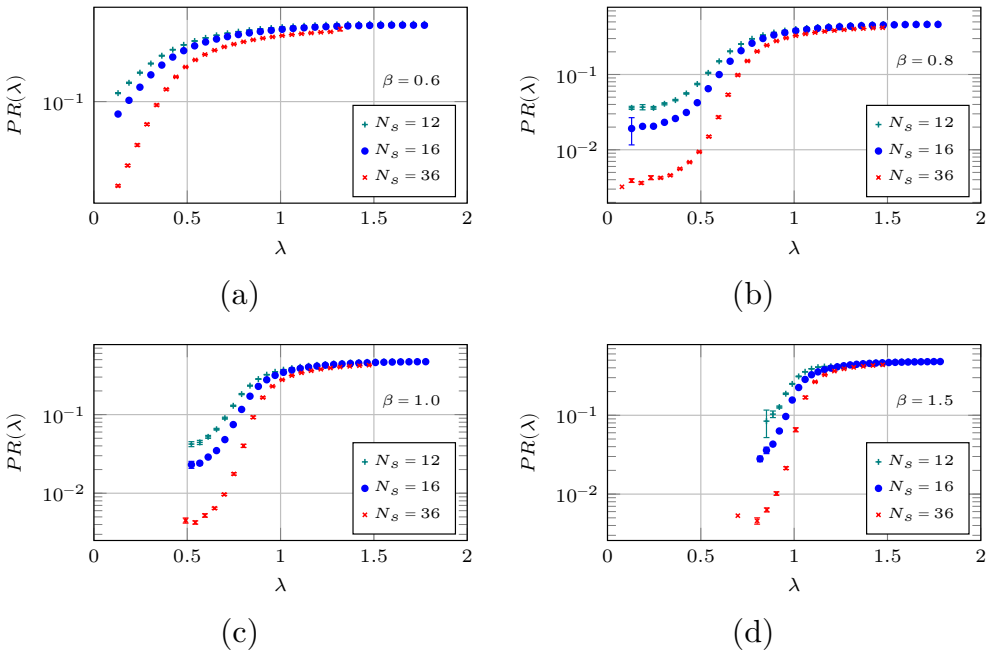

Figure 2.15 The participation ratio for different volumes and β. Here the PR scales as $1/V$ only at the low end of the spectrum, the higher modes show no scaling at all. This shows that only the low modes are localized.

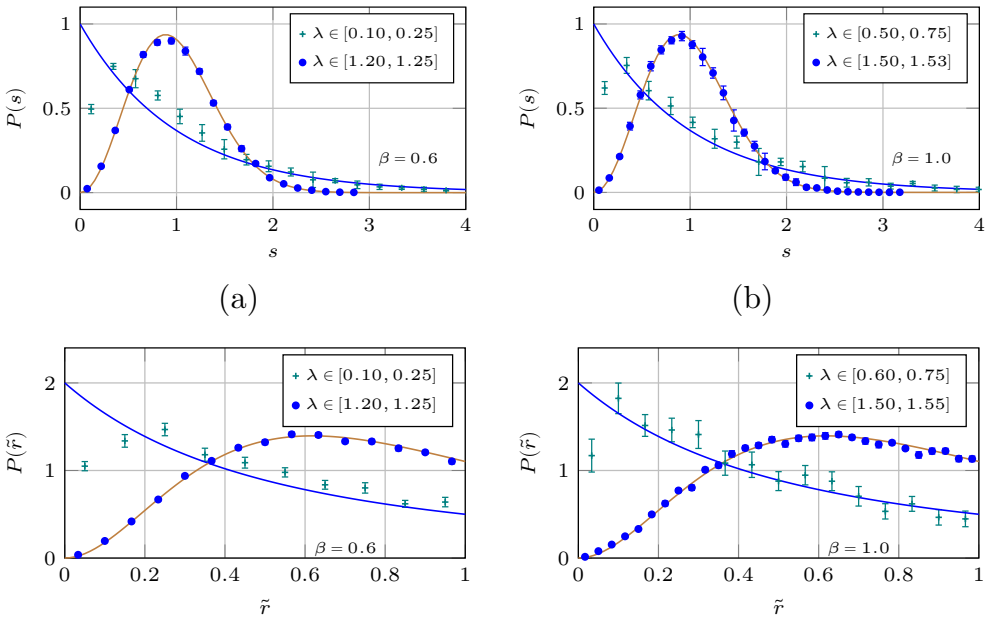

Figure 2.16 (a,b): The level spacing distribution $P(s)$ in different spectral windows and for different β. (c,d): The distribution of the ratio of level spacings $P(\tilde{r})$ in different spectral windows and for different β. In spectral windows that lie at the low end of the spectrum the distributions are Poissonian, while higher up in the spectrum the distributions behave like the GUE.

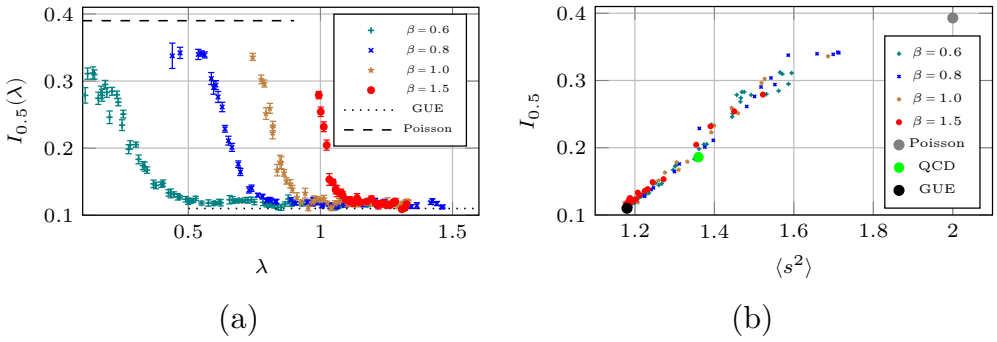

Figure 2.17 (a) The integral $I_{0.5}$ characterizing the transition from Poissonian to GUE statistics for the $3D$ $CP(3)$ model. (b) Characterizing the transition from Poissonian to GUE statistics for the $3D$ $CP(3)$ model using the integral $I_{0.5}$ vs. the variance of the level spacing distribution. For reference also the point of critical statistics in QCD is indicated, as obtained in [48]. The spread of the data points in this scatter plot can be taken as reference for the error estimation.

2.4.5 Discussion

The preceding sections have shown that in two dimensions the whole Dirac spectrum of $CP(N-1)$ models appears to be localized. The influence of the dimensionality of the system on the localization properties has been known for a long time. The original Anderson model had on-site/diagonal disorder; there it has been shown that in $d \leq 2$ for arbitrary small disorder localization occurs[72]. For off-site/off-diagonal disorder it depends on the details of the model, that is, the eigenmodes can fall into the three categories of localized, delocalized, and critical eigenmodes.

In three dimensions an Anderson transition in the spectrum takes place. Namely, the low end of the spectrum is localized, while the higher modes are delocalized. In between, a mobility edge can be defined. As the (lattice) coupling is increased, also the mobility edge moves up in the spectrum. Also in $CP(N-1)$ as the coupling is increased, the Polyakov loop becomes polarized to 1. Thus also here a similar trapping mechanism as in QCD may be at play, even though one cannot view the Polyakov loop as an order parameter in $CP(N-1)$, since there is no center symmetry.

2.5 Summary

In this chapter we have studied Anderson localization in different models/theories. QCD shows an Anderson transition in the deconfined phase. The main effect of a background magnetic field is to lower the mobility edge. A simple three dimensional toy model captures general features of the Anderson transition observed in QCD. The magnetic field in the toy model has a similar effect on the spectrum as in QCD. Nevertheless, due to the simplicity of the model not all features can be captured. So for instance, in the toy model the magnetic field essentially induces a simple shift in the spectrum, as opposed to QCD, where the effect of the magnetic field on the spectrum is more intricate.

In $CP(N-1)$ the localization properties depend on the dimensionality of the model: In two space-time dimensions all the modes are localized, while in three space-time dimensions an Anderson transition can be observed. In the three dimensional case the transition appears to be quite similar to QCD: Also here, as the lattice coupling is increased, a gap in the spectrum emerges and the lowest modes become localized.

All in all, Anderson-type transitions seem to be a rather common feature in lattice QFTs. Nevertheless, it is still not clear what physical role these Anderson transitions play. In QCD the following picture can be constructed: At low temperature all the Dirac eigenmodes are delocalized. In particular, this is true for the modes near the origin, which are essential for long ranging forces in bound states. The delocalized nature also works in favor of this; namely, delocalized modes necessarily have large spatial overlap with one another, which also entails more interaction between them. At high temperature on the other hand, there are no longer any modes near the origin, i.e., forces decay more quickly. Furthermore, the lowest modes become localized. This means that they have no spatial overlap, i.e., there is no interaction between them. As a result, the quarks no longer form bound states.

3 Landau Levels in QCD

The following chapter is based on the publication [73], which was done in collaboration with Falk Bruckmann, Gergely Endrődi, Matteo Giordano, Sandor Katz, Tamás Kovács, and Ferenc Pittler.

Studying QCD on the lattice with a background magnetic field has been a topic for many years now. In order for a magnetic field to have a significant impact on the phase structure of QCD, rather strong magnetic fields are required. For example a magnetic field that is comparable to a temperature of $T = 100\,\mathrm{MeV}$, which is still below the pseudo critical QCD transition temperature of $T_c \approx 160\,\mathrm{MeV}$, would be around $eB \approx 0.1\,\mathrm{GeV}^2$. Such a field strength is already several orders of magnitude above that of magnetars[74] ($eB \sim 10^{-5}\,\mathrm{GeV}^2$). Nevertheless, even higher magnetic fields may play an important role in understanding the evolution of the early universe as well as heavy ion collisions.

In the absence of strong interactions, the quarks only interact with the background magnetic field. This is a well-known problem, commonly denoted as the Landau problem. From a classical point of view, a constant magnetic field induces a helical motion of a charged particle around the direction of the magnetic field. The motion in the direction of the magnetic field is not hindered in any way. In a plane perpendicular to the magnetic field, the motion (projected to the plane) is restricted to circular orbits, whose radii shrink with rising magnetic field. This results in a dimensional reduction of the system, as the plane perpendicular to the magnetic field becomes essentially impervious. From a quantum mechanical point of view this picture remains essentially valid, only the radii become quantized. The orbits of different radii are called Landau levels. In particular, the lowest Landau level has zero radius. All the Landau levels are highly degenerate; the degeneracy of each Landau level is proportional to the total magnetic flux through the plane perpendicular to the magnetic field. Thus for a large enough magnetic field all occupied states are in the lowest Landau level eventually. This circumstance serves as the basis for the so called lowest Landau level approximation.

For interacting quantum field theories the situation becomes more complicated. If the interaction is weak, the Landau levels will simply be perturbed slightly, relieving some of the degeneracies, but leaving the overall Landau level structure intact. Especially at strong magnetic fields the lowest Landau level approximation is still expected to work

well. For strong interactions, in particular QCD, the situation is less clear and it has to be seen to what extent the Landau level structure can be carried over. In QCD the constituent fermionic particles, the quarks, carry electric charge and are thus susceptible to the magnetic field. The gluons on the other hand, which cause the strong interaction between the quarks, are electrically neutral and are thus only indirectly influenced by the magnetic field. Also here it may be expected that for exceedingly strong magnetic fields, the quarks will display Landau levels. However, for magnetic fields that are comparable with the QCD transition temperature this is far from obvious. Nevertheless, around the QCD transition this question becomes especially interesting, since there the system is highly susceptible to the behavior of the quarks.

In QCD the crossover from the confined low temperature phase to the high temperature phase of the quark gluon plasma goes hand in hand with the restoration of chiral symmetry. Below and above the crossover, the main effect of the magnetic field is to enhance chiral symmetry breaking, which goes under the name of magnetic catalysis. Only around the crossover inverse magnetic catalysis plays a dominant role[10]. The effect of magnetic catalysis can largely be attributed to the Landau level structure of quark spectra, as has been shown in various models of strong interactions[12–14]. For convenience, the lowest Landau level approximation is employed for a wide range of calculations involving strong interactions and large magnetic fields, e.g., see [75–82]. For asymptotically large fields this approximation is certainly applicable. Nevertheless, for moderately large fields it is quite hard to estimate the systematic errors that are introduced by the approximation. Also this may strongly depend on the observable in question, as there are observables which only take contributions from the lowest Landau level. Among these are anomalous currents[83,84] and spin polarizations[50,85].

Therefore the main motivation of this work was to quantify how good the lowest Landau level approximation actually is for a given setup. Lattice simulations give a first principles approach to this problem. The main advantage lies in the fact that other systematic effects due to, e.g., low energy approximations and effective models can be excluded. The following sections are organized as follows: First the Landau levels are introduced in two dimensions in Section **3.1**. Then Landau levels in four spacetime dimensions are discussed in Section **3.2**. Section **3.3** deals with observables in the lowest Landau level and shows numerical results thereof. Finally, Section **3.4** gives a general overview summarizing the findings.

3.1 Landau Levels in two dimensions

For simplicity let us start with the discussion of Landau levels in two dimensions. First we consider the free case, where the only interaction is between the quark and the magnetic field. We put the quark in the xy plane of size L^2 with periodic boundary conditions and the magnetic field along the z-axis. Setting

$$A_x = 0 \text{ and } A_y = xB \tag{3.1}$$

results in $\overrightarrow{B} = B\vec{e}_z = const.$. In a periodic space the total flux of the magnetic field is quantized, see [60],

$$qBL^2 = 2\pi N_b. \tag{3.2}$$

Here N_b is the flux quantum number. The Dirac operator reads

$$\not{D} = \gamma^x \partial_x + \gamma^y(\partial_y + iqxB), \tag{3.3}$$

where the charge, $q > 0$, of the quark is assumed to be positive[5]. The magnetic field couples to both the spin, $s_z = \pm 1/2$, as well as the angular momentum, $L_z = 2l + 1$, $l \in \mathbb{Z}_0^+$, of the quark. The resulting eigenvalues of $-\not{D}^2$ have the form

$$\lambda_n^2 = qB(2l + 1 - 2s_z) = 2nqB, \tag{3.4}$$

with degeneracy

$$\nu_n = N_b N_c(2 - \delta_{n,0}), \tag{3.5}$$

where the Landau index $n \in \mathbb{Z}_0^+$ is composed both of the spin and the angular momentum quantum number. The lowest Landau level has $l = 0$ and $s_z = 1/2$, resulting in a zero eigenvalue, $\lambda_0 = 0$, independent of the magnetic field. The lowest Landau level is polarized, that is, it has a definite spin projection; this is also reflected in the degeneracy in eq. (3.5), as it is only half of that of the higher Landau levels. The higher Landau Levels, $n > 0$, are comprised of both $s_z = \pm 1/2$ components, with the appropriate angular momentum quantum number l. In both cases the degeneracy of the Landau levels is proportional to the total flux of the magnetic field.

Next we consider a discretized version of the Dirac operator in eq. (3.3), namely the staggered Dirac operator

[5] A negative charge would result in the lowest Landau level having the opposite spin, $s_z = -1/2$.

$$D_{x,y} = \frac{1}{2}\sum_{\nu}(\eta_\nu(x)u_\nu(x)\delta_{x+\hat{\nu},y} - \eta_\nu(y)u_\nu^\dagger(y)\delta_{x,y+\hat{\nu}}), \tag{3.6}$$

$$u_1(x) = \exp(ia^2qBn_x), \qquad u_2(x) = \exp(-ia^2qBN_xn_y\delta_{n_x,N_x-1}), \tag{3.7}$$

where the $U(1)$ phases $u_\nu(x)$ implement the magnetic field on the lattice, as discussed in [9], and $\eta_\nu(x)$ are the staggered phases from eq. (1.16). The lattice sites are labeled by n_x and n_y, the lattice size is given by $N_xN_y = N_s^2$, with $L = aN_s$ and a the lattice spacing. The dependence of $u_\nu(x)$ on the magnetic field can be written in terms of the flux quantum N_b: $a^2qB = 2\pi N_b/N_s^2$. This sets an upper limit on the magnetic field through $N_b < N_s^2$ due to the periodicity of $u_\nu(x)$. Physically this bound can be understood as the highest mode that can be resolved on the lattice, which means $B < 2\pi/a^2$.

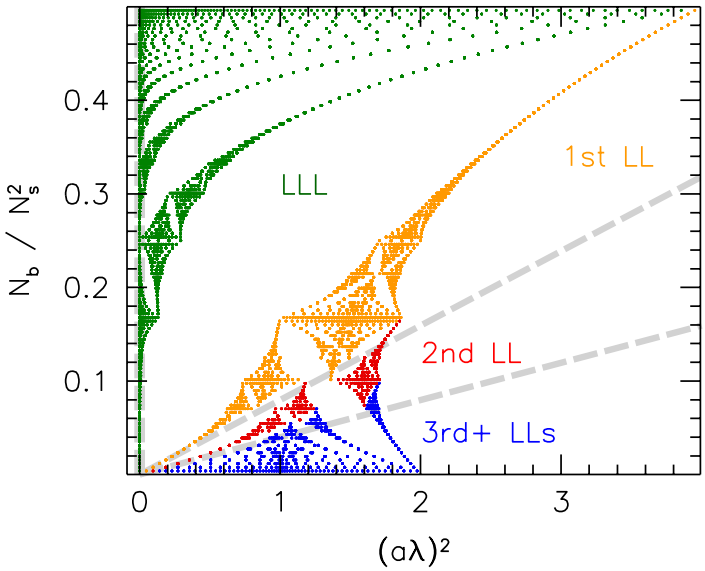

Figure 3.1 The eigenvalues of the staggered $2D$ Dirac operator (without QCD interactions) in eq. (3.6) vs. the magnetic field. The discretization breaks up the Landau levels into a fractal structure known as Hofstadter's butterfly. The color coding is according to the continuum degeneracy of the Landau levels as in eq. (3.5). Note the gap separating the lowest from the higher Landau levels. The continuum Landau levels are also indicated as dashed lines.

The eigenvalues of the staggered Dirac operator no longer have the simple form of eq. (3.4). Rather they break up and form a structure called

Hofstadter's butterfly[19]. Figure **3.1** displays the eigenvalues $(a\lambda)^2$ of the (negative) square of the staggered Dirac operator $-D^2$ as a function of the magnetic field. Even though the eigenvalues no longer obey eq. (3.4), the Landau level degeneracy in eq. (3.5) still groups together the eigenvalues in a sensible manner, as indicated by the color coding. The continuum limit takes place in the lower left corner of the plot, where $a\lambda \to 0$ and $N_b/N_s^2 \to 0$ (with B fixed). There the eigenvalues of the discretized operator lie virtually on top of the continuum curves for the Landau levels.

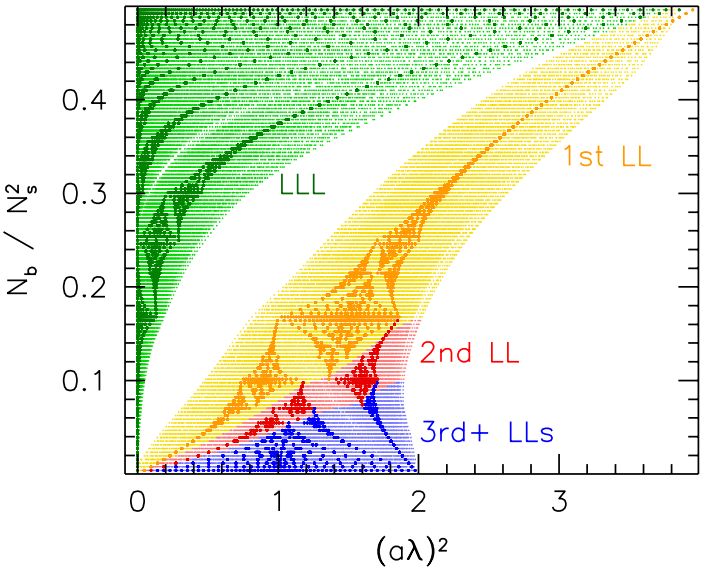

Figure 3.2 The eigenvalues of the interacting staggered $2D$ Dirac operator in eq. (3.8) vs. the magnetic field. The fractal structure of the butterfly is smeared out by the interaction. The lowest Landau level is still clearly separated by a gap in the spectrum from the rest. The higher Landau levels, however, start to mix and are no longer separated from one another. (For comparison, the free eigenvalues are still displayed. Also the color coding of the higher Landau levels is still according to the continuum degeneracy.)

Introducing QCD interactions is done in the usual way,

$$D_{x,y} = \frac{1}{2}\sum_{\nu}(\eta_\nu(x)u_\nu(x)U_\nu(x)\delta_{x+\hat{\nu},y} - \eta_\nu(y)U_\nu^\dagger(y)u_\nu^\dagger(y)\delta_{x,y+\hat{\nu}}), \quad (3.8)$$

using the $SU(3)$ gauge links $U_\nu(x) \in SU(3)$. Figure **3.2** shows that the interaction smears out the fractal structure of the butterfly[6]. This has the effect that the higher Landau levels mix and are thus no longer separated. However, the gap between the lowest and the higher Landau levels remains.

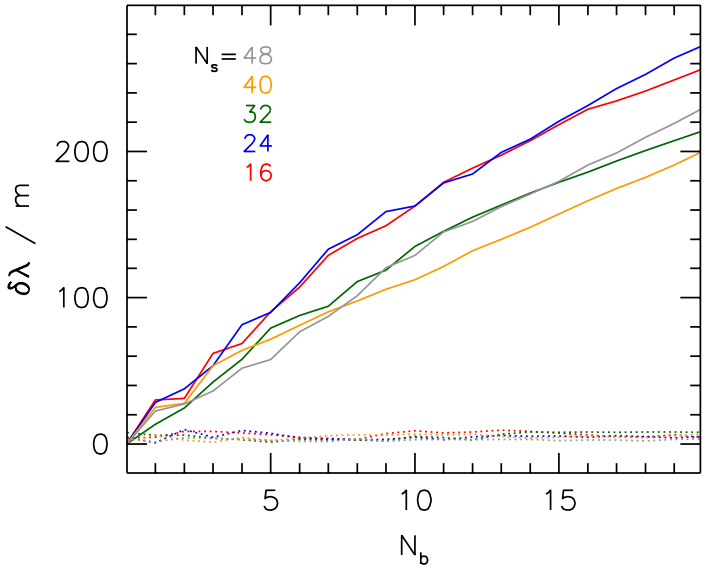

Figure 3.3 The dotted lines indicate the level spacing of the $2D$ Dirac operator right above the gap. The solid lines show the width of the gap between the lowest and the higher Landau levels. (Both quantities are measured in terms of the light quark mass, as this results in a renormalization group invariant spectral density, see [62].) The continuum limit ($N_s \to \infty$) shows that the gap is larger than the level spacing above it, even at small N_b. Thus the lowest Landau level is well separated even in the continuum with QCD interactions.

Figure **3.3** shows the width of the gap $\delta\lambda$ as a function of the magnetic flux N_b for different lattice spacings. The curves are for a fixed physical volume and the lattices have an aspect ratio $N_s/N_t = 4$; so the continuum limit corresponds to $N_s \to \infty$. It is evident that the width of the gap always exceeds the average level spacing above the gap for $N_b > 0$.

[6] The $SU(3)$ gauge links for the figure come from a $2d$ slice of a $4d$ gauge configuration at $T = 400\,\mathrm{MeV}$ with physical quark masses.

Thus the gap between the lowest and the higher Landau levels survives the continuum limit.

This finding is not accidental; namely, the lowest Landau level is protected by topology: In two dimensions the topological charge,

$$Q_{\text{top}}^{2D} = \frac{1}{2\pi} \int d^2x \, F_{xy} = \frac{1}{2\pi} L^2 qB = N_b, \tag{3.9}$$

is just the magnetic flux quantum number N_b. The four dimensional notion of handedness is replaced by the spin projection. In that way, the index theorem ensures that the topological charge,

$$Q_{\text{top}}^{2D} = N_\uparrow - N_\downarrow, \tag{3.10}$$

is equal to the difference between spin up and spin down zero modes. Moreover, in two dimensions the vanishing theorem[86–88] makes sure that either $N_\uparrow$ or $N_\downarrow$ is zero. For positive $qB > 0$, the only states with definite spin have spin up and thus $N_\uparrow = N_b$. The states belonging to the lowest Landau level, indeed, vanish and their degeneracy is just N_b for each color component separately.

Figure **3.4** shows a plot of the squared matrix elements $|\varphi_i^\dagger \sigma_{xy} \varphi_j|^2$ of the spin operator $\sigma_{xy} = \sigma_z$ for different eigenmodes φ_i, φ_j. (Details of how the spin operator is implemented on the lattice in the staggered formulation can be found in [50].) Only the (diagonal) matrix elements corresponding to the lowest Landau level are significantly different from zero. The matrix elements corresponding to higher Landau levels as well as off diagonal matrix elements are all compatible with zero. This shows that, even in the interacting case, the lowest Landau level is the only one with a definite spin.

3.2 Landau levels in four dimensions

In four dimension the situation becomes more involved. Again we will first look at the free case, where the quark solely interacts with the background magnetic field: Now there are additionally the z- and t-directions. Since the magnetic field acts only in the xy plane via the vector potential in eq. (3.1), the z- and t-components of the Dirac equation decouple from those in the xy plane. The solutions in the z- and t-directions are just plane waves, while the solutions in the xy plane are the Landau levels as before in the two dimensional case. Together the eigenmodes can be written

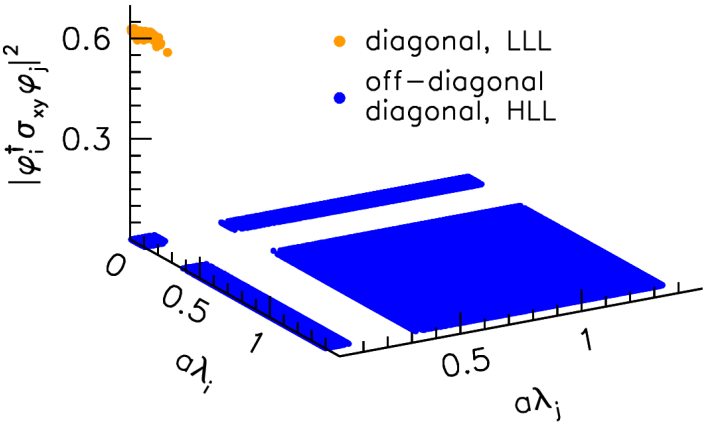

Figure 3.4 The squared matrix elements $|\varphi_i^\dagger \sigma_{xy} \varphi_j|^2$ of the spin operator $\sigma_{xy} = \sigma_z$ for different eigenmodes φ_i, φ_j. The off diagonal matrix elements are close to zero ($< 10^{-4}$). For higher Landau levels, the diagonal matrix elements are also close to zero ($< 10^{-2}$). Only for the modes from the lowest Landau level the matrix elements are significantly different from zero. (The eigenmodes and eigenvalues are indexed by their mode number i in this figure. For this figure a magnetic flux quantum $N_b = 10$ was chosen. The eigenmodes correspond to those of the down quark.)

$$\psi_{n\alpha p_z p_t} = \varphi_{n\alpha} e^{ip_z z} e^{ip_t t}, \tag{3.11}$$

where α labels the degeneracy within each Landau level. The eigenvalues[7] of $-\not{D}^2$ now have additional momenta p_z and p_t:

$$\lambda^2_{np_zp_t} = 2nqB + p_z^2 + p_t^2, \qquad \nu_{np_zp_t} = 2N_bN_c(2 - \delta_{n,0}). \tag{3.12}$$

Now each Landau level, n, can have arbitrary contributions from the p_z and p_t momenta, so different Landau levels necessarily overlap. Thus it is no longer possible to distinguish the lowest Landau level from the rest just by looking at the eigenvalues $\lambda_{np_zp_t}$.

[7] The additional factor of 2 for the degeneracy comes from the fact that in $4D$ we have to use 4-spinors instead of 2-spinors in $2D$.

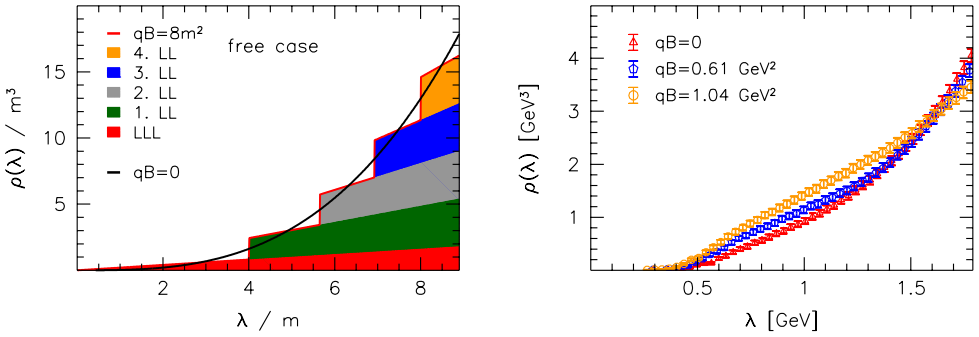

(a) (b)

Figure 3.5 (a): The spectral density of the free Dirac operator (only interacting with the magnetic field). The spectral density has distinct jumps at $\lambda = \sqrt{2nqB}$. It is no longer possible to distinguish different Landau levels by their eigenvalue alone. (b): In the interacting case the steps are smoothed out.

Figure **3.5(a)** shows the spectral density,

$$\rho(\lambda) = \int \frac{d^2p}{(2\pi)^2} \sum_n \nu_n \delta(\lambda - \lambda_{np_zp_t}) = \sum_n \nu_n \frac{\lambda}{2\pi} \Theta(\lambda^2 - 2nqB), \quad (3.13)$$

as a function of the eigenvalue. Higher Landau levels clearly start to contribute at the onsets $\lambda = \sqrt{2nqB}$ to the spectral density. In the interacting case, shown in Figure **3.5(b)**, this signature of the Landau levels is smoothed out.

Since it is no longer possible to distinguish the lowest Landau level by simple mode counting, we will use a projection operator that projects arbitrary modes down to the lowest Landau level. In the free case in the continuum it is obvious that

$$\begin{aligned} \text{continuum, non-int.: } P &= \sum_{p_z p_t} \sum_{\alpha} \psi_{0\alpha p_z p_t} \psi^{\dagger}_{0\alpha p_z p_t} \\ &= \sum_{\alpha} \varphi_{0\alpha} \varphi^{\dagger}_{0\alpha} \otimes \mathbb{1}_z \otimes \mathbb{1}_t \end{aligned} \quad (3.14)$$

projects down to the lowest Landau level. On the lattice it is still true that the eigenmodes factorize as in eq. (3.11), however, later it will be more convenient to use a coordinate basis for the z- and t-directions. In that case the eigenmodes can be written as

$$\psi_{izt}(x, y, z', t') = \varphi_i(x, y) \delta_{z,z'} \delta_{t,t'}, \quad (3.15)$$

where i labels the two dimensional Landau levels (with the eigenvalues in ascending order). The lowest Landau level corresponds to the first $2N_cN_b$ two dimensional eigenmodes φ_i. Thus the projector on the lattice reads (the sum over the doublers is an artifact of the staggered discretization)

$$\begin{aligned} \text{lattice, non-int.: } P &= \sum_{i\leq 2N_cN_b} \sum_{\text{doublers}} \sum_{zt} \psi_{izt}\psi^\dagger_{izt} \\ &= \sum_{i\leq 2N_cN_b} \sum_{\text{doublers}} \varphi_i\varphi_i^\dagger \otimes \mathbb{1}_z \otimes \mathbb{1}_t. \end{aligned} \tag{3.16}$$

In the interacting case, that is, when QCD interactions are switched on, the eigenmodes no longer factorize, as the xy and zt components of the Dirac operator $\not{D} = \not{D}_{xy} + \not{D}_{zt}$ do not commute in general. Still, we can use the eigenmodes $\varphi_i^{(zt)}$ of $D_{xy}^{(zt)}$ on a zt slice to span the space

$$\psi_{izt}(x,y,z',t') = \varphi_i^{(zt)}(x,y)\delta_{zz'}\delta_{tt'}.$$

Just as in the noninteracting case the projector can be written

$$\text{lattice, int.: } P = \sum_{i\leq 2N_cN_b} \sum_{\text{doublers}} \sum_{zt} \psi_{izt}\psi^\dagger_{izt}, \tag{3.17}$$

only it cannot be simplified any further than that. A similar construction can be made from $\tilde{\varphi}_i^{(zt)}$, which are eigenvalues of $\not{D}_{xy}^{(zt)}(B=0)$, the two dimensional Dirac operator at zero magnetic field. Similarly a basis is formed by the modes

$$\tilde{\psi}_{izt}(x,y,z',t') = \tilde{\varphi}_i^{(zt)}(x,y)\delta_{zz'}\delta_{tt'},$$

yielding the projector

$$\tilde{P} = \sum_{i\leq 2N_cN_b} \sum_{\text{doublers}} \sum_{zt} \tilde{\psi}_{izt}\tilde{\psi}^\dagger_{izt}. \tag{3.18}$$

The projector $\tilde{P}$ can be used to cancel additive divergencies, as will be shown later.

To see that the construction of P, as a lowest Landau level projector, in eq (3.17) is justified, we can define the quantity

$$W_i(\phi) = \sum_{zt} \sum_{\text{doublers}} |\psi^\dagger_{izt}\phi|^2.$$

Here ϕ is an arbitrary eigenmode of the full Dirac operator $\not{D}(B)$. Thus $W_i(\phi)$ measures the overlap of ϕ with the i-th two dimensional Landau mode. The fact that ψ_{izt} form a complete basis, as well as, the normalization, $\phi^\dagger\phi = 1$, ensures that the overlap factors W_i are also properly normalized: $\sum_i W_i(\phi) = 1$.

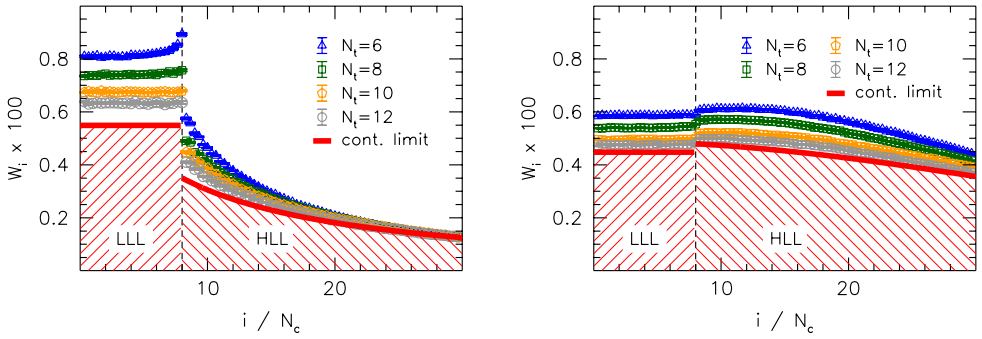

(a) $220 < \lambda/m_{ud} < 225$ (b) $535 < \lambda/m_{ud} < 545$

Figure 3.6 The overlap factor $W_i(\phi)$ as a function of the Landau eigenmode number i. $W_i(\phi)$ is averaged over several modes ϕ lying in a small spectral window as well as over several gauge configurations. Low lying modes show a stronger overlap with modes from the lowest Landau level. (The magnetic flux quantum is $N_b = 8$, the temperature is $T = 400\,\mathrm{MeV}$, and m_{ud} is the light quark mass. Thus the degeneracy of the lowest Landau level is $N_c N_b = 24$.)

Figure **3.6(a)** shows that low lying eigenmodes, indeed, have a stronger overlap with the lowest Landau level than higher modes that lie in the bulk of the spectrum, as depicted in Figure **3.6(b)**. Moreover, there is a distinct jump in the overlap factor between the lowest and higher Landau levels. Also the overlap factor is approximately constant for the lowest Landau level, signaling that these modes are equivalent in that respect. (In the case of vanishing magnetic field $B = 0$, the overlap factor becomes a smoothly decreasing function.) This shows that P can, indeed, be used to analyze the effects of the lowest Landau level in full QCD.

It is not clear, a priori, that the action corresponding to this restricted Dirac operator is local. This is an important point, since the universality of the continuum limit rests on this fact. In the continuum the lowest Landau level has a natural length scale $l_B = \sqrt{qB}$ associated with it. Thus it is sufficient to show that the projector P is local down to that same length scale.

From the definition of P in eq. (3.17) it is clear that it is already perfectly local in the z- and t-directions. (This is to be expected, since a magnetic field in the z-direction, $\vec{B} = B\vec{e}_z$, affects only the transverse motion in the xy plane.) We can analyze the effect of P in the xy plane by acting with P on a source vector ξ, localized at a lattice site (x, y, z, t):

$$\Psi = P\xi. \tag{3.19}$$

We can measure the effect of P by analyzing the decay of Ψ in the xy plane. In particular, we can measure the decay of

$$L(d) = \langle \|\Psi(x', y', z, t)\| \rangle, \qquad d = \sqrt{(x - x')^2 + (y' - y)^2}, \tag{3.20}$$

where the expectation value $\langle ... \rangle$ involves an average over different z-t-slices as well as different gauge configurations.

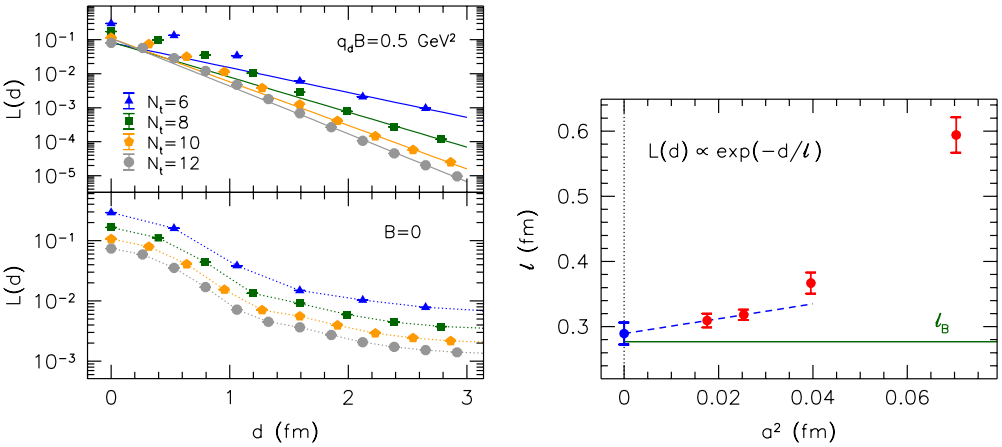

(a) decay of $L(d)$ (b) continuum limit

Figure 3.7 (a): $L(d)$ as a function of the distance d for $B = 0.5\,\mathrm{GeV}^2$ and $B = 0$. For $B \neq 0$ $L(d)$ decays exponentially, while for $B = 0$ no such decay is observed. (b): The continuum extrapolation shows that the characteristic length l is compatible with that of the lowest Landau level $l_B = \sqrt{qB}$.

Figure **3.7(a)** shows that $L(d) \sim e^{-d/l}$ has an exponential decay for $B > 0$, with a characteristic decay length l. In the continuum limit the characteristic length l is compatible with that of the lowest Landau level l_b, as is shown in Figure **3.7(b)**. The fact that P appears to be a local operator is highly nontrivial. This has to be due to an intricate interplay of the modes in the lowest Landau level. Generally speaking, the projection down to a subset of the spectrum is a highly

nonlocal object, which is confirmed by the slow decay of $L(d)$ due to the projection operator $\tilde{P}$, as depicted in Figure **3.7(a)** (lower panel). (Remember that $\tilde{P}$ is built up from the first $2N_cN_b$ two dimensional modes at $B = 0$, cf. eq. (3.18). N_b is set to the would be value for $B > 0$, of course.)

3.3 Observables for the lowest Landau level

Now we can use the projector P in eq. (3.17) to define lowest Landau level projected observables. This enables us to assess to what extend the observable in question is dominated by the lowest Landau level. In principle any observable that can be expressed in terms of quark eigenvalues or eigenmodes is suitable for this. In the following we will focus on quark bilinears $\langle\bar{\psi}^f\Gamma\psi^f\rangle$ for a particular quark flavor f.

The QCD partition function $\mathcal{Z}$ for three flavors, up, down, and strange, reads

$$\mathcal{Z} = \int \mathcal{D}U\mathcal{D}\bar{\psi}\mathcal{D}\psi\, e^{-S_G - S_M}, \tag{3.21}$$

$$S_M = \bar{\psi}M\psi = \sum_f \bar{\psi}^f M_f \psi^f, \tag{3.22}$$

where $M = \mathrm{diag}(M_u, M_d, M_s)$ is the fermion matrix and S_G is the action for the $SU(3)$ gauge fields U. The quark matrix for the flavor f is given by $M_f = \not{D}_f - m_f$. The explicit flavor dependence of the Dirac operator comes from the fact that the different flavors couple to the background magnetic field via different electric charges: $q_u = -2q_d = -2q_s = 2e/3$, where $e > 0$ is the positive elementary charge. The quark bilinears can be written

$$\begin{aligned}\langle\bar{\psi}^f\Gamma\psi^f\rangle &= \frac{T}{4V}\frac{1}{\mathcal{Z}}\int \mathcal{D}U\mathcal{D}\bar{\psi}\mathcal{D}\psi\,(\bar{\psi}^f\Gamma\psi^f)e^{-S_G-S_M} \\ &= \frac{T}{4V}\frac{1}{\mathcal{Z}}\int \mathcal{D}U e^{-S_G}(\det M)^{1/4}\,\mathrm{Tr}(M_f^{-1}\Gamma),\end{aligned} \tag{3.23}$$

where in the last step the quark fields have been integrated out analytically and the rooting trick for staggered fermions has been applied, in order to have only the above mentioned three flavors in the continuum limit. The prefactor T/V makes the observable intensive. Details of the lattice setup involving the scale setting as well as the setting of the quark masses $m_u = m_d$ and m_s are described in [9,58].

In order to obtain the contribution of the lowest Landau level to these bilinears, the projector P from eq. (3.17) can be used. The projector can be represented in block diagonal form in flavor space, $P = \mathrm{diag}(P_u, P_d, P_s)$, just as the fermion matrix. For the observable the quark matrix is simply replaced by $M \to PMP$. For the weight the higher Landau levels should be quenched, $M \to PMP + 1 - P$, otherwise the determinant would vanish altogether. Thus the lowest Landau level contribution of the quark bilinears is given by

$$\langle \bar{\psi}^f \Gamma \psi^f \rangle^{LLL} = \tag{3.24}$$
$$= \frac{T}{4V} \frac{1}{\mathcal{Z}} \int \mathcal{D}U e^{-S_G} (\det(PMP + 1 - P))^{1/4} \,\mathrm{Tr}(M_f^{-1} P_f \Gamma P_f).$$

It is possible to study the valence and sea effects separately, that is, one can either leave out the projector from the weight (using just $\det M$ as the weight) or one can leave out the projector from the observable (using just $\mathrm{Tr}(M_f^{-1}\Gamma)$ as the observable). Furthermore, it is possible to consider the weight $\det M$ with or without the B-dependence. At present, only the valence case with zero magnetic field in the weight has been studied. (The other cases are more complicated to implement and computationally more expensive.) This means that only the quarks in the valence sector feel the presence of the magnetic field, while the sea quarks, governing the distribution of the gauge configurations, are not affected by the magnetic field at all. For temperatures below and above the QCD transition temperature, $T_c \approx 160\,\mathrm{MeV}$, the valence contribution is the dominant one[49], e.g., for the quark condensate. Only around the transition temperature the sea effect takes the lead, see [10]. In the following, we will use the quark bilinears in the valence approximation:

$$\langle \bar{\psi}^f \Gamma \psi^f \rangle = \tag{3.25}$$
$$= \frac{T}{4V} \frac{1}{\mathcal{Z}(0)} \int \mathcal{D}U e^{-S_G} [\det M(0)]^{1/4} \,\mathrm{Tr}[M_f^{-1}(B)\Gamma],$$
$$\langle \bar{\psi}^f \Gamma \psi^f \rangle^{LLL} = \tag{3.26}$$
$$= \frac{T}{4V} \frac{1}{\mathcal{Z}(0)} \int \mathcal{D}U e^{-S_G} [\det M(0)]^{1/4} \,\mathrm{Tr}[M_f^{-1}(B) P_f \Gamma P_f].$$

In particular, we will focus on the quark condensate, $\langle \bar{\psi}\psi \rangle$ (i.e., $\Gamma = 1$), and the spin polarization, $\langle \bar{\psi}\sigma_{xy}\psi \rangle$ (i.e., $\Gamma = \sigma_{xy}$); the staggered

implementation of $\sigma_{xy} = \frac{i}{2}[\gamma_x, \gamma_y]$, containing also the gauge fields in the xy plane, can be found in [50].

3.3.1 Renormalization

Observables like quark bilinears are UV-divergent quantities, which means that comparing the lowest Landau level contribution to the full quantity has to be done with care. Let us start by considering these for the free case in the continuum first. For this we assume a large but finite volume, $V = L^3$, and $qB > 0$ for simplicity. Also the temperature is assumed to be $T = 0$; since the lowest Landau level approximation is expected to work best when the magnetic field is the largest scale in the system, relaxing this condition to $0 < T < \sqrt{B}$ is not expected to make much of a difference. To simplify the notation further we will neglect a factor of $N_c = 3$ because all three color components give the same contribution in the free case.

3.3.1.1 Additive divergencies in the free case

The condensate can be written as

$$\langle\bar{\psi}\psi\rangle_B = \frac{T}{V}\mathrm{Tr}(\not{D} + m)^{-1} = \sum\!\!\!\!\!\!\int_{\lambda} \frac{1}{i\lambda + m} = \sum\!\!\!\!\!\!\int_{\lambda>0} \frac{2m}{\lambda^2 + m^2}, \qquad (3.27)$$

$$\text{with} \quad \sum\!\!\!\!\!\!\int_{\lambda>0} = T\sum_{p_t}\sum_{n}\int \frac{dp_z}{2\pi}\frac{\nu_n}{L^2},$$

for the third equality the fact that there are chiral partners with opposite eigenvalue has been used. The eigenvalues λ and degeneracies ν_n are those of the Landau levels in eq. (3.12). At $T = 0$ the discrete sum over Matsubara frequencies turns into an integral over p_t, similar to p_z. Thus for any fixed Landau level, n, the integration over p_z and p_t is UV-divergent.

We can rewrite the condensate by exponentiating the denominator, that is, by using $1/y = \int_0^\infty ds\, e^{-sy}$, which is essentially Schwinger's proper time[89] formulation. Thus it becomes possible to sum up all the Landau levels and integrate over the p_z and p_t momenta analytically:

$$\langle\bar{\psi}\psi\rangle_B = \frac{mqB}{2\pi^2}\int_0^\infty ds\, e^{-m^2 s}\sum_n (2-\delta_{n0})e^{-2qBns}\int_0^\infty dp\, pe^{-p^2 s}$$
$$= \frac{mqB}{4\pi^2}\int_0^\infty ds\,\frac{e^{-m^2 s}}{s}\coth(qBs). \tag{3.28}$$

In this formulation, the divergence comes from the lower boundary of the s integration. Using the cutoff scale Λ and expanding the coth for small s, we can identify the divergence,

$$\langle\bar{\psi}\psi\rangle_B = \frac{mqB}{4\pi^2}\int_{1/\Lambda^2}^\infty ds\, e^{-m^2 s}\left[\frac{1}{qBs^2}+\frac{qB}{3}+\mathcal{O}(s^2)\right]$$
$$= \frac{m\Lambda^2}{4\pi^2}-\frac{m^3}{4\pi^2}\log\frac{\Lambda^2}{m^2}+\text{finite}. \tag{3.29}$$

The divergence does not depend on the magnetic field B at all; thus it can be removed by subtracting the condensate at $B=0$. In this way $\Delta\langle\bar{\psi}\psi\rangle$ is a finite quantity,

$$\Delta\langle\bar{\psi}\psi\rangle_B = \langle\bar{\psi}\psi\rangle_B - \langle\bar{\psi}\psi\rangle_0 = \frac{mqB}{4\pi^2}\int_0^\infty ds\,\frac{e^{-m^2 s/qB}}{s^2}(s\coth(qBs)-1)$$
$$= \frac{mqB}{2\pi^2}\left[\log\Gamma(x)-\left(x-\frac{1}{2}\right)\log x + x - \frac{1}{2}\log(2\pi)\right], \tag{3.30}$$

with $x = m^2/(2qB)$.

For the lowest Landau level contribution to the condensate we can simply take the $n=0$ part of the sum in eq. (3.28) above, which is tantamount to replacing $\coth(qBs)$ by 1:

$$\langle\bar{\psi}\psi\rangle_B^{LLL} = \frac{mqB}{4\pi^2}\int_0^\infty ds\,\frac{e^{-m^2 s}}{s}. \tag{3.31}$$

In this case the divergence is milder; namely, it is only logarithmic,

$$\langle\bar{\psi}\psi\rangle_B^{LLL} = \frac{mqB}{4\pi^2}\log\frac{\Lambda^2}{m^2}+\text{finite}. \tag{3.32}$$

Here the divergence cannot be removed by subtracting the $B=0$ contribution as the divergence does depend on the magnetic field. However,

the divergence can be removed by subtracting $\langle\bar{\psi}\tilde{P}\psi\rangle$, using the projector $\tilde{P}$ in eq. (3.18). $\tilde{P}$ projects on the first N_b two-dimensional ($B = 0$) modes, i.e., onto the modes that would be in lowest Landau level at $B > 0$. In that way the quantity $\Delta\langle\bar{\psi}\psi\rangle_B^{LLL}$ stays finite:

$$\begin{aligned}\Delta\langle\bar{\psi}\psi\rangle_B^{LLL} &= \langle\bar{\psi}\psi\rangle_B^{LLL} - \langle\bar{\psi}\tilde{P}\psi\rangle_0 \\ &= \frac{m}{\pi}\int_0^\infty \frac{dp\,p}{2\pi}\left[\frac{qB}{p^2+m^2} - 2\int_0^{\sqrt{qB}}\frac{dp_{xy}\,p_{xy}}{2\pi}\frac{2m}{p^2+p_{xy}^2+m^2}\right] \\ &= \frac{mqB}{4\pi^2}\left[(1+2x)\log\left(1+\frac{1}{2x}\right) - 1\right], \end{aligned} \tag{3.33}$$

with $x = m^2/(2qB)$ again. The upper bound $\sqrt{qB}$ ensures that only the first N_b two-dimensional modes participate. This can be derived by counting free fermionic states in a box of size L_xL_y:

$$2\frac{L_xL_y}{(2\pi)^2}\int_{p_x^2+p_y^2\le qB} dp_x dp_y = 2\frac{L_xL_y}{2\pi}\int_0^{\sqrt{qB}} dp\,p = \frac{L_xL_y}{2\pi}qB = N_b. \tag{3.34}$$

An alternative way of regularization is the gradient flow method[90,91], which involves smearing the fields with the help of the heat kernel

$$K_t = e^{-t(-D^2+m^2)},$$

where D^2 is the (gauge-covariant) Laplacian, m the quark mass, and t the flow time. The flow time can be related to the smearing radius[90] R_s via $t = R_s^2/8$. In the condensate both quark fields $\bar{\psi}$ and ψ are flowed, resulting in

$$\langle\bar{\psi}\psi\rangle_B(t) = \frac{T}{V}\mathrm{Tr}[(\not{D}+m)^{-1}K_{2t}].$$

In the free case the Laplacian D^2 commutes with the squared Dirac operator $\not{D}^2$. Also the eigenvalues of D^2 are essentially the same as those of $\not{D}^2$, only with the spin set to zero, $s_z = 0$, and degeneracy ν_l:

$$\lambda_{lp_zp_t} = qB(2l+1) + p_z^2 + p_t^2, \qquad \nu_l = N_b. \tag{3.35}$$

Just as before we can use the chiral partners to obtain a spectral representation for the condensate, cf. eq. (3.27):

$$\langle\bar{\psi}\psi\rangle_B(t) = \frac{mqB}{2\pi^2}e^{-2tm^2}\sum_{l=0}^{\infty}\sum_{s_z=\pm\frac{1}{2}}\int_0^{\infty}dp\,p\frac{e^{-2t[qB(2l+1)+p^2]}}{qB(2l+1-2s_z)+p^2+m^2}.$$

Also here we can use Schwinger's proper time, as well as, sum over Landau levels and integrate over the momenta, yielding

$$\langle\bar{\psi}\psi\rangle_B(t) = \frac{mqB}{4\pi^2}e^{-2tm^2}\int_0^{\infty}ds\,\frac{e^{-sm^2}\cosh(qBs)}{(2t+s)\sinh(qB(2t+s))}. \quad (3.36)$$

For any flow time $t > 0$ the integral no longer diverges, with $1/t = \Lambda^2$ being essentially the momentum cutoff scale. Again, the lowest Landau level approximation can be obtained by taking only the $l = 0$ and $s_z = +1/2$ contribution to the sum:

$$\langle\bar{\psi}\psi\rangle_B^{LLL}(t) = \frac{mqB}{4\pi^2}e^{-2tm^2}e^{-2tqB}\int_0^{\infty}ds\,\frac{e^{-sm^2}}{(2t+s)}. \quad (3.37)$$

The lowest Landau level approximation is expected to be valid (if at all) when the magnetic field is the largest scale in the system. Consequently, the flow time can be chosen in terms of the magnetic field; namely, choosing $8t = c^2/(qB) = R_s^2$ with $c \approx 1$ has a well defined continuum limit for fixed B because the physical smearing radius R_s then also stays fixed.

The other observable left to consider is the spin polarization $\langle\bar{\psi}\sigma_{xy}\psi\rangle$. A spectral representation can be obtained in a similar fashion as for the condensate in eq. (3.27):

$$\langle\bar{\psi}\sigma_{xy}\psi\rangle_B = \sum_{\lambda>0}\!\!\!\!\!\!\int\frac{2m}{\lambda^2+m^2}\langle\lambda|\sigma_{xy}|\lambda\rangle = \langle\bar{\psi}\sigma_{xy}\psi\rangle_B^{LLL} = \langle\bar{\psi}\psi\rangle_B^{LLL}, \quad (3.38)$$

where the fact has been used that only the lowest Landau level has a definite spin projection, i.e., $\langle\lambda^{LLL}|\sigma_{xy}|\lambda^{LLL}\rangle = 1$ while all higher Landau levels are composed of both spin-up and spin-down states. Thus in the free case there is no distinction between the lowest Landau level contribution and the full observable in this case. Both are equal to the lowest Landau level condensate in eq. (3.31) and hence logarithmically divergent. The divergence is proportional to $m\log\Lambda^2/m^2$; therefore a possible way to extract the finite part is

$$T^{div} \equiv m\frac{\partial}{\partial m}\langle\bar{\psi}\sigma_{xy}\psi\rangle_B, \tag{3.39}$$

$$\Delta\langle\bar{\psi}\sigma_{xy}\psi\rangle_B = \langle\bar{\psi}\sigma_{xy}\psi\rangle_B - T^{div} = \frac{mqB}{2\pi^2}. \tag{3.40}$$

This procedure also works in the interacting case, where T^{div} has been measured in Ref. [50] for full QCD.

3.3.1.2 Analyzing the ratios of the observables

In the last section we have seen that additive UV-divergencies can be eliminated in two different ways. One is by subtracting the observable at $B = 0$, the other is by smearing the gauge as well as the fermion fields over an area R_s^2 with the help of the gradient flow, which eliminates short scale (UV) noise.

The multiplicative renormalization constants on the other hand are expected to be independent of the magnetic field. Also in the limit of exceedingly large magnetic fields, $B \to \infty$, the lowest Landau level approximation should be valid. In that case it seems natural that the lowest Landau level projected observables should have the same renormalization constants as the full observable. However, since the lowest Landau level projection on the lattice effectively involves the limit $B \to \infty$ *before* the continuum limit, $a \to 0$, it is still conceivable that the ultra violet behavior might be affected. Whether this is the case or not has to be checked in a future study.

In the following we will consider the ratio of observables, first in the free case and afterwards numerically at a fixed cutoff. Let us start with the condensate and the $B = 0$ subtraction scheme and define the ratio

$$D_f^S(B) = \frac{\Delta\langle\bar{\psi}_f\psi_f\rangle^{LLL}}{\Delta\langle\bar{\psi}_f\psi_f\rangle}, \tag{3.41}$$

$$\Delta\langle\bar{\psi}_f\psi_f\rangle_B^{LLL} = \langle\bar{\psi}_f P\psi_f\rangle_B - \langle\bar{\psi}_f\tilde{P}\psi_f\rangle_0, \tag{3.42}$$

$$\Delta\langle\bar{\psi}_f\psi_f\rangle_B = \langle\bar{\psi}_f\psi_f\rangle_B - \langle\bar{\psi}_f\psi_f\rangle_0, \tag{3.43}$$

where we have used the lowest Landau level projector P from eq. (3.17) as well as the projector at vanishing magnetic field $\tilde{P}$ from eq. (3.18). In the free case the numerator and denominator were given in the previous section in eq. (3.33) and (3.30), respectively. Taking the ratio and also the limit $B \to \infty$ yields

$$D^S(B) \xrightarrow{B\to\infty} 1 - \mathcal{O}\left(\frac{1}{\log(qB/m^2)}\right). \tag{3.44}$$

So the ratio only very gradually approaches 1 from below.
Secondly we consider the same type of ratio only now with the flowed observables rather than the subtracted ones:

$$C_f^S(B,t) = \frac{\langle\bar{\psi}_f\psi_f\rangle_B^{LLL}(t)}{\langle\bar{\psi}_f\psi_f\rangle_B(t)}. \tag{3.45}$$

The flow time can be set by the magnetic field via $t = c^2/(8qB)$ where $c \approx 1$ is just a fixed parameter. In the free case this ratio can be written

$$C^S(B,t) = \frac{I_2(t)}{I_1(B,t)}, \tag{3.46}$$

$$I_1(B,t) = \int_0^\infty ds\, \frac{e^{-sm^2}}{2t+s}\frac{1+e^{-2qBs}}{1-e^{-2qB(2t+s)}}, \tag{3.47}$$

$$I_2(t) = \int_0^\infty ds\, \frac{e^{-sm^2}}{2t+s}. \tag{3.48}$$

For large magnetic fields, $B \to \infty$, I_2 has the asymptotic form:

$$I_2 \xrightarrow{B\to\infty} \log(qB/2cm^2)$$

The difference $I_1 - I_2$ is bounded, which can be seen from

$$\begin{aligned} I_1 - I_2 &= \int_0^\infty ds\, \frac{e^{-sm^2}e^{-2sqB}}{2t+s}\frac{1+e^{-4qBt}}{1-e^{-4qBt}e^{-2qBs}} \\ &\leq \frac{1+e^{-4qBt}}{1-e^{-4qBt}}\int_0^\infty ds\, \frac{e^{-sm^2}e^{-2sqB}}{2t+s} \\ &= \frac{1+e^{-4qBt}}{1-e^{-4qBt}}\int_0^\infty ds\, \frac{e^{-sm^2/qB}e^{-2s}}{2qBt+s} \\ &\leq \frac{1}{4qBt}\frac{1+e^{-4qBt}}{1-e^{-4qBt}}. \end{aligned} \tag{3.49}$$

Since $qBt \sim c$ is kept fixed by the parameter $c \approx 1$, the difference is bounded from above independently from the magnetic field. Consequently we can write

$$\frac{1}{C^S} = 1 + \frac{I_1 - I_2}{I_2} \xrightarrow{B\to\infty} 1 + \mathcal{O}\left(\frac{1}{\log(qB/m^2)}\right)$$

$$\text{and conversely} \quad C^S \xrightarrow{B\to\infty} 1 - \mathcal{O}\left(\frac{1}{\log(qB/m^2)}\right). \tag{3.50}$$

Strictly speaking, the above analysis is only valid at zero temperature. However, it turns out that the asymptotic behavior at $B \to \infty$ remains valid even at nonzero temperature. Intuitively this is clear, since then the magnetic field B is the largest scale in the system which cannot be spoiled by any finite temperature T.

3.3.2 Results

Figures **3.8(a,c)** show the ratio $D_d^S(B)$ for the down[8] quark as a function of the magnetic field for two different temperatures, $T = 124\,\text{MeV}$ and $T = 170\,\text{MeV}$, which are below and above the QCD crossover temperature, respectively. Shown are curves for different lattice spacings towards the continuum limit, $a \to 0$, at a fixed temperature $T = 1/(N_t a)$; that is, a larger value of N_t is closer to the continuum. The total physical volume is kept fixed with an aspect ratio of $N_s/N_t = 4$. In both cases D_d^S rises from about 30% at $eB \approx 0.4\,\text{GeV}^2$ to 50 %−80% at $eB \approx 1.6\,\text{GeV}^2$. Also the curves for the finer lattices lie closer together, which implies that a continuum limit may be possible for this observable.

Figures **3.8(b,d)** show the ratio $C_d^S(B)$ as a function of the magnetic field, again for the two temperatures $T = 124\,\text{MeV}$ and $T = 170\,\text{MeV}$. Here the ratio $C_d^S(B)$ rises from about 20% at $eB \approx 0.4\,\text{GeV}^2$ to about 50% at $eB \approx 1.6\,\text{GeV}^2$. However, in this case the curves even for the finest lattice spacings still differ significantly, that is, there seems to be no scaling towards the continuum limit for this observable. (This may change for finer lattices.)

Provided we take the $N_t = 10$ and $N_t = 12$ curves to assess the validity of the lowest Landau level approximation, we find that both C_d^S and D_d^S

[8] Since the lowest Landau level projector only acts in the valence sector, the results for the up quark are the same only at a different value of the magnetic field, i.e., $\langle\bar{\psi}_u\Gamma\psi_u\rangle_B = \langle\bar{\psi}_d\Gamma\psi_d\rangle_{2B}$, where also the parity symmetry $B \to -B$ has been used.

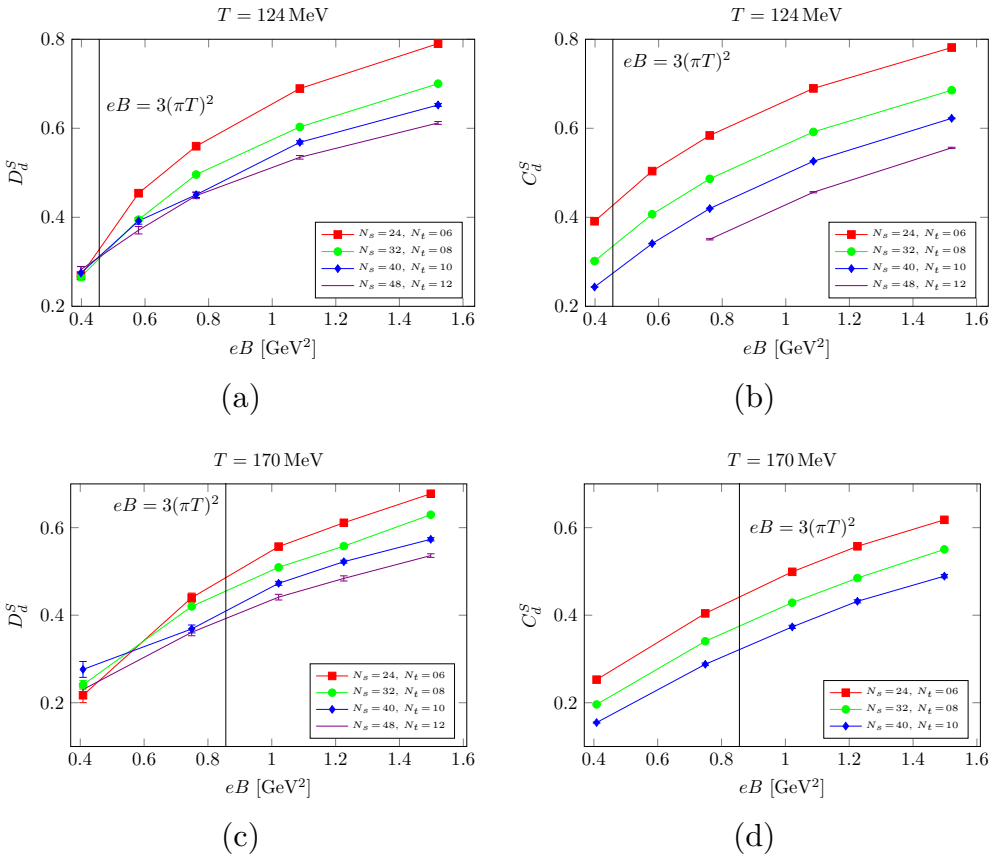

Figure 3.8 The ratios D^S and C^S both for the down quark as a function of the magnetic field for different lattice spacings. For comparison also the line $eB = 3(\pi T)^2$ where the magnetic field becomes the largest dimensionful scale in the system is included.

are at most 50%-60% at our largest magnetic field $eB \approx 1.6\,\mathrm{GeV}^2$. This is well in accordance with the findings for the free case above: Both C^S and D^S only very gradually approach 1, where the deviation from 1 is of the form $1/\log(B)$, cf. eq. (3.44) and (3.50).

For the spin polarization we can define similar ratios. Since the spin polarization $\langle\bar{\psi}\sigma_{xy}\psi\rangle$ vanishes at $B = 0$, the subtraction scheme to extract the finite part has to be defined differently, see eq. (3.40) above.

$$D_f^T(B) = \frac{\langle\bar{\psi}\sigma_{xy}\psi\rangle_B^{LLL} - T^{div}}{\langle\bar{\psi}\sigma_{xy}\psi\rangle_B - T^{div}},$$

with T^{div} from eq. (3.39) from above.

In the free case only the lowest Landau level contributes to the spin polarization, $\langle\bar{\psi}\sigma_{xy}\psi\rangle_B^{LLL} = \langle\bar{\psi}\sigma_{xy}\psi\rangle_B$, and consequently the ratio is trivially $D^T \equiv 1$ in this case.
In the case of the flowed observables, the ratio can simply be written as

$$C_f^T(B) = \frac{\langle\bar{\psi}\sigma_{xy}\psi\rangle_B^{LLL}(t)}{\langle\bar{\psi}\sigma_{xy}\psi\rangle_B(t)},$$

where the flow time is set by $t = c^2/(8qB)$ with $c \approx 1$. In the free case this ratio is also trivially equal to unity.

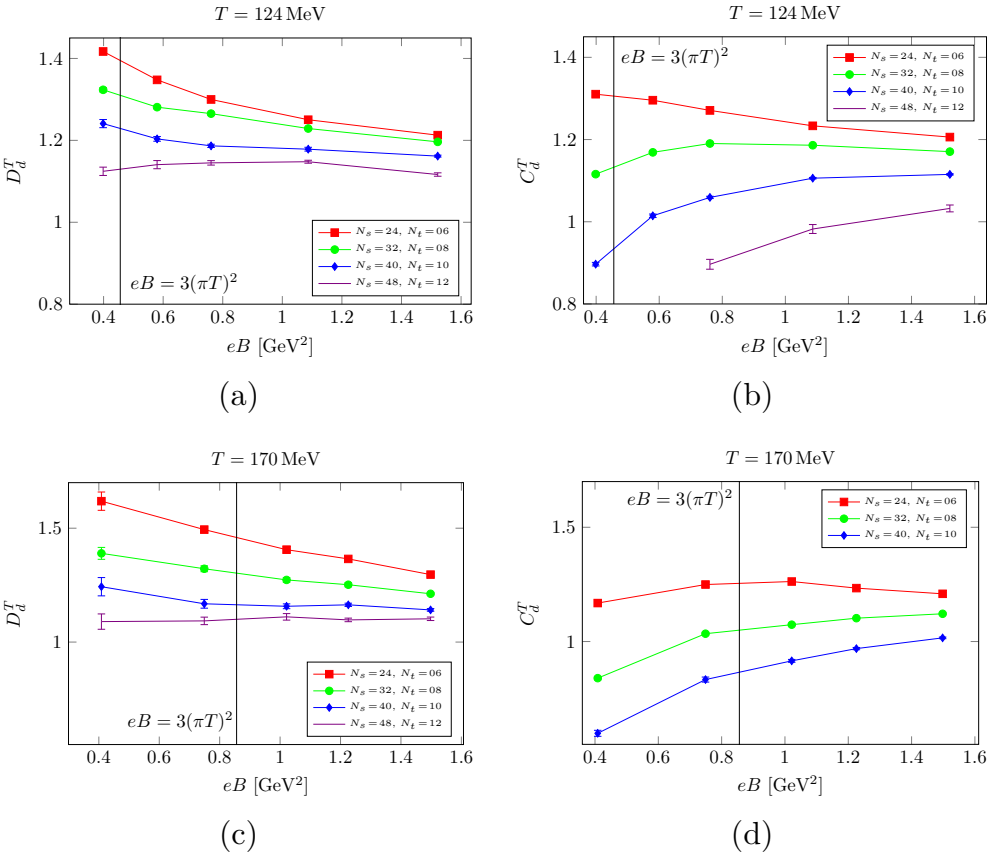

Figure 3.9 The ratios D_d^T and C_d^T for the down quark as a function of the magnetic field for different lattice spacings. For comparison the line $eB = 3(\pi T)^2$ where the magnetic field becomes the largest dimensionful scale in the system is included.

In Figures **3.9(a,c)** the ratio D_d^T is shown as a function of the magnetic field, again for the same two temperatures as above. The curves for different lattice spacings reveal that D_d^T scales nicely towards the continuum

limit. All the curves show $D_d^T > 1$, namely that the spin polarization is *overestimated* by the lowest Landau level approximation. This may be understood as follows: For the lowest Landau level the eigenvalues of σ_{xy} are close to 1, see Figure **3.4**. The higher Landau levels must have negative matrix elements, in order for σ_{xy} to be a traceless operator. This also entails negative contributions from higher Landau levels to the spin polarization $\langle\bar{\psi}\sigma_{xy}\psi\rangle$. Nevertheless, the deviation of D_d^T from 1 is much milder than that of the condensate D_d^S above. It remains below 15% for the finest lattice spacing ($N_t = 12$). This is in good agreement with the expectation from the free case where the ratio is trivially equal to unity.

For the ratio C_d^T the situation is not so clear, as can be seen in Figures **3.9(b,d)**. Here the different lattice spacings show large cutoff effects, e.g., sometimes C_d^T approaches 1 from above, and sometimes from below.

3.4 Summarizing the results

In the last sections the Landau level structure of QCD in a background magnetic field has been analyzed. In the free case, i.e., when no QCD interactions are present, the spectrum of the Dirac operator can be conveniently grouped into Landau levels. The degeneracies of the Landau levels are all proportional to the magnetic flux. The lowest Landau level's eigenvalues are independent of B, while the higher Landau levels have squared eigenvalues proportional to B. Therefore with a rising magnetic field the higher Landau levels become ever more suppressed, while the lowest Landau level approximation becomes better and better.

In the case of full QCD, i.e., when color interactions are present, the situation becomes much more involved because the color interactions mix different Landau levels. Consequently it is no longer possible to easily distinguish between different Landau levels. Nevertheless, it has been shown that even in that case the lowest Landau level can be extracted in a consistent manner. That this is at all possible has topological reasons. Namely, it rests on the fact that the two-dimensional lowest Landau level modes have zero-eigenvalues and the number of these modes is a topological invariant, which depends solely on the magnetic flux but not on the gluonic field configuration. On the lattice these zero-modes are shifted to nonzero values, however, there is still a gap in the spectrum between these modes and the rest. This gap corresponds to the largest gap in Hofstadter's butterfly in solid state physics, which also there

separates the lowest Landau level from the higher ones. Thus in two dimensions the lowest Landau level can be identified unambiguously even in the interacting case.

In four dimensions this is no longer true. Nevertheless, for each xy plane (perpendicular to $\vec{B}$) the lowest Landau level can be clearly identified. In this way a projector P can be constructed that projects a four-dimensional mode precisely onto the lowest Landau level subspace in each xy plane. In this way it was found that low lying four dimensional modes, indeed, have a larger overlap with the lowest Landau level than higher four-dimensional modes have.

With the help of the projector P the lowest Landau level contribution to a number of common fermionic observables could be defined. The focus was mainly on the quark condensate $\bar{\psi}P\psi$ and the spin polarization $\bar{\psi}P\sigma_{xy}P\psi$. The ratios of the lowest Landau level approximated observable to the full observable give an estimation of the validity of the lowest Landau level approximation. In particular, the ratios are constructed in such a way as to become unity in the limit $B \to \infty$.

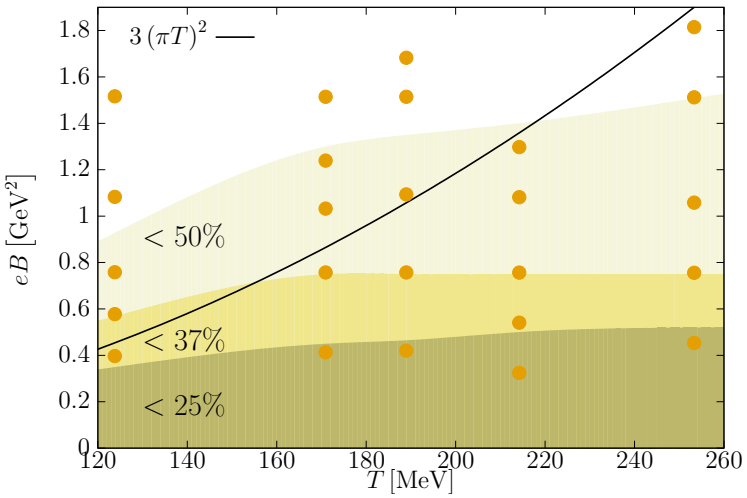

Figure 3.10 The ratio D_d^S showing the validity of the condensate in the T-B plane. The lighter the color, the closer the lowest Landau level approximation is to the full result. The orange dots indicate the simulation points and black line, $q_d B = (\pi T)^2$, marks when the magnetic field becomes the largest dimensionful scale in the system.

For the quark condensate the lowest Landau level approximation is found to generally underestimate the full condensate. For the spin polarization the opposite is true, namely, the spin polarization is *overestimated* by

the lowest Landau level approximation. Still, in both cases the full observable is slowly approached by the lowest Landau level approximated one with rising magnetic field.

Finally, Figure **3.10** shows the results for D_d^S (at $N_t = 12$) in the $T - B$ plane for a wide range of temperatures and magnetic fields. Darker regions indicate where the approximation becomes worse and worse, that is, where the approximation is only 50%, 37%, and 25% of the full result, respectively. White areas on the other hand indicate that there the lowest Landau level approximation makes up more that 50% of the full result. The contours have been found using splines of $D_d^S(B)$ to calculate the magnetic field at which D_d^S reaches a given percentage. Using these threshold values at the different temperatures a second spline, this time in T, was employed to give the contours shown in the figure. These results can also be compared with the naive expectation that the lowest Landau level approximation becomes valid when the magnetic field becomes the largest scale in the system, i.e., when $qB > (\pi T)^2$.

All in all, the above analysis shows that the validity of the lowest Landau level approximation can be assessed quantitatively using first principle methods, i.e., lattice simulations. One has to stress that the findings above are only for the valence part. A lowest Landau level projection for the virtual sea quarks is left for future studies.

4 Addressing the sign problem with dual variables

Lattice gauge theory, and lattice QCD in particular, has been immensely successful in computing physical quantities from first principles. Among these were decay constants as well as hadronic masses, see e.g., [92, 93]. Moreover, also the thermodynamic properties can be studied quite naturally. Nevertheless, problems arise as soon as one considers non-zero density, that is, an abundance of particles over anti particles or vice versa. In that case we face difficulties when applying the usual Monte-Carlo methods with importance sampling due to the occurrence of a sign problem: In the Euclidean path integral representation of the partition function,

$$\mathcal{Z} = \int \mathcal{D}\Phi \, e^{-S[\Phi]},$$

each configuration of the fields Φ is weighted with the negative exponent of the action $S[\Phi]$. As long as the action is real, e^{-S} can be viewed as a probability distribution. However, when the action is complex this is no longer the case and we are confronted with a sign problem.

Over the years there have been numerous proposals of how to overcome the sign problem. These include *reweighting*, *stochastic quantization*, *dual variables*, and *Lefschetz-thimbles*. Reweighting works by adding the imaginary part of the action to the observable, while using the real part of the action as the weight of the probability distribution. Thus the expectation value of an observable X can be computed as

$$\langle X \rangle_{\text{complex}} = \frac{\langle X e^{-i\Im(S)} \rangle_{\text{real}}}{\langle e^{-i\Im(S)} \rangle_{\text{real}}}, \tag{4.1}$$

where $\langle ... \rangle_{\text{complex}}$ denotes the expectation value with respect to the complex action and $\langle ... \rangle_{\text{real}}$ denotes the expectation value with respect to only the real part of the action. Even though this is an exact rewriting with no approximations, in practice there is the problem that the imaginary part of the action may be highly oscillatory. Thus evaluating eq. (4.1) numerically is tricky because delicate cancellations have to appear. Hence this method only works when the so called reweighting factor $r = \langle e^{-i\Im(S)} \rangle_{\text{real}}$ is not too small. Physically this

means that the free energy difference between the system with $\Im(S) = 0$ and $\Im(S) \neq 0$ should be small.

Complex-Langevin is a form of stochastic quantization. It works by complexifying field space and then using the Langevin equation for the evolution of the fields. Under certain conditions it can be shown that the resulting field configurations at large evolution times are distributed according to the original action. The advantage of the Langevin-method is that a Markov-chain can be generated without importance sampling. While the (real) Langevin method works very well in many different contexts, see e.g., [94–96], the complexified version has serious problems, in that convergence to the right distribution is not guaranteed in all cases[97–99]. Moreover, it is not clear whether these problems are technical or principal in nature.

For the dual variable approach notice that even though the integrand in the partition function can be complex, the partition function itself has to be real for a stable physical system in equilibrium, i.e., for a partition function that can be represented as

$$\mathcal{Z} = \mathrm{Tr} e^{-\beta(\hat{H}-\mu\hat{N})}. \tag{4.2}$$

Thus all the imaginary contributions have to cancel. The partition function can be decomposed into a sum/integral over only positive terms in arbitrarily many different ways. The problem is to find such a useful representation for the partition function for a given (complex) action. One way to obtain such a decomposition is to analytically integrate out some or all of the fields appearing in the action at the expense of introducing new variables while doing so. It has then to be checked whether the resulting decomposition has the desired properties.

Finally, the Lefschetz-thimble method is in some sense similar to the Langevin approach. The idea is to write the partition function as a sum over different so called thimbles, on which the imaginary part of the action remains constant. This relies on the deformation of the integration contour for complex integrals. One such thimble can be defined as the union of all paths of steepest decent ending on a particular critical point of the action. Now, if only a few of the thimbles contribute to the partition function, the sign problem is solved, in the sense that one has only to sum up a few terms with different complex phases. Whether this is the case in realistic examples, e.g., QCD, remains to be seen.

In the following we will focus on dual variables. First, the situation in QCD is reviewed; afterwards, the particular example of QCD with scalar

quarks is presented. If not indicated otherwise, the chemical potential μ and the mass m are measured in lattice units.

4.1 QCD

The QCD partition function for one fermion flavor can be written as

$$\mathcal{Z}(\mu) = \int \mathcal{D}U\mathcal{D}\psi\mathcal{D}\bar{\psi}\, e^{-S_g - S_f(\mu)}, \tag{4.3}$$

with S_g the gauge action and the fermionic action using staggered fermions

$$\begin{aligned} S_f(\mu) = \sum_x \Big[\sum_\nu \Big(& \eta_\nu(x) e^{\mu\delta_{\hat{\nu},\hat{0}}} \bar{\psi}(x) U_\nu(x) \psi(x+\hat{\nu}) \\ & - \eta_\nu(x) e^{-\mu\delta_{\hat{\nu},\hat{0}}} \bar{\psi}(x+\hat{\nu}) U_\nu^\dagger(x) \psi(x) \Big) \\ & + 2m\bar{\psi}(x)\psi(x) \Big]. \end{aligned} \tag{4.4}$$

As long as $\mu = 0$ the first and the second terms in the sum are complex conjugates of each other, and thus the action yields a positive determinant when the Grassmann fields are integrated out. Similarly also for μ purely imaginary the action remains real. For real μ, however, the action becomes complex and we end up with a sign problem. The gauge action S_g does not couple to the chemical potential and thus remains real irrespective of μ.

Since the gauge action plays no role for the sign problem, it is often neglected when studying the sign problem. This is equivalent to the strong coupling limit, where the lattice coupling is set to $\beta = 0$. The first proposal of dual variables in $U(3)$ QCD was in [100]. This was then extended to the case of $SU(3)$ at finite baryon density by *Karsch & Mütter* in [101]. Later works contributed to these formulations by refining the algorithmic details and mapping out the phase diagram[102]. A similar construction works with center subsets, where instead of the whole $SU(3)$ integration only $\mathbb{Z}_3$ rotations are performed[103,104]. The resulting formulation does retain the $SU(3)$ gauge links, but contains the same building blocks[103], since the $SU(3)$ integration and the $\mathbb{Z}_3$ summation project onto the same terms.

In order to obtain the dual formulation, note that in the strong coupling limit the integration over the gauge field variables $U_\nu(x)$ factorizes. Also

the exponential at a single link can be factorized further. With the shorthand notation

$$\begin{aligned} u &= \eta_\nu(x)\bar{\psi}(x)U_\nu(x)\psi(x+\hat{\nu}), \\ \bar{u} &= -\eta_\nu(x)\bar{\psi}(x+\hat{\nu})U_\nu^\dagger(x)\psi(x), \end{aligned} \tag{4.5}$$

we can expand the kinetic term at a single link as

$$\begin{aligned} e^{ue^{\mu\delta_{\hat{\nu},\hat{0}}}}e^{\bar{u}e^{-\mu\delta_{\hat{\nu},\hat{0}}}} &= \sum_{m,n=0}^{3}\frac{1}{m!n!}(e^{\mu\delta_{\hat{\nu},\hat{0}}}u)^m(e^{-\mu\delta_{\hat{\nu},\hat{0}}}\bar{u})^n \\ &= 1 + u\bar{u} + \frac{1}{4}u^2\bar{u}^2 + \frac{1}{36}u^3\bar{u}^3 + \frac{1}{6}(e^{3\mu\delta_{\hat{\nu},\hat{0}}}u^3 + e^{-3\mu\delta_{\hat{\nu},\hat{0}}}\bar{u}^3) \\ &\quad + \text{terms vanishing under } SU(3) \text{ integration}, \end{aligned} \tag{4.6}$$

where it has been used that u and $\bar{u}$ are Grassmann bilinears and hence commuting. There are also a number of mixed terms that vanish when the $SU(3)$ integration is performed. For instance the term u vanishes due to $\int dU U = 0$, and similarly for the other mixed terms. Only the terms written explicitly do not vanish under the $SU(3)$ integration. In order to perform the integrals, we can make use of the $SU(3)$ integrals[23]

$$\int dU\, U_{ab}(U^\dagger)_{cd} = \frac{1}{3}\delta_{ad}\delta_{bc}, \tag{4.7}$$

$$\int dU\, U_{ab}U_{cd}U_{ef} = \frac{1}{6}\varepsilon_{ace}\varepsilon_{bdf}. \tag{4.8}$$

With the help of (4.7) the integral over the $u\bar{u}$-term gives

$$\int dU\, u\bar{u} = \frac{1}{3}\bar{\psi}(x)\psi(x)\bar{\psi}(x+\hat{\nu})\psi(x+\hat{\nu}). \tag{4.9}$$

The $u^2\bar{u}^2$-term is somewhat more complicated. Due to the Grassmann nature of the $\bar{\psi}$s we can substitute the color components $\bar{\psi}_a\bar{\psi}_c = \frac{1}{2}\varepsilon_{ace}\varepsilon_{ACe}\bar{\psi}_A\bar{\psi}_C$ and similarly for the ψs. Denoting with $\psi' = \psi(x+\hat{\nu})$, the u^2-term becomes

$$u^2 = \frac{1}{4}\bar{\psi}_A\psi'_B\bar{\psi}_C\psi'_D\varepsilon_{ace}\varepsilon_{ACe}\varepsilon_{bdf}\varepsilon_{BDf}U_{ab}U_{cd}.$$

The two Us can be contracted[105] with two of the εs, using $\varepsilon_{ace}\varepsilon_{bdf}U_{ab}U_{cd} = 2(U^\dagger)_{ef}$, which gives

$$u^2 = \frac{1}{2}\bar{\psi}_A \psi'_B \bar{\psi}_C \psi'_D \varepsilon_{ACe} (U^\dagger)_{ef} \varepsilon_{BDf}.$$

In the same way the $\bar{u}^2$-term can be reduced to

$$\bar{u}^2 = \frac{1}{2}\bar{\psi}'_A \psi_B \bar{\psi}'_C \psi_D \varepsilon_{ACe} U_{ef} \varepsilon_{BDf}.$$

Thus for the U integration we can again use eq. (4.7), giving

$$\int dU\, u^2 \bar{u}^2 = \frac{1}{3}((\bar{\psi}\psi)(x))^2((\bar{\psi}\psi)(x+\hat{\nu}))^2. \tag{4.10}$$

The remaining u^3- and $\bar{u}^3$-terms can also be simplified using the Grassmann nature of the ψs:

$$\begin{aligned} u^3 &= \eta_\nu(x)\bar{\psi}_a U_{ab} \psi'_b \bar{\psi}_c U_{cd} \psi'_d \bar{\psi}_e U_{ef} \psi'_f \\ &= -\eta_\nu(x)\bar{\psi}^3 \psi'^3 \varepsilon_{ace}\varepsilon_{bdf} U_{ab} U_{cd} U_{ef} \\ &= -6\eta_\nu(x)\bar{\psi}^3(x)\psi^3(x+\hat{\nu}), \end{aligned}$$

where it was used that $\varepsilon_{ace}\varepsilon_{bdf}U_{ab}U_{cd}U_{ef} = 6 \det U = 6$ and the shorthands $\psi^3 = \psi_1\psi_2\psi_3$ and $\bar{\psi}^3 = \bar{\psi}_1\bar{\psi}_2\bar{\psi}_3$ were introduced. In the same way $\bar{u}^3$ gives

$$\bar{u}^3 = 6\eta_\nu(x)\bar{\psi}^3(x+\hat{\nu})\psi^3(x).$$

Therefore the U integration becomes trivial for those terms, and we can write

$$\begin{aligned} \int dU\, e^{u e^{\mu\delta_{\nu,\hat{0}}}} e^{\bar{u} e^{-\mu\delta_{\nu,\hat{0}}}} &= 1 + \frac{1}{3}\bar{\psi}\psi(x)\bar{\psi}\psi(x+\hat{\nu}) + \frac{1}{12}\left(\bar{\psi}\psi(x)\bar{\psi}\psi(x+\hat{\nu})\right)^2 \\ &\quad + \frac{1}{36}\bar{\psi}^3\psi^3(x)\bar{\psi}^3\psi^3(x+\hat{\nu}) \\ &\quad - \eta_\nu(x)e^{3\mu\delta_{\nu,\hat{0}}}\bar{\psi}^3(x)\psi^3(x+\hat{\nu}) \\ &\quad + \eta_\nu(x)e^{-3\mu\delta_{\nu,\hat{0}}}\bar{\psi}^3(x+\hat{\nu})\psi^3(x). \end{aligned} \tag{4.11}$$

Similarly, also the mass term can be expanded at each site:

$$e^{2m\bar{\psi}\psi(x)} = 1 + 2m\bar{\psi}\psi(x) + \frac{(2m)^2}{2}(\bar{\psi}\psi(x))^2 + \frac{(2m)^3}{6}(\bar{\psi}\psi(x))^3. \tag{4.12}$$

The partition function is the product of all links as in eq. (4.11) together with all sites as in eq. (4.12), integrated over the Grassmann fields at all sites. The Grassmann integration introduces a number of constraints on which terms contribute to the partition function. Using the common definition for Grassmann integrals, $\int d\xi = 0$ and $\int d\xi\, \xi = 1$, one finds that at each site all the color components of ψ and $\bar{\psi}$ have to be present, in order to have a nonvanishing contribution.

The first two lines in eq. (4.11) add equal amounts of ψ and $\bar{\psi}$ on each of the two neighboring sites. Also the mass terms only add equal amounts of ψ and $\bar{\psi}$ to a site. The μ-dependent terms, on the other hand, only add ψ^3 on one site and $\bar{\psi}^3$ on a neighboring site, and vice versa. This means that all the color components on one site are already saturated for ψ, but not for the conjugate $\bar{\psi}$ on that same site. The only way to also saturate the color components of the conjugate field is by building up closed, nonintersecting loops. Since these are oriented and they depend on the chemical potential, they are referred to as *baryonic* loops. The other terms do not depend on μ and are thus called *mesonic*. Also they can form paths, in order to saturate the Grassmann fields on the sites, which do not necessarily have to be closed.

Provided that the Grassmann fields are saturated at every site, the Grassmann integration can be performed, yielding a *dual* configuration. The dual configuration consists of a set of three occupation numbers or dual variables:

$$n(x) \in \{0,1,2,3\}, \quad k_\nu(x) \in \{0,1,2,3\}, \quad b_\nu(x) \in \{-1,0,1\} \tag{4.13}$$

Here $n(x)$ stands for one of the mass terms in eq. (4.12). $k_\nu(x)$ is the mesonic occupation number, i.e., the first two lines of eq. (4.11). And finally, $b_\nu(x)$ is the baryonic occupation number, namely, the last two lines of eq. (4.11). The constraint for the baryonic variable is that $\sum_\nu b_\nu(x) = 0$[9], which essentially states flux conservation on each site, thus ensuring that only closed loops can exist. Furthermore, the $b_\nu(x)$ can only be nonzero if $k_\nu = n = 0$ on the sites x and $x + \hat{\nu}$. Hence the baryonic parts of space are completely disjoint from the rest. A value of $b_\nu(x) = -1$ is interpreted as an *antibaryon* hopping from x to $x + \hat{\nu}$, or equivalently a *baryon* hopping from $x + \hat{\nu}$ to x. In this sense a baryon leaving one site can always be interpreted as an antibaryon entering a neighboring site, and vice versa.

[9] The sums over ν are understood to go over all $2 \cdot d$ directions, i.e., all forward and backward hoppings.

The other two variables are subject to the constraint $\sum_\nu k_\nu(x)+n(x) = 3$. This means that the ks can either also form closed paths, or the paths have to end with mass terms n. The case $k_\nu = 3$ is somewhat special as it is also completely disjoint from all neighboring sites. Moreover, it can also be seen as a special kind of baryon loop, which after one forward hopping immediately closes by hopping backward again; thus being μ-independent.

The partition function can now be entirely written in terms of the dual variables k_ν, n, and baryonic loops ℓ formed by the b_νs[102]:

$$\mathcal{Z}(\mu) = \tag{4.14}$$
$$= \sum_{\{k,n,l\}} \left(\prod_{x,\nu} \frac{(3-k_\nu(x))!}{3!k_\nu(x)!} \right) \left(\prod_x \frac{3!}{n(x)!} (2m)^{n(x)} \right) \left(\prod_\ell W_\ell(\mu)) \right),$$

where the weight of a baryonic loop is given by

$$W_\ell(\mu) = \frac{e^{3\mu N_t w_t}}{(3!)^{N_\ell}} (-1)^{N_- + w_t + 1} \prod_{(x,\nu)\in\ell} \eta_\nu(x).$$

N_ℓ is the length of the loop, $w_t \in \mathbb{Z}$ is the winding number in temporal direction, and N_- counts the total number of backward hoppings[10]. Therefore there is a sign problem remaining in this formulation. This is due to the closing of the loop, the antiperiodic boundary conditions for fermions in the temporal direction, the backward hoppings, and the staggered phases $\eta_\nu(x)$. At $\mu = 0$ the sign problem can be circumvented by a clever combination of similar configurations[101]. For $\mu > 0$, however, a sign problem reappears.

Figure **4.1** shows an example configuration of the dual variables. The configuration has two baryonic loops: one that closes trivially and one with a winding in the temporal direction, introducing a factor $e^{3\mu N_t}$ to the weight. Notice that this produces the correct factor $\exp(3\mu N_t) = \exp(\mu_{Baryon}/T)$, as it should. (Here μ_{Baryon} is measured in physical units, as opposed to the conventions so far, that μ is measured in lattice units.) The total sign of the configuration is positive. It is important to notice that no site is unoccupied and that the baryon loops are completely disjoint from the mesonic sites, which is both due to the constraints from the Grassmann integration.

[10] One could equally well use the number of forward hoppings, since for even-sized lattices the two give the same parity.

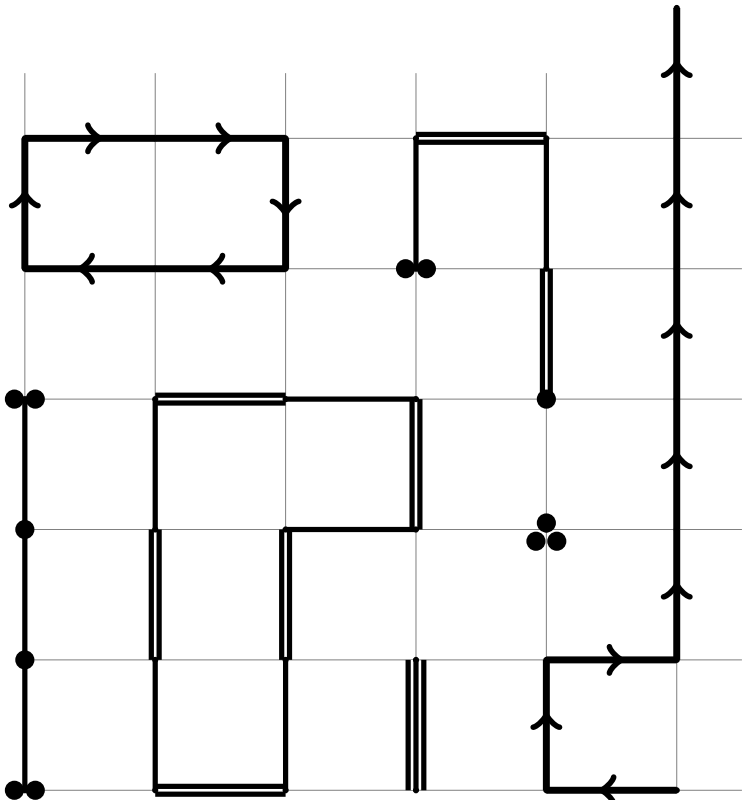

Figure 4.1 An example configuration on a 6×6 lattice for the dual variables k, n, b. Dots symbolize sites where n is nonzero. The mesonic variables k are shown as unoriented bonds. The baryonic variables b are visualized as directed bonds, forming closed loops. One trivially closed loop and one that winds around in the temporal direction are shown. The loop with the temporal winding introduces a factor $e^{3\mu N_t}$ to the weight. The total sign of this particular configuration is positive.

4.2 QCD with scalar quarks

The following section is based on the publications [8,106] together with Falk Bruckmann.

As we have seen in the previous section, QCD still has a sign problem even in the dual formulation[11]. Nevertheless, the dual formulation makes it transparent where the sign problem comes from. Namely, signs are

[11] This refers to the strong coupling limit. Full QCD also has a sign problem, but until now there has not been a dual formulation for full QCD.

introduced by (i) the closing of the fermion loops, (ii) the antiperiodic temporal boundary conditions for fermions, (iii) the staggered phases, and (iv) the relative sign in the Dirac operator, since it is a first order derivative. Hence it seems that the sign problem is purely fermionic in nature.

In this way it may be expected that there would be no sign problem if quarks were scalar particles rather than fermions. Even so, this conjecture is nontrivial since the $SU(3)$ gauge links are complex and the group integral are not necessarily positive[22]. In the following, this conjecture will be analyzed. The setup is more or less the same as in the previous section, that is, we still work in the strong coupling regime, only now the fermionic action S_f is replaced by a bosonic one S_b.

$$S_b = \sum_x \sum_{f=1}^{N_f} \Bigg((m^2 + 2d)\phi^{f\dagger}(x)\phi^f(x) - \tag{4.15}$$
$$- \sum_{\nu=0}^{d-1} \Big(e^{\mu\delta_{\hat{\nu},\hat{0}}} \phi^{f\dagger}(x) U_\nu(x) \phi^f(x+\hat{\nu}) + e^{-\mu\delta_{\hat{\nu},\hat{0}}} \phi^{f\dagger}(x+\hat{\nu}) U_\nu^\dagger(x) \phi^f(x) \Big) \Bigg) .$$

In the first line there is a *mass* term for the *complex scalar field* ϕ^f for each flavor. For simplicity we take all the flavors to have the same mass m; nevertheless, the following discussion holds true also for different masses m^f. The second line, together with the $2d$-term in the first, is a *discretized covariant* Laplacian in d dimensions, using the $SU(3)$ gauge field U. For the temporal direction $\hat{\nu} = \hat{0}$ we couple a chemical potential μ to the scalar field in the usual way.

We can rewrite the action in the following form:

$$S_b = \sum_x \Bigg(- \sum_\nu \mathrm{Tr}\Big(\alpha_\nu J_\nu(x) U_\nu(x) + \alpha_\nu^{-1} J_\nu^\dagger(x) U_\nu^\dagger(x) \Big) \tag{4.16}$$
$$+ \sum_f \Big((2d + m^2) \phi^{f\dagger}(x) \phi^f(x) \Big) \Bigg),$$

$$J_\nu(x) = \sum_f \phi^f(x+\hat{\nu}) \phi^{f\dagger}(x) \qquad \text{forward hopping,} \tag{4.17}$$

$$J_\nu^\dagger(x) = \sum_f \phi^f(x) \phi^{f\dagger}(x+\hat{\nu}) \qquad \text{backward hopping,} \tag{4.18}$$

where we constructed the forward- and backward-hopping matrices J and $J^\dagger$ from the scalar fields at adjacent sites and $\alpha_\nu = e^{\mu\delta_{\hat{\nu},\hat{0}}}$ is the

fugacity factor. In the case of $\mu = 0$ or when μ is purely imaginary, the fugacity factor fulfills $\alpha_\nu^{-1} = \alpha_\nu^*$, resulting in a real action, $S_b \in \mathbb{R}$. However, in general for $\mu \neq 0$ the action becomes complex and we end up with a sign problem, similar to the fermionic case.

4.2.1 Assessing the sign problem

In order to assess the severity of the sign problem we integrate over the scalar fields ϕ in the partition function Z, resulting in a determinant representation:

$$Z = \int \mathcal{D}U \int \mathcal{D}\phi \mathcal{D}\phi^\dagger e^{-S} = \int \mathcal{D}U \frac{1}{\det(M[U])^{N_f}}, \tag{4.19}$$

$$M_{x,y} = (m^2 + 2d)\delta_{x,y} - \sum_\nu \left(e^{\mu \delta_{\hat{\nu},\hat{0}}} U_\nu(x) \delta_{x+\hat{\nu},y} + e^{-\mu \delta_{\hat{\nu},\hat{0}}} U_\nu(x)^\dagger \delta_{y+\hat{\nu},x} \right).$$

A measure for the severity of the sign problem is the *phase quenched reweighting factor*:

$$r^{pq} = \left\langle \left(\frac{|\det(M)|}{\det(M)} \right)^{N_f} \right\rangle. \tag{4.20}$$

For $\mu = 0$ the determinant is real and positive, and hence $r^{pq} = 1$. For large μ the dominating contribution to the determinant is again positive, such that also here $r^{pq} = 1$. This comes from the fact that $\det M$ is a polynomial in e^μ, i.e., $\det M = e^{3V\mu}(1 + \mathcal{O}(e^{-\mu}))$. In the range $\mu \in [0.5, 2]$ the reweighting factor differs significantly from 1. For these intermediate values of the chemical potential, delicate cancellations can occur, as can be seen in Figure **4.2**.

In order to compare different (lattice) volumes V it is useful to consider the *free energy density* difference Δf, which is defined by

$$r^{pq} = e^{-V\Delta f}. \tag{4.21}$$

A naive extrapolation of the data points in Figure **4.3** yields the values $\mu_c = 1.233(1)$ and $\Delta f_c = 1.33(2)$ for where the sign problem is most severe. This would result in reweighting factors $r^{pq}(\mu_c) \approx 10^{-10}$ already for a 4×4 lattice. Hence it is not feasible to simulate the theory around μ_c with reweighting. Therefore another representation of the partition function is needed.

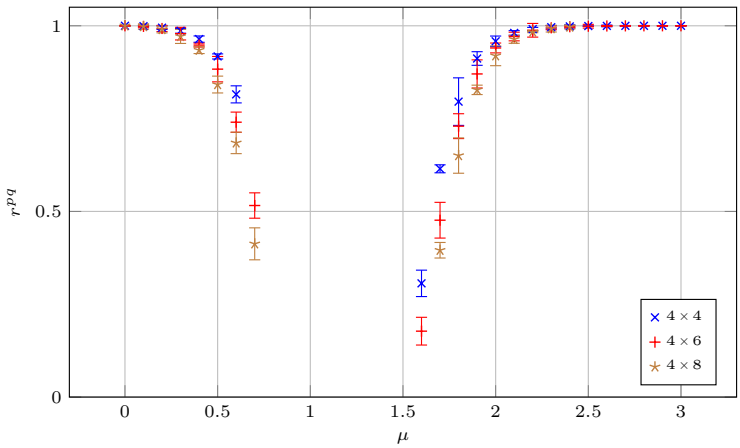

Figure 4.2 The phase quenched reweighting factor r^{pq} is shown as a function of the chemical potential μ in lattice units. The simulation parameters are $N_f = 3$, $d = 2$, and 10^5 configurations were used. The different data sets correspond to different lattice sizes. In the region $\mu \in [0.7, 1.6]$ the autocorrelation becomes so large that neither the errors, nor the mean values are reliable any more, and thus these points are omitted in the plot.

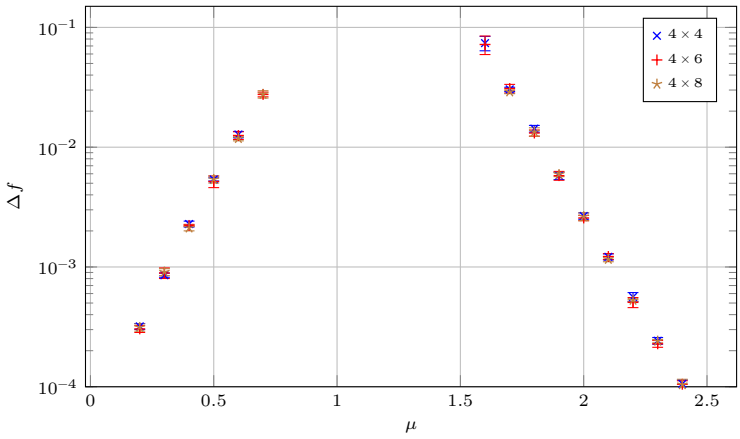

Figure 4.3 The *free energy density* Δf as a function of μ. A naive extrapolation, yields $\mu_c = 1.233(1)$ and $\Delta f_c = 1.33(2)$.

4.2.2 Dualizing scalar QCD

We start from eq. (4.16) for the action. In the partition function

$$Z = \int \mathcal{D}\phi \mathcal{D}\phi^\dagger \int \mathcal{D}U \prod_{x,\nu} e^{\mathrm{Tr}(J_\nu(x)U_\nu(x) + U_\nu^\dagger(x) J_\nu^\dagger(x))} \prod_{x,f} e^{-(2d+m^2)|\phi^f(x)|^2} \quad (4.22)$$

we perform the integration over the gauge fields U first. The $SU(3)$ integral over a single link can be performed[107], giving a five-fold sum[12]

$$I(J,\alpha_\nu) = \int dU e^{\mathrm{Tr}(\alpha_\nu JU + \alpha_\nu^{-1} U^\dagger J^\dagger)} = \\ = \sum_{j,k,l,n,\bar{n}=0}^{\infty} \frac{2\alpha_\nu^{3(n-\bar{n})}}{g_{(1)}! g_{(2)}!} \frac{X^j Y^k Z^l \Delta^n \bar{\Delta}^{\bar{n}}}{j!k!l!n!\bar{n}!}, \quad (4.23)$$

where $g_{(1)}$ and $g_{(2)}$ are shorthands for

$$g_{(1)} = k + 2l + n + \bar{n} + 1 \quad \text{and} \quad g_{(2)} = j + 2k + 3l + n + \bar{n} + 2. \quad (4.24)$$

The other variables in eq. (4.23) are functions of the hopping matrices J and $J^\dagger$:

$$X = \mathrm{Tr}(JJ^\dagger), \quad Y = \frac{1}{2}[X^2 - \mathrm{Tr}((JJ^\dagger)^2)], \quad Z = \det(JJ^\dagger), \quad (4.25)$$
$$\Delta = \det(J), \qquad \bar{\Delta} = \det(J^\dagger).$$

The $SU(3)$ integrals in eq. (4.22) factorize and thus we can apply this expansion for each bond separately,

$$Z = \sum_{\{j,k,l,n,\bar{n}\}} \int \mathcal{D}\phi \mathcal{D}\phi^\dagger \rho(|\phi|) \prod_{x,\nu} \left(\frac{2\alpha_\nu^{3(n-\bar{n})}}{g_{(1)} g_{(2)}} \frac{X^j Y^k Z^l \Delta^n \bar{\Delta}^{\bar{n}}}{j!k!l!n!\bar{n}!} \right)_\nu (x),$$
$$\rho(|\phi|) = \prod_{x,f} e^{-(2d+m^2)|\phi^f(x)|^2}, \quad (4.26)$$

where $[...]_\nu(x)$ means that all the functions $X, Y, Z, \Delta, \bar{\Delta}$ and variables $j, k, l, n, \bar{n}$ have a direction index and a position argument. In this way the partition function is now written in terms of a sum over the dual variables, $j, k, l, n, \bar{n}$, and an integral over the scalar fields ϕ. Thus a configuration in this new representation is given by a set of values for the dual variables $j, k, l, n, \bar{n}$ on all bonds, together with a set of values for the scalar field ϕ on each site. More details on the admissible configurations of the dual variables will be discussed in the next section.

[12] Also the term $(\det J + \det J^\dagger)^n$ in [107] has been expanded into separate terms. Also there is a typo in the definition of Y in the reference.

As can be seen from the partition function, the only μ-dependence comes from the fugacity factor $\alpha_\nu = e^{\mu\delta_{\nu,\hat{0}}}$, which itself only contributes when n or $\bar{n}$ are nonzero. For this reason we call n and $\bar{n}$ *baryonic* variables. Similarly, Δ and $\bar{\Delta}$ are called *baryonic building blocks*, since they describe the hopping of three quarks or antiquarks on a bond.

The other variables introduce no μ-dependence; consequently, j, k, and l will be called *mesonic* variables. And, since X, Y, and Z describe the hopping of equal amounts of quarks and antiquarks on a bond, they are called *mesonic building blocks*.

4.2.3 Discussion

To assess the sign problem in the dual formulation we have to analyze the functions X, Y, Z, Δ, and $\bar{\Delta}$: The functions X, Y, and Z only depend on $JJ^\dagger$. Now $JJ^\dagger$ is a positive matrix, with eigenvalues $\lambda_i \geq 0$. Therefore we have

$$\begin{aligned} X &= \sum_i \lambda_i && \geq 0, \\ Y &= \frac{1}{2}\left[\sum_{i,j}\lambda_i\lambda_j - \sum_i \lambda_i^2\right] = \sum_{i<j}\lambda_i\lambda_j && \geq 0, \\ Z &= \prod_i \lambda_i && \geq 0. \end{aligned} \tag{4.27}$$

For Δ and $\bar{\Delta}$ the situation is different, as they depend only on J and $J^\dagger$, respectively. And since J and $J^\dagger$ in general have complex eigenvalues, the same is true for Δ and $\bar{\Delta}$. One can work out that

$$\begin{aligned} \Delta_\nu(x) &= \det\Big(\sum_{f=1}^{N_f}\phi^f(x+\hat{\nu})\phi^{f\dagger}(x)\Big) \\ &= \frac{1}{3!}\sum_{f_1,f_2,f_3=1}^{N_f} d_{f_1f_2f_3}(x+\hat{\nu})d^*_{f_1f_2f_3}(x) \\ &= \frac{1}{3!}\sum_{\sigma} d_{\sigma_1\sigma_2\sigma_3}(x+\hat{\nu})d^*_{\sigma_1\sigma_2\sigma_3}(x), \end{aligned} \tag{4.28}$$

where $d_{f_1f_2f_3}(x) = \det(\phi^{f_1}(x)|\phi^{f_2}(x)|\phi^{f_3}(x))$ denotes the determinant with the different flavors as columns. The map σ runs over all choices of 3 out of N_f, i.e., $\sigma : \{1,2,3\} \to \{1,...,N_f\}$. The validity of eq. (4.28) can easily be shown by writing the determinant with Levi-Civita-Symbols:

$$\begin{aligned}\det\Big(\sum_f \phi^f \varphi^{f\dagger}\Big) &= \frac{1}{3!}\sum_{f_1,f_2,f_2} \varepsilon_{ijk}\varepsilon_{lmn}\phi_i^{f_1}\varphi_l^{*f_1}\phi_j^{f_2}\varphi_m^{*f_2}\phi_k^{f_3}\varphi_n^{*f_3} \\ &= \frac{1}{3!}\sum_{f_1,f_2,f_2} \varepsilon_{ijk}\phi_i^{f_1}\phi_j^{f_2}\phi_k^{f_3}\Big(\varepsilon_{lmn}\varphi_l^{f_1}\varphi_m^{f_2}\varphi_n^{f_3}\Big)^* \\ &= \frac{1}{3!}\sum_{f_1,f_2,f_2} \det(\phi^{f_1}|\phi^{f_2}|\phi^{f_3})\det(\varphi^{f_1}|\varphi^{f_2}|\varphi^{f_3})^*. \quad (4.29)\end{aligned}$$

As a consequence there is a flavor antisymmetry in the baryonic hopping term $\Delta = \det J$, and likewise for the antibaryon $\bar{\Delta} = \det J^\dagger$. This makes it also clear that for $N_f < 3$, there cannot be any dependence on the chemical potential, as then $\Delta = \bar{\Delta} = 0$. The reason for this is that the determinant dictates that a baryon must be *antisymmetric* in *three* flavors, compensating the color antisymmetry. Hence there is also no sign problem for one and two flavors in the dual formulation. Nevertheless, for $N_f \geq 3$ apparently a sign problem remains.

4.2.4 Three flavors

In the following we restrict the discussion to the simplest nontrivial case, $N_f = 3$. In this case the sum in eq. (4.28) collapses to a single term

$$\Delta_\nu(x) = \det\left(\phi^1|\phi^2|\phi^3\right)(x+\hat{\nu})\det\left(\phi^1|\phi^2|\phi^3\right)^*(x). \quad (4.30)$$

In order to approach the remaining sign problem, notice that the partition function also contains the integration over the matter field ϕ. Performing these analytically becomes increasingly complicated, when several powers of the mesonic and baryonic building blocks are involved. (The convergence of these integrals is guaranteed because the Gaussian factor in $\rho(|\phi|)$ suppresses large field values.) Thus it seems advantageous to do the ϕ integrations also numerically. Nevertheless, we can use one important feature of this integration. At each site and for each flavor- and color-component the integrals are of the form

$$\int d\phi d\phi^*\, e^{-\#|\phi|^2}(\phi)^A(\phi^*)^B \sim \delta_{AB}, \quad (4.31)$$

where δ_{AB} comes from integrating over the phase of ϕ. As a consequence, at each site there must be an equal power of ϕ and ϕ^* fields, otherwise that term will not contribute to the partition function. Only when the constraint $A_a^f(x) \stackrel{!}{=} B_a^f(x)$ on the exponents in eq. (4.31) is fulfilled

for each flavor f and color component a at each site, that term will contribute to the partition function.

It will also be useful to introduce *coarser constraints* by summing over the different flavors and colors, yielding $\sum_{f,a} A_a^f(x) = \sum_{f,b} B_a^f(x)$. The mesonic building blocks contain ϕ and ϕ^* in equal amounts on the same site. Hence they already fulfill the constraint. The baryonic building blocks are different; they are of third order in $\phi_a^f(x)^*$ and $\phi_a^f(x+\hat{\nu})$. Thus a single baryonic building block cannot fulfill the constraint on its own. Nevertheless, when other baryonic building blocks are attached to both the sites x and $x+\hat{\nu}$, the constraint can be fulfilled on these sites. This yields a constraint on the baryonic dual variables:

$$\sum_{\nu} [m_\nu(x) - m_\nu(x-\hat{\nu})] = 0, \tag{4.32}$$

with

$$m_\nu(x) = n_\nu(x) - \bar{n}_\nu(x). \tag{4.33}$$

In fact this is just a discrete version of the current conservation equation $\sum_\nu \partial_\nu m_\nu(x) = 0$ for the net baryon current $m_\nu = (n-\bar{n})_\nu$. In the end this has the consequence that baryonic building blocks must come in closed loop configurations. The baryon chemical potential 3μ couples to the conserved charge of the net baryon current, namely, $\sum_x m_0(x)$. Furthermore, only loops that wind the temporal direction will introduce a μ-dependence.

When considering closed loops, ℓ, of baryonic building blocks, we find that, in our $N_f = 3$ case, they have the weight (ignoring the factorials in the denominator for the moment)

$$\begin{aligned} W_\ell(\mu) &\sim e^{3\mu N_t w_t} \prod_{(x,\nu)\in\ell} d^*_{123}(x) d_{123}(x+\hat{\nu}) = \\ &= e^{3\mu N_t w_t} \prod_{(x,\nu)\in\ell} \left| \det(\phi^1(x)|\phi^2(x)|\phi^3(x)) \right|^2 \geq 0, \end{aligned} \tag{4.34}$$

where w_t is the winding number in the temporal direction. This shows that in this case there is *no longer a sign problem* at nonzero chemical potential.

The diagrammatic representation of the dual configurations is in some ways similar and in others different to the fermionic case. Figure **4.4** shows an example of such a configuration. The mesonic variables are not directional, while the baryonic ones clearly are oriented, just as in the fermionic case. Notable differences are that baryon loops can be intersecting, that arbitrary large occupation numbers are allowed, and

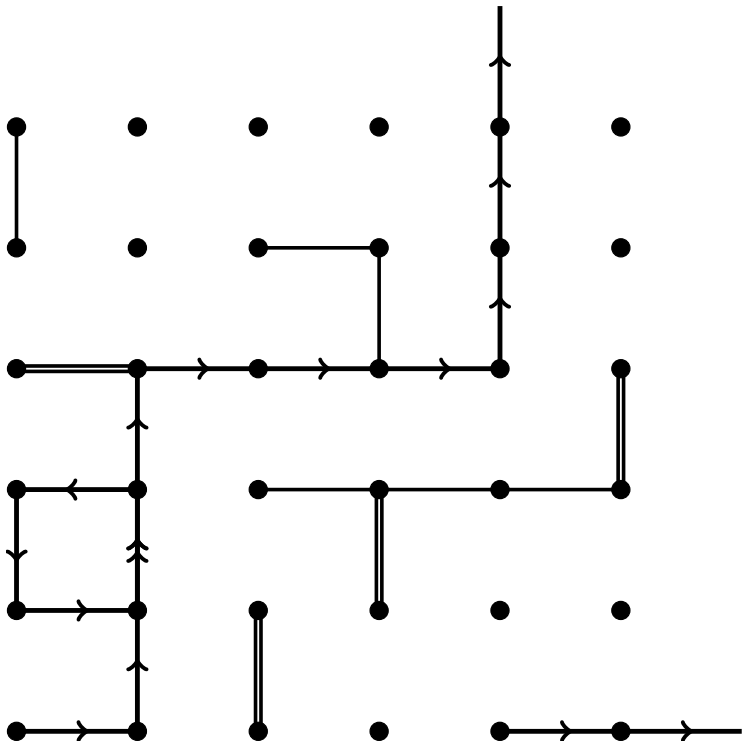

Figure 4.4 An example configuration on a 6×6 lattice of the dual variables. Baryonic bonds are indicated with arrows. All the different mesonic bonds are shown as unoriented lines for simplicity. (Note that dots do not correspond to mass terms as was the case in QCD in Figure **4.1**.)

that even completely unoccupied sites are possible as well. Also the mass is treated differently: together with the spacetime dimension it determines the width of the Gaussian distribution of the scalar fields.

In the dual representation a hybrid strategy can be applied for updating the configurations. Namely, for dual variables j, k, l, $n+\bar{n}$ local updates can be used. The same is true for the scalar field ϕ. For $n-\bar{n}$ on the other hand worm algorithms[6,34] seem promising because the closed loop constraints have to be preserved.

4.2.5 More flavors

As we have seen, the sign problem in the dual formulation can be eliminated completely for three flavors. For $N_f > 3$ it can be shown numerically that a simple closed loop prescription as before does not

result in positive weights. The following discussion focuses on $N_f = 4$ as an example of the technical difficulties that are encountered with more flavors.

Before we had the situation that only two baryonic factors had to be multiplied at a given site. Namely, d_{123} from the ending of the incoming bond and d^*_{123} from the beginning of the outgoing bond, or vice versa. Now the sum in eq. (4.28) consists of four terms, $\#d_{123} + \#d_{124} + \#d_{134} + \#d_{234}$, where the determinants on the neighboring site are absorbed into the (different) coefficients, denoted as #. Considering this to be part of a closed loop, the sum is multiplied by the another such sum, $\#d^*_{123} + \#d^*_{124} + \#d^*_{134} + \#d^*_{234}$, of the outgoing bond. When the multiplication is carried out, there will obviously be mixed terms, which are in general not positive.

This suggests that *finer* constraints than above have to be used, e.g., not summing over the flavor indices for the constraint. Consider, for example, the mixed term $d_{123}(x)d^*_{124}(x)$. There the 'mismatch' is that $\phi^3(x)$ and $\phi^4(x)^*$ is contained once, but not their complex conjugates. Therefore such a term will not contribute, as it vanishes under the ϕ integration, cf. eq. (4.31). Hence only the terms with equal flavor combinations, $d_{f_1f_2f_3}d^*_{f_1f_2f_3}$, give a contribution to the partition function.

However, this could change if also mesonic contributions are considered. If we connect a mesonic building block X to the baryonic loop only at the site x, the missing complex conjugate pair $\phi^3(x)^*$ and $\phi^4(x)$ is present. Nevertheless, this conjugate pair is also accompanied by $\phi^3(y)$ and $\phi^4(y)^*$ at some y near x, and these do not survive the ϕ integration, so we are in the same situation as above, that only equal flavor combinations, $|d_{f_1f_2f_3}|^2$, of the baryon loop contribute.

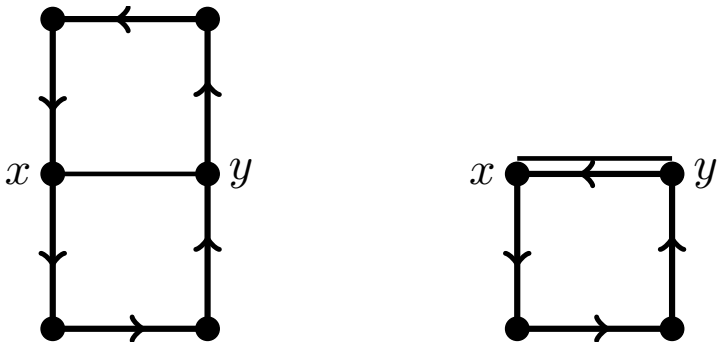

Figure 4.5 Two simple examples of a single meson connected to a baryon loop, resulting in a (nontrivial) positive weight.

We can go further, and consider the mesonic building block X connected to two sites x and y which are both part of a baryon loop, as depicted in Figure **4.5**. The different flavor combinations (1,2,3), (1,2,4), (1,3,4), (2,3,4) have to traverse the baryon loop separately, due to the ϕ integration. Only on the sites x and y, where the meson is connected, also the mixed terms play a role besides the $|d_{f_1 f_2 f_3}|^2$-contribution. A typical nonvanishing mixed contribution reads

$$\begin{aligned}&\det(\phi^1|\phi^2|\phi^3)(x)\det(\phi^1|\phi^2|\phi^3)(y)^*\det(\phi^1|\phi^2|\phi^4)(x)\det(\phi^1|\phi^2|\phi^4)(y)^*\\&\times\ \mathrm{Tr}(\phi^4(x)\phi^4(y)^\dagger\phi^3(y)\phi^3(x)^\dagger)\\&=\varepsilon_{abc}\phi^1_a\phi^2_b\phi^3_c\phi^4_d(x)\varepsilon_{ABC}\phi^{1*}_A\phi^{2*}_B\phi^{4*}_C\phi^{3*}_d(x)\times(x\to y)^*.\end{aligned}\tag{4.35}$$

Of course, also other flavor combinations with the same structure are possible. The ϕ integrations are only nonvanishing if $A = a$, $B = b$, $c = d = C$. In that way at site x only a positive factor $|\phi^1|^2|\phi^2|^2|\phi^3|^2|\phi^4|^2$ remains, and similar for the site y. Thus also the total weight of such a configuration is positive.

All in all, these examples suggest that also for $N_f > 3$ the sign problem can be eliminated in the dual theory, when the right kind of constraint is used. For this one has to break down the dual variables j, k, l, n and $\bar{n}$ into components for all the different flavor combinations through multinomial expansions. Keeping track of the contributing terms becomes rather intricate, especially when higher occupation numbers are encountered, so it remains to be seen whether this is a viable option.

4.3 Conclusion and outlook

We have seen that dualization can be applied to both fermionic and scalar QCD in a similar manner. However, in the fermionic case, a sign problem remains in the dual formulation. This is due to the fermionic anticommutation relations, the relative sign difference of the two terms of the Dirac operator, the antiperiodic boundary conditions in the time direction, and the staggered phases. In the scalar case, all these are are absent. Consequently, it could be shown that scalar QCD has, indeed, no sign problem in the dual formulation for up to $N_f \leq 3$ flavors. For more flavors the formulation becomes vastly more complicated, so it is not clear whether the formulation is positive.

So far, we have only considered the strong coupling limit. In recent years, there have been several successful attempts to also find a dual formulation for the gauge sector[108–111]. Essentially, they all work by

integrating over the gauge field, at the expense of introducing new field variables. In case of [109] these are matrix valued fields living on the links between sites. Ref. [110] works with additional scalar fields on the plaquettes, termed *induced* fields. Ref. [111] works with so called color flux variables. In the context of scalar QCD it seems that the induced fields could be incorporated most naturally into the existing framework. Nevertheless, how to do this is not straight forward because the induced fields most certainly will increase the number of scalar fields beyond three flavors. Thus, if it turns out that the sign problem can be eliminated for $N_f > 3$, a dual representation of full scalar QCD seems to be in reach.

5 Summary

This thesis has analyzed a number of different nonperturbative aspects of QCD and similar theories. On the one hand, the subject of localization was covered in case of QCD, an Ising-Anderson toy model and $CP(N-1)$. On the other, one of the first studies of Landau levels of quarks from first principles was presented. Finally, the sign problem of nonzero density in QCD was studied using either fermionic or scalar quarks.

Localization in QCD extended previous work[15–18] on the subject to the case of a background magnetic field. At zero magnetic field it had been found that below the QCD transition temperature the Dirac operator essentially behaves like a random unitary matrix. This entails strong correlations between neighboring eigenvalues and delocalized eigenmodes. Above the transition temperature, on the other hand, this situation changes. The low modes near the origin become localized, while the high modes remain extended. In between these two there is a point of critical statistics in the spectrum, the mobility edge. From other studies on background magnetic fields[9,10,50] it was known that observables susceptible to the low end of the spectrum of the Dirac operator show a strong dependence on the magnetic field. Hence this should be visible in the spectrum as well. As was shown this is, indeed, the case. The overall tendency of the magnetic field is to push the spectrum toward lower eigenvalues. Likewise this also lowers the mobility edge.

Similar observations could be made in a simple three dimensional Ising-Anderson model. A background magnetic field can be introduced in an analogous way as in QCD. Also here the magnetic field shifts the spectrum to lower eigenvalues, albeit in a much simpler manner than in QCD. Nevertheless, this shows that the essential features of localization in QCD are also captured by a much simpler model.

Furthermore, there are a number of toy models, $CP(N-1)$ in particular, that serve as a playground to test out new ideas and methods for QCD. These also share a number of properties with the latter. Among the most notable ones are the dynamical generation of a mass gap and asymptotic freedom. Hence the question arises whether in $CP(N-1)$ localization can also be observed. This was shown to be the case, depending on the dimensionality of the model. In two dimensions all modes appear to be localized. In three dimensions an Anderson-transition from localized to delocalized modes takes place in the spectrum, similar to QCD.

Another part of this thesis dealt with Landau levels of quarks in QCD. In two dimensions the lowest Landau level is separated from the rest and can easily be identified by simple mode counting. In four dimensions the momenta from the additional two directions make the Landau levels overlap, so they can no longer be identified by the eigenvalues alone. Nevertheless, it was possible to find a way to identify the lowest Landau level using the eigenmodes themselves. With this presciption the lowest Landau level dominance was investigated for different observables at several different temperatures and magnetic fields.

The last part of this thesis was concerned with the sign problem at nonzero density in QCD. Using dual variables it has been possible to eliminate the sign problem in a number of different systems. Nevertheless, from earlier works it is known that dual formulations of QCD still suffer from a remnant sign problem. The remaining sign problem seems to come exclusively from the fermionic nature of the quarks. Indeed, as could be shown, the sign problem is absent if quarks were *scalar* particles. In that case it depends on the number of flavors whether there is a sign problem. For one and two flavors the dependence on the chemical potential is completely absent, that is, no baryons can be formed. For three flavors, on the other hand, baryons can be formed and the resulting representation has no longer a sign problem. For more than three flavors at first sight there seems to be a sign problem present. Nevertheless, a closer look suggests that this sign could also be absent, when considering baryons of only three distinct flavors. In the end, if the sign problem is, indeed, absent for more than three flavors, this could lead the way to going beyond strong coupling, i.e., also taking the gauge action into account.

All in all, these findings shed some new light on the nonperturbative aspects of strongly coupled theories. In particular, the results for localization in $CP(N-1)$ models may have some relevance for antiferromagnetic spin models[112,113] in condensed matter physics. On the other hand, $CP(N-1)$ models in higher dimensions may be renormalizable nonperturbatively[38]. This would render them *asymptotically safe* and thus also interesting in the context of particle physics as well as quantum gravity.

Localization in QCD with a background magnetic field adds to our understanding of the QCD phase diagram, by giving new insight at the level of quark spectra. Also Landau levels in QCD fall into a similar category. Furthermore, the findings on Landau levels can be used in

effective model calculations. In this way there can be better control over the errors involved when using the lowest Landau level approximation.

Lastly, scalar QCD could have some applications in grand unified theories. In particular, this is the case when Gauge-Higgs models are involved. Adding a Higgs-potential term is just a minor modification of the action used in this thesis, leaving the technical aspects unchanged.

Bibliography

[1] A. Salam and J.C. Ward, Weak and electromagnetic interactions, *Nuovo Cim.* **11** 568-577 (1959).

[2] S.L. Glashow, Partial Symmetries of Weak Interactions, *Nucl. Phys.* **22** 579-588 (1961).

[3] S. Weinberg, A Model of Leptons, *Phys. Rev. Lett.* **19** 1264-1266 (1967).

[4] Y. Aoki, Z. Fodor, S.D. Katz, and K.K. Szabo, The QCD transition temperature: Results with physical masses in the continuum limit, *Phys. Lett.* **B643** 46-54 (2006). [hep-lat/0609068]

[5] U.W. Heinz, The Quark gluon plasma at RHIC, *Nucl. Phys.* **A721** 30-39 (2003). [nucl-th/0212004]

[6] D. Göschl, C. Gattringer, A. Lehmann, and C. Weis, Simulation strategies for the massless lattice Schwinger model in the dual formulation, *Nucl. Phys.* **B924** 63-85 (2017). [1708.00649]

[7] F. Bruckmann, C. Gattringer, T. Kloiber, and T. Sulejmanpasic, Dual lattice representations for O(N) and CP(N−1) models with a chemical potential, *Phys. Lett.* **B749** 495-501 (2015). ([Erratum: Phys. Lett.B751,595(2015)]) [1507.04253]

[8] F. Bruckmann and J. Wellnhofer, Diagrammatic representation of scalar QCD and sign problem at nonzero chemical potential, *Phys. Rev.* **D97**(1), 014501 (2018). [1710.08243]

[9] G.S. Bali, F. Bruckmann, G. Endrodi, Z. Fodor, S.D. Katz, S. Krieg, A. Schafer, and K.K. Szabo, The QCD phase diagram for external magnetic fields, *JHEP* **02** 044 (2012). [1111.4956]

[10] F. Bruckmann, G. Endrodi, and T.G. Kovacs, Inverse magnetic catalysis and the Polyakov loop, *JHEP* **04** 112 (2013). [1303.3972]

[11] G. Endrodi, Critical point in the QCD phase diagram for extremely strong background magnetic fields, *JHEP* **07** 173 (2015). [1504.08280]

[12] I.A. Shovkovy, Magnetic Catalysis: A Review, *Lect. Notes Phys.* **871** 13-49 (2013). [1207.5081]

[13] J.O. Andersen, W.R. Naylor, and A. Tranberg, Phase diagram of QCD in a magnetic field: A review, *Rev. Mod. Phys.* **88** 025001 (2016). [1411.7176]

[14] V.A. Miransky and I.A. Shovkovy, Quantum field theory in a magnetic field: From quantum chromodynamics to graphene and Dirac semimetals, *Phys. Rept.* **576** 1-209 (2015). [1503.00732]

[15] A.M. Garcia-Garcia and J.C. Osborn, Chiral phase transition in lattice QCD as a metal-insulator transition, *Phys. Rev.* **D75** 034503 (2007). [hep-lat/0611019]

[16] T.G. Kovacs and F. Pittler, Poisson to Random Matrix Transition in the QCD Dirac Spectrum, *Phys. Rev.* **D86** 114515 (2012). [1208.3475]

[17] M. Giordano, T.G. Kovacs, and F. Pittler, Universality and the QCD Anderson Transition, *Phys. Rev. Lett.* **112**(10), 102002 (2014). [1312.1179]

[18] L. Ujfalusi, M. Giordano, F. Pittler, T.G. Kovács, and I. Varga, Anderson transition and multifractals in the spectrum of the Dirac operator of Quantum Chromodynamics at high temperature, *Phys. Rev.* **D92**(9), 094513 (2015). [1507.02162]

[19] D.R. Hofstadter, Energy levels and wave functions of Bloch electrons in rational and irrational magnetic fields, *Phys. Rev.* **B14** 2239-2249 (1976).

[20] M.E. Peskin and D.V. Schroeder, *An Introduction to quantum field theory* (Addison-Wesley, Reading, USA, 1995).

[21] T. Muta, *Foundations of Quantum Chromodynamics: An Introduction to Perturbative Methods in Gauge Theories, (3rd ed.)*, Vol. 78 (World Scientific, Hackensack, N.J., 2010).

[22] M. Creutz, *Quarks, gluons and lattices* (Cambridge Univ. Press, Cambridge, UK, 1985).

[23] C. Gattringer and C.B. Lang, Quantum chromodynamics on the lattice, *Lect. Notes Phys.* **788** 1-343 (2010).

[24] D.J. Gross and F. Wilczek, Ultraviolet Behavior of Nonabelian Gauge Theories, *Phys. Rev. Lett.* **30** 1343-1346 (1973).

[25] H.D. Politzer, Reliable Perturbative Results for Strong Interactions?, *Phys. Rev. Lett.* **30** 1346-1349 (1973).

[26] U. Aglietti, Introduction to perturbative QCD, In 1st School on Field Theory and Gravitation Vitoria, Brazil, April 15-19, 1997 (1997). [hep-ph/9705277]

[27] M. Luscher and P. Weisz, On-Shell Improved Lattice Gauge Theories, *Commun. Math. Phys.* **97** 59 (1985). ([Erratum: Commun. Math. Phys.98,433(1985)])

[28] H.B. Nielsen and M. Ninomiya, No Go Theorem for Regularizing Chiral Fermions, *Phys. Lett.* **105B** 219-223 (1981).

[29] S. Carrozza, T. Krajewski, and A. Tanasa, Using Grassmann calculus in combinatorics: Lindström-Gessel-Viennot lemma and Schur functions (2016). [1604.06276]

[30] S.R. Sharpe, Rooted staggered fermions: Good, bad or ugly?, *PoS* **LAT2006** 022 (2006). [hep-lat/0610094]

[31] A. Ukawa, Lectures on lattice QCD at finite temperature, In Phenomenology and lattice QCD. Proceedings: Uehling Summer School, Seattle, USA, Jun 21-Jul 2, 1993 (1995).

[32] N. Metropolis, A.W. Rosenbluth, M.N. Rosenbluth, A.H. Teller, and E. Teller, Equation of state calculations by fast computing machines, *J. Chem. Phys.* **21** 1087-1092 (1953).

[33] S. Duane, A.D. Kennedy, B.J. Pendleton, and D. Roweth, Hybrid Monte Carlo, *Phys. Lett.* **B195** 216-222 (1987).

[34] N. Prokof'ev and B. Svistunov, Worm Algorithm for Problems of Quantum and Classical Statistics, In Understanding Quantum Phase Transitions, Lincoln D. Carr,ed. Taylor & Francis, Boca Raton, 2010 (2009). [0910.1393]

[35] Chapman and Hall/CRC, *Handbook of Markov Chain Monte Carlo (Chapman & Hall/CRC Handbooks of Modern Statistical Methods)*, 1 ed. (Chapman and Hall/CRC, 2011).

[36] S. Weinzierl, Introduction to Monte Carlo methods, (2000). [hep-ph/0006269]

[37] K. Binder and D.P. Landau, *A Guide to Monte Carlo Simulations in Statistical Physics*, 2 ed. (Cambridge University Press, 2005).

[38] A. Codello and R. Percacci, Fixed Points of Nonlinear Sigma Models in d>2, *Phys. Lett.* **B672** 280-283 (2009). [0810.0715]

[39] M. Shifman and A. Yung, Two-Dimensional Sigma Models Related to Non-Abelian Strings in Super-Yang-Mills, In Proceedings, 100th anniversary of the birth of I.Ya. Pomeranchuk (Pomeranchuk 100): Moscow, Russia, June 5-6, 2013 (2014). [1401.7067]

[40] M.-L. Mehta, *Random Matrices* (Elsevier Science, 2004).

[41] B. Eynard, T. Kimura, and S. Ribault, Random matrices, (2015). [1510.04430]

[42] R.G. Edwards, U.M. Heller, J.E. Kiskis, and R. Narayanan, Quark spectra, topology and random matrix theory, *Phys. Rev. Lett.* **82** 4188-4191 (1999). [hep-th/9902117]

[43] Mehta, On the statistical properties of the level-spacings in nuclear spectra, *Nucl. Phys. A* **18** 395-419 (1960).

[44] M.-L. Mehta and M. Gaudin, On the density of Eigenvalues of a random matrix, *Nuclear Physics* **18**(Supplement C), 420 - 427 (1960).

[45] Atas, Bogomolny, Giraud, and Roux, Distribution of the Ratio of Consecutive Level Spacings in Random Matrix Ensembles, *Physical Review Letters* **110**(8), 084101 (2013). [1212.5611]

[46] Anderson, Absence of Diffusion in Certain Random Lattices, *Physical Review* **109** 1492-1505 (1958).

[47] F. Evers and A.D. Mirlin, Anderson transitions, *Rev. Mod. Phys.* **80** 1355-1417 (2008).

[48] S.M. Nishigaki, M. Giordano, T.G. Kovacs, and F. Pittler, Critical statistics at the mobility edge of QCD Dirac spectra, *PoS* **LATTICE2013** 018 (2014). [1312.3286]

[49] M. D'Elia and F. Negro, Chiral Properties of Strong Interactions in a Magnetic Background, *Phys. Rev.* **D83** 114028 (2011). [1103.2080]

[50] G.S. Bali, F. Bruckmann, M. Constantinou, M. Costa, G. Endrődi, S.D. Katz, H. Panagopoulos, and A. Schäfer, Magnetic susceptibility of QCD at zero and at finite temperature from the lattice, *Phys. Rev.* **D86** 094512 (2012). [1209.6015]

[51] A. Schäfer, G. Endrődi, and J. Wellnhofer, Center clusters in full QCD at finite temperature and background magnetic field, *Phys. Rev.* **D92**(1), 014509 (2015). [1506.07698]

[52] D. Diakonov and V. Yu. Petrov, A Theory of Light Quarks in the Instanton Vacuum, *Nucl. Phys.* **B272** 457-489 (1986).

[53] R.A. Janik, M.A. Nowak, G. Papp, and I. Zahed, Chiral disorder in QCD, *Phys. Rev. Lett.* **81** 264-267 (1998). [hep-ph/9803289]

[54] J.C. Osborn and J.J.M. Verbaarschot, Thouless energy and correlations of QCD Dirac eigenvalues, *Phys. Rev. Lett.* **81** 268-271 (1998). [hep-ph/9807490]

[55] T.G. Kovacs, F. Pittler, F. Bruckmann, and S. Schierenberg, High temperature quark localization by Polyakov loops, *PoS* **LATTICE2011** 200 (2011). [1112.0119]

[56] T.G. Kovacs and F. Pittler, Poisson statistics in the high temperature QCD Dirac spectrum, *PoS* **LATTICE2011** 213 (2011). [1111.3524]

[57] G. Cossu and S. Hashimoto, Anderson Localization in high temperature QCD: background configuration properties and Dirac eigenmodes, *JHEP* **06** 056 (2016). [1604.00768]

[58] S. Borsanyi, G. Endrodi, Z. Fodor, A. Jakovac, S.D. Katz, S. Krieg, C. Ratti, and K.K. Szabo, The QCD equation of state with dynamical quarks, *JHEP* **11** 077 (2010). [1007.2580]

[59] G. 't Hooft, A Property of Electric and Magnetic Flux in Non-abelian Gauge Theories, *Nucl. Phys.* **B153** 141-160 (1979).

[60] M.H. Al-Hashimi and U. -J. Wiese, Discrete Accidental Symmetry for a Particle in a Constant Magnetic Field on a Torus, *Annals Phys.* **324** 343-360 (2009). [0807.0630]

[61] M. Giordano, S.D. Katz, T.G. Kovacs, and F. Pittler, The chiral transition as an Anderson transition, *PoS* **LATTICE2014** 214 (2014). [1410.8392]

[62] L. Giusti and M. Luscher, Chiral symmetry breaking and the Banks-Casher relation in lattice QCD with Wilson quarks, *JHEP* **03** 013 (2009). [0812.3638]

[63] M. Giordano, T.G. Kovacs, and F. Pittler, An Ising-Anderson model of localisation in high-temperature QCD, *JHEP* **04** 112 (2015). [1502.02532]

[64] J.J.M. Verbaarschot and T. Wettig, Random matrix theory and chiral symmetry in QCD, *Ann. Rev. Nucl. Part. Sci.* **50** 343-410 (2000). [hep-ph/0003017]

[65] K. Fukushima and V. Skokov, Polyakov loop modeling for hot QCD, *Prog. Part. Nucl. Phys.* **96** 154-199 (2017). [1705.00718]

[66] F. Bruckmann, T.G. Kovacs, and S. Schierenberg, Anderson localization through Polyakov loops: lattice evidence and Random matrix model, *Phys. Rev.* **D84** 034505 (2011). [1105.5336]

[67] F. Bruckmann and J. Wellnhofer, Anderson localization in sigma models, In 35th International Symposium on Lattice Field Theory (Lattice 2017) Granada, Spain, June 18-24, 2017 (2017). [1710.05662]

[68] P. Di Vecchia, A. Holtkamp, R. Musto, F. Nicodemi, and R. Pettorino, Lattice CP^{N-1} Models and Their Large N Behavior, *Nucl. Phys.* **B190** 719-733 (1981).

[69] M. Campostrini, P. Rossi, and E. Vicari, Topological susceptibility and string tension in the lattice CP^{N-1} models, *Phys. Rev.* **D46** 4643-4657 (1992). [hep-lat/9207032]

[70] M. Campostrini, P. Rossi, and E. Vicari, Monte Carlo simulation of CP**(N-1) models, *Phys. Rev.* **D46** 2647-2662 (1992).

[71] M. Campostrini and P. Rossi, 1/N expansion of the topological susceptibility in the CP**(N-1) models, *Phys. Lett.* **B272** 305-312 (1991).

[72] Abrahams, Anderson, Licciardello, and Ramakrishnan, Scaling Theory of Localization: Absence of Quantum Diffusion in Two Dimensions, *Physical Review Letters* **42** 673-676 (1979).

[73] F. Bruckmann, G. Endrodi, M. Giordano, S.D. Katz, T.G. Kovacs, F. Pittler, and J. Wellnhofer, Landau levels in QCD, *Phys. Rev.* **D96**(7), 074506 (2017). [1705.10210]

[74] V.M. Kaspi and A.M. Beloborodov, Magnetars, *Annual Review of Astronomy and Astrophysics* **55**(1), 261-301 (2017).

[75] K. Fukushima, Magnetic-field Induced Screening Effect and Collective Excitations, *Phys. Rev.* **D83** 111501 (2011). [1103.4430]

[76] C.N. Leung and S.-Y. Wang, Gauge independence and chiral symmetry breaking in a strong magnetic field, *Annals Phys.* **322** 701-708 (2007). [hep-ph/0503298]

[77] E.J. Ferrer, V. de la Incera, I. Portillo, and M. Quiroz, New look at the QCD ground state in a magnetic field, *Phys. Rev.* **D89**(8), 085034 (2014). [1311.3400]

[78] J.-P. Blaizot, E.S. Fraga, and L.F. Palhares, Effect of quark masses on the QCD pressure in a strong magnetic background, *Phys. Lett.* **B722** 167-171 (2013). [1211.6412]

[79] Sh. Fayazbakhsh and N. Sadooghi, Color neutral 2SC phase of cold and dense quark matter in the presence of constant magnetic fields, *Phys. Rev.* **D82** 045010 (2010). [1005.5022]

[80] E.J. Ferrer, V. de la Incera, and X.J. Wen, Quark Antiscreening at Strong Magnetic Field and Inverse Magnetic Catalysis, *Phys. Rev.* **D91**(5), 054006 (2015). [1407.3503]

[81] Sh. Fayazbakhsh and N. Sadooghi, Phase diagram of hot magnetized two-flavor color superconducting quark matter, *Phys. Rev.* **D83** 025026 (2011). [1009.6125]

[82] K. Fukushima, K. Hattori, H.-U. Yee, and Y. Yin, Heavy Quark Diffusion in Strong Magnetic Fields at Weak Coupling and Implications for Elliptic Flow, *Phys. Rev.* **D93**(7), 074028 (2016). [1512.03689]

[83] K. Fukushima, D.E. Kharzeev, and H.J. Warringa, The Chiral Magnetic Effect, *Phys. Rev.* **D78** 074033 (2008). [0808.3382]

[84] A.V. Sadofyev and Y. Yin, Drag suppression in anomalous chiral media, *Phys. Rev.* **D93**(12), 125026 (2016). [1511.08794]

[85] M. Frasca and M. Ruggieri, Magnetic Susceptibility of the Quark Condensate and Polarization from Chiral Models, *Phys. Rev.* **D83** 094024 (2011). [1103.1194]

[86] J.E. Kiskis, Fermions in a Pseudoparticle Field, *Phys. Rev.* **D15** 2329 (1977).

[87] N.K. Nielsen and B. Schroer, Axial Anomaly and Atiyah-Singer Theorem, *Nucl. Phys.* **B127** 493-508 (1977).

[88] M.M. Ansourian, Index Theory and the Axial Current Anomaly in Two-Dimensions, *Phys. Lett.* **B70** 301-305 (1977).

[89] J.S. Schwinger, On gauge invariance and vacuum polarization, *Phys. Rev.* **82** 664-679 (1951).

[90] M. Lüscher, Properties and uses of the Wilson flow in lattice QCD, *JHEP* **1008** 071 (2010). [1006.4518]

[91] M. Lüscher, Chiral symmetry and the Yang–Mills gradient flow, *JHEP* **1304** 123 (2013). [1302.5246]

[92] S. Durr *et al.*, Ab-Initio Determination of Light Hadron Masses, *Science* **322** 1224-1227 (2008). [0906.3599]

[93] Sz. Borsanyi *et al.*, Ab initio calculation of the neutron-proton mass difference, *Science* **347** 1452-1455 (2015). [1406.4088]

[94] M. Namiki, I. Ohba, K. Okano, M. Rikihisa, and S. Tanaka, Numerical Simulation of Nonlinear σ Model by Means of Stochastic Quantization Method, *Prog. Theor. Phys.* **73** 186 (1985).

[95] K. Okano and L. Schulke, Renormalization and Renormalization Group Behavior of the O(N) Nonlinear σ Model in Stochastic Quantization, *Nucl. Phys.* **B295** 105-122 (1988).

[96] C. Bauer, G.S. Bali, and A. Pineda, Compelling Evidence of Renormalons in QCD from High Order Perturbative Expansions, *Phys. Rev. Lett.* **108** 242002 (2012). [1111.3946]

[97] D.K. Sinclair and J.B. Kogut, Complex Langevin Simulations of QCD at Finite Density – Progress Report, In 35th International Symposium on Lattice Field Theory (Lattice 2017) Granada, Spain, June 18-24, 2017 (2017). [1710.08465]

[98] J. Bloch, J. Glesaaen, J.J.M. Verbaarschot, and S. Zafeiropoulos, Complex Langevin Simulation of a Random Matrix Model at Nonzero Chemical Potential, (2017). [1712.07514]

[99] K. Nagata, J. Nishimura, and S. Shimasaki, Testing the criterion for correct convergence in the complex Langevin method, (2018). [1802.01876]

[100] P. Rossi and U. Wolff, Lattice QCD With Fermions at Strong Coupling: A Dimer System, *Nucl. Phys.* **B248** 105-122 (1984).

[101] F. Karsch and K.H. Mutter, Strong coupling QCD at finite Baryon number density, *Nucl. Phys.* **B313** 541-559 (1989).

[102] M. Fromm, *Lattice QCD at strong coupling*, (Doctoral dissertation). Zurich, ETH (2010).

[103] J. Bloch and F. Bruckmann, Positivity of center subsets for QCD, *Phys. Rev.* **D93**(1), 014508 (2016). ([Addendum: Phys. Rev.D93,no.3,039907(2016)]) [1508.03522]

[104] J. Bloch, F. Bruckmann, and T. Wettig, Subset method for one-dimensional QCD, *JHEP* **10** 140 (2013). [1307.1416]

[105] J. Bloch and F. Bruckmann, Diagrammatics of center subsets for QCD, (to be published).

[106] F. Bruckmann and J. Wellnhofer, Scalar QCD at nonzero density, *PoS* **LATTICE2016** 054 (2016). [1611.05643]

[107] K.E. Eriksson, N. Svartholm, and B.S. Skagerstam, On Invariant Group Integrals in Lattice QCD, *J. Math. Phys.* **22** 2276 (1981).

[108] J. Budczies and M.R. Zirnbauer, Howe duality for an induced model of lattice U(N) Yang-Mills theory, (2003). [math-ph/0305058]

[109] H. Vairinhos and P. de Forcrand, Lattice gauge theory without link variables, *JHEP* **12** 038 (2014). [1409.8442]

[110] B.B. Brandt, R. Lohmayer, and T. Wettig, Induced QCD I: Theory, *JHEP* **11** 087 (2016). [1609.06466]

[111] C. Marchis and C. Gattringer, Dual representation of lattice QCD with worldlines and worldsheets of abelian color fluxes, *Phys. Rev.* **D97**(3), 034508 (2018). [1712.07546]

[112] N. Read and S. Sachdev, Spin-Peierls, valence-bond solid, and Néel ground states of low-dimensional quantum antiferromagnets, *Phys. Rev. B* **42** 4568–4589 (1990).

[113] F. Delfino, A. Pelissetto, and E. Vicari, Three-dimensional antiferromagnetic CP^{N-1} models, *Phys. Rev. E* **91** 052109 (2015). [1502.07599]

Acknowledgements

First and foremost I thank my supervisor Falk Bruckmann for his support and guidance. Next I thank Gergely Endrődi, Matteo Giordano, Sandor Katz, Tamás Kovács, and Ferenc Pittler for many discussions during our colaboration. Furthermore, I thank Jacques Bloch and Christof Gattringer for useful discussions. I also thank Maximilian Emmerich and Jakob Simeth for proof reading the manuscript. This work was supported by the DFG grant BR $2872/7-1$.